

Dissertation
submitted to the
Combined Faculties for the Natural Sciences and for Mathematics
of the Ruperto-Carola University of Heidelberg, Germany
for the degree of
Doctor of Natural Sciences

presented by
Diplom-Physicist Daniel-Rolf Harbeck
born in Hiltrup (now Münster)
Oral examination: May 21st 2003

Chemical Inhomogeneities in the Old Stellar Populations of the Local Group

Referees: **Priv. Doz. Dr. Andreas Burkert**
 Prof. Dr. Immo Appenzeller

Chemische Inhomogenitäten in den alten stellaren Populationen der Lokalen Gruppe

Die alten Sterne der lokalen Gruppe (LG) sind Zeugen der ersten signifikanten Sternentstehungsphasen. Wir untersuchen die Eigenschaften dieser alten Sternpopulationen anhand einiger galaktischer Kugelsternhaufen (KSH) und sphäroidaler Zwerggalaxien (dSphs) der LG. In Kugelsternhaufen finden wir keinen direkten Zusammenhang zwischen dem Problem des zweiten Parameters der Horizontalastmorphologie, interner stellarer Entwicklung, und den chemischen Inhomogenitäten in KSHen feststellen. Vielmehr zeigen wir, daß interne stellare Evolution die chemischen Variationen in KSH nicht alleine erklären kann, sondern daß Szenarien, in denen Akkretion von angereichertem Material oder primordiale Häufigkeitsunterschiede die chemischen Variationen verursachen, wahrscheinlicher sind. Im weiteren benutzen wir Horizontalaststerne (HB-Sterne), um Populationsgradienten in dSph Galaxien zu untersuchen. In vielen Fällen finden eine zentrale Konzentration der roten HB-Sterne im Vergleich zu den blauen HB-Sternen ("interner Zweitparametereffekt"). Wir identifizieren Metallgehaltsunterschiede von Sternen als die dominante Ursache dieser Populationsgradienten, wohingegen ein interner Altersgradient nicht wesentlich zu den unterschiedlichen Horizontalastmorphologien beizutragen scheint. Wir diskutieren die Populationsgradienten in den dSph Galaxien im Kontext möglicher Entstehungsszenarien.

Chemical Inhomogeneities in the Old Stellar Populations of the Local Group

The old stars with ages of order of 10 Gyr in the Local Group (LG) are the legacy of the first epoch of star formation. We investigate the properties of these old stellar populations in several Milky Way Globular Clusters (GCs) and LG dwarf spheroidal (dSph) galaxies. In GCs we study spectroscopically the interplay between internal stellar evolution, the second parameter problem of the horizontal branch (HB) morphology, and star-to-star abundance variations within these clusters. We cannot find evidence for a direct link between chemical inhomogeneities in GCs and the second parameter problem, and internal stellar evolution. Indeed, we demonstrate that internal stellar evolution cannot be the primary driver of the abundance variations in GCs and favor scenarios of accretion of nucleosynthesized material or primordial variations. In the second part we use HB stars to trace population gradients in the LG dSphs photometrically ("internal second parameter effect") and find in many galaxies the red HB stars to be more centrally-concentrated than the blue HB stars. We identify metallicity as the dominant driver of these gradients in dSphs, while age only seems to play a minor role. We discuss the population gradients in dSphs in the context of the formation process of these low-mass galaxies.

Für Leah Elisabeth & Nele Marie

Contents

1	Introduction	1
2	Mixing as a Second Parameter in NGC 7006	3
2.1	Introduction	3
2.1.1	Morphology of the horizontal branch	4
2.1.2	Need for new data	7
2.2	Data and Reduction	8
2.2.1	Spectral Indices	9
2.3	Results	11
2.3.1	An anti-correlation between CN and CH?	15
2.3.2	Radial distribution of CN strengths	16
2.4	Summary	18
3	CN Variations in 47 Tuc	21
3.1	Introduction	21
3.2	Scenarios for Abundance Variations	22
3.3	The Globular Cluster 47 Tuc	24
3.3.1	New information on the main sequence	24
3.4	Data and Reduction	26
3.4.1	Observations	26
3.4.2	Data reduction	28
3.4.3	Membership of program stars	30
3.4.4	A correlation between CN absorption bands	31
3.5	CN variations on the main sequence	32
3.5.1	A Test of the CN Bimodality	32
3.5.2	The CN/CH anti-correlation	35
3.6	Summary and Conclusions	35
3.6.1	External vs. evolutionary scenarios	37
3.6.2	On the origin of the bimodality	38

3.6.3	Where is the polluting gas?	38
3.6.4	Other support for external pollution scenarios	39
3.7	Appendix: Calibration of CN and CH indices in 47 Tuc	44
4	Integrated Spectra of Second Parameter GCs	47
4.1	Introduction	47
4.2	Data and Reduction	50
4.3	Results	51
4.4	Conclusion	54
5	A Wide Field Study of Sextans dSph	57
5.1	Introduction	57
5.2	Observations and Reduction	59
5.2.1	Calibration	61
5.2.2	Reddening	62
5.2.3	Photometric errors and Incompleteness	63
5.3	Color-Magnitude Diagram	64
5.3.1	Distinguishing between foreground dwarfs and red giants	66
5.3.2	Distance modulus	67
5.3.3	Metallicity from the RGB	67
5.3.4	The red bump	69
5.3.5	RR Lyrae stars in Sextans	71
5.4	Radial gradients in post main-sequence populations	72
5.5	Blue stragglers vs. young stars	74
5.6	Discussion	74
6	Population Gradients in LG dSphs	77
6.1	Motivation	77
6.2	The horizontal branch as a tracer of population gradients	78
6.3	Data sample and reduction	79
6.4	Analysis	83
6.4.1	Cumulative radial distribution	83
6.4.2	T_2 statistics of number ratios	83
6.4.3	RGB radial distribution and metallicities	84
6.4.4	The HB morphology index	84
6.5	Radial gradients in the HB morphologies	87
6.5.1	The Milky Way companions	87
6.5.2	The Andromeda companions	89

6.5.3	The lonesome Tucana	89
6.6	Metallicity gradients in dSphs seen in the RGB	89
6.7	The dSphs in the metallicity-HB-index diagram	90
6.7.1	The whole covered field	91
6.7.2	Radial dependence of the HB index and the metallicity	94
6.8	Global Parameters governing HB gradients	96
6.9	Conclusions	98
6.10	Appendix: The transition type galaxy Phoenix	101
6.10.1	Different distributions of subpopulations	101
7	Sextans & Draco dSphs in the SDSS	105
7.1	Introduction	105
7.2	Data, CMD, and star selection	106
7.3	Radial Gradients in the HB morphology	109
7.3.1	Draco	109
7.3.2	Sextans	110
7.4	Conclusions	111
8	Conclusions and future prospects	115
8.1	Is the CN problem in GCs solved?	115
8.2	Do we understand dSphs?	118
8.2.1	How could the population gradients form?	120
8.2.2	The global second parameter effect of LG dSphs	123
8.2.3	Further projects	124
	References	124
	Acknowledgements	133
	Curriculum Vitae	135
	List of Publications	137

Chapter 1

Introduction

The Local Group (LG) of galaxies is the only place in the Universe where we can study the properties and evolution of stellar populations in great detail, since we can resolve them into their constituents, the stars. In contrast, studies of stellar populations of remote galaxies are limited to the investigation of their integrated properties. Only if we understand the nearby resolvable stellar populations of the LG, we can hope to eventually understand unresolved stellar populations at larger distances. The aim of this thesis is to contribute to the understanding of stellar populations in the Local Group, where we concentrate on the *old* stellar populations since these are the legacy of the first epoch star formation episodes. The Globular Clusters (GCs) and the dwarf spheroidal (dSph) galaxies in the LG are of special interest since they provide the best defined populations: GCs consist of single-age, single-metallicity stars; the next level of complexity is reached in the dSphs which have predominantly old stellar populations with a large range in metallicity. While GCs and dSph galaxies appear to be simple systems, they pose a lot of challenges in terms of understanding stellar evolution and galaxy formation.

Although GCs consist of old stars with the same age and same metallicity, the evolution of these most simple stellar populations is still not completely understood. Stars within the same GC and at the same evolutionary state commonly exhibit differences in carbon, nitrogen, and oxygen (CNO) abundances (and in other lighter elements), while showing the same iron abundance. Even the parameters controlling the morphology of the horizontal branches (HBs) in GCs are not completely understood; while metallicity was identified as a major parameter of the HB morphology, other, “second” parameters such as age or stellar rotation, must play an important role. A probable connection between CNO abundance variations — if they trace different internal stellar evolution within a GC — and a “second parameter” of the HB morphology was suggested in the literature. Nevertheless, this hypothesis had not yet been proved or disproved so far. One critical problem is that internal stellar evolution may not be the only source of abundance variations in globular clusters. Intense studies during the last thirty years indicate that internal stellar evolution (i.e., the dredge-up of nucleosynthesised material from the stellar interior to the stellar envelope), external pollution (i.e., the accretion of slow stellar winds from intermediate mass AGB stars), and perhaps primordial variations are all contributing to the the observed intra-cluster abundance variations. It is at least clear that internal stellar evolution cannot be the only important cause of

these variations. For a complete understanding of the GC stellar population, it is important to disentangle the various mechanisms that produce the chemical inhomogeneities. Recent studies, including this thesis work, reveal that external pollution, possibly in binary systems, or by supernova enrichment, seems to be important in GCs.

Once we understand the well-defined stellar populations of GCs we can study the mixed stellar populations of galaxies with more confidence. Dwarf galaxies like the dSphs in the LG may represent the leftover basic building blocks predicted by hierarchical merger scenarios of the origin of massive galaxies. The chemistry of the dwarf galaxies would then define the chemical composition of the ancient populations in these larger galaxies. Although the dSphs are the lowest mass and simplest galaxies known, their stars exhibit a wide spread of abundances, indicating their complex formation histories. Furthermore, each dSph experienced its own unique star formation history, no two dSphs look alike in this respect. In a few dSph galaxies, an internal second parameter effect has been detected: the morphology of the horizontal branch varies from the center to the outer parts in some dSphs. The driver of these population gradients is not well understood as yet.

This thesis is structured as follows: In Chapters 2 and 3 we investigate the problem of chemical inhomogeneities and the second parameter of the HB morphology in MW globular clusters. Despite the fact that stars in globular clusters are believed to be of common origin and they share identical chemical compositions, star-to-star variations in abundances of GC stars are observed. In particular the light CNO elements can show strong differences within a given GC. In chapter 2 we will test and argue against the hypothesis that the scatter in the CNO elements of RGB stars in GCs trace mixing processes in the interior of stars and whether they can be linked to post-RGB stellar evolution. In chapter 3 we will explore the true origin of these abundance variations in GCs. For unevolved stars on the main sequence of the GC 47 Tuc we will demonstrate that processes exterior of these stars, e.g., like primordial abundance variations or self-pollution, must drive the abundance spread rather than internal stellar evolution only. In Chapter 4 we explore the impact of different HB morphologies and CNO abundance variations on the properties of the integrated spectral energy distributions of three GCs.

In the chapters 5, 6, and 7 we investigate the spatial distribution of different stellar populations in LG dSphs as they are traced by HB stars. The detection of significant radial population gradients in the Sextans dSph in Chapter 5 leads us to a comprehensive study of the phenomenon of population gradients in dSphs in Chapter 6. With the observations of the Sextans and Draco dSphs by the Sloan Digital Sky Survey (SDSS) a study of the large scale distribution of stars in these galaxies became possible (Chapter 7).

Finally, we will present our summary and conclusions in Chapter 8. We will also outline future opportunities to extend this research.

Chapter 2

Mixing as a Second Parameter in NGC 7006

Abstract

Rotationally induced mixing with subsequent dredge-up of nucleosynthesized material is discussed as a second parameter of the horizontal branch morphology in globular clusters. CNO abundances have been proposed as tracers of the dredge up of processed material. NGC 7006 is a prominent example of a second parameter GC: Its HB morphology is too red for its metallicity. We present spectroscopic measurements of CN molecular band strengths S(3839) and CH band CH(4300) strengths for 12 giants in NGC 7006 to test rotationally-driven mixing as a second parameter in this cluster. Our observations reveal (i) a scatter in star-to-star CN absorption strengths with the same amplitude as seen in other GCs of the same metallicity, but different HB morphologies; (ii) a possible continuous distribution of CN absorption strength with a preference for CN-enriched stars, and (iii) a possible weak radial gradient in the number ratio of CN-strong and CN-weak stars. We argue against the hypothesis that CN-variations are directly correlated to the second parameter effect of the HB morphology. However, the small sample of stars measured in NGC 7006 prevents us from drawing firm conclusions.

2.1 Introduction

The stellar populations of globular clusters (GCs) consist of single-age and single-metallicity stars of very old age (age ≥ 10 Gyr). At this age, only low-mass ($M \leq 0.9M_{\odot}$) stars are present on the main-sequence, the phase in which they spend most of their lifetime (hydrogen core-burning). Once the hydrogen in their stellar cores is consumed, these stars will enter into the post main-sequence evolutionary phase and will evolve along the red giant branch (hydrogen shell-burning) to the horizontal branch (helium core-burning), and will finally end after the asymptotic giant branch phase (helium shell-burning) on the white dwarf cooling sequence. Since the post main-sequence evolution is very short compared to the lifetime on the main-sequence, the post main-sequence stellar population in an old GC consists of stars of roughly the same initial mass. According to the Vogt-Russell theorem, the initial conditions of a star define its whole subsequent evolution. All stars in a GC post main-

sequence state are assumed to share the same basic initial parameters (age, mass, metallicity). Since in a first approximation all GCs of the Milky Way (MW) have comparable ages, all stars in MW GCs of the same metallicity should evolve in the same way.

Both assumptions (identical evolution of stars within a GC and identical evolution of stars in different GCs of the same metallicity) are falsified by observations: (i) Star-to-star abundance variations in the light elements such as Na, Al, C, N, and O on the RGB of GCs are a hint of additional processes governing the stellar evolution that are not included in the modelling of old stellar populations; the assumption of the same initial conditions on the main-sequence may be invalid (see Chapter 3). (ii) MW GC's of the same metallicity show very different morphologies of the horizontal branch (“second parameter effect”). Additional parameters are required for a description of the post main-sequence stellar evolution. In this chapter, we will investigate stellar rotation as one such second parameter determining the HB morphology.

2.1.1 Morphology of the horizontal branch

The helium-burning sequence of GCs is populated by stars of the same initial mass; typical present-day masses of these stars are $M \sim 0.6 M_{\odot}$. The helium core-burning sequence of GCs is called *the horizontal branch*. The morphology of a GC's HB refers to the distribution of stars along the helium core-burning sequence. This sequence is crossed by the well-defined strip of pulsation instability, in which HB stars will form variable RR Lyrae stars. Since the mass of the helium-burning core of an HB star is almost independent of the initial mass of the star, the *bolometric* luminosity of HB stars is constant, making them useful as standard candles for distance determinations. The HB morphology can be quantified as follows (Lee, Demarque, & Zinn, 1994):

$$HB = \frac{\#B - \#R}{\#B + \#V + \#R}, \quad (2.1)$$

where $\#B$ and $\#R$ are the number of HB stars bluer or redder than the instability strip, respectively; $\#V$ is the number of variable stars in the instability strip. Predominantly due to differential mass-loss in the RGB phase prior to ignition of helium core-burning, an extended region will be populated along the HB with stars of different envelope masses. Among the MW GCs, there is a general dependence of the HB morphology on the clusters' metallicity: On average, metal-poor GCs tend to produce stars with high effective temperatures (blue HB stars), while metal-rich GCs tend to form helium core-burning stars with lower effective temperatures (red HB stars).

It was realized early that other parameters must affect the evolution of stars to the HB (e.g., Sandage & Wildey 1960), since there are GCs that do not strictly obey this metallicity-HB-morphology relation. For example, some GCs show excessively red HB morphologies at a given metallicity (e.g., NGC 7006, Sandage 1967), or excessively blue HB morphologies that do not strictly obey the relation between metallicity and HB-morphology.

In numerous studies, many parameters have been proposed and investigated as “the second parameter”, but the riddle of HB morphologies in globular clusters still lacks a comprehensive solution. For instance, age, helium abundance, CNO abundances, or stellar rotation

and subsequent rotationally induced mixing might affect the HB morphology of a globular cluster (e.g., as systematically investigated by Lee, Demarque, & Zinn 1994). In general, these parameters regulate the evolution of a main-sequence star along the RGB to the HB by changing the mass of the stellar envelope, the mass of the helium burning core, the opacity of the stellar material, or a mixture of these parameters. Following the argumentation of Lee, Demarque, & Zinn (1994), we briefly summarize how different stellar parameters will change the evolution of stars to the horizontal branch. In this chapter we will test if internal abundance spreads in GCs can be linked to the problem of HB morphology. We concentrate on the outer halo cluster NGC 7006 as it shows a prominent second parameter effect: At its given metallicity of $[\text{Fe}/\text{H}] = -1.6$ dex its HB morphology is the reddest among other GCs of similar metallicities, such as M 3, M 13, or M 10 (see Tab. 2.3). Accordingly we will comment how the effects of different parameters on the HB morphology have been explored for this particular globular cluster, NGC 7006.

- **Metallicity:** The main effect of metallicity is a change in the opacity of the stellar material. With increasing metallicity, the opacity rises and will lead to HB stars with lower effective temperatures.
- **Age:** With increasing age on time-scales of several billion years, the mass of a HB star's envelope would decrease, since the total mass of the star at the helium ignition on the RGB is smaller, while the mass of the helium-burning core is unaffected, since the cores of low-mass RGB stars are stabilized by the pressure of a degenerate electron gas. Age is a promising candidate to be *the* second parameter effect: younger GCs would produce redder HBs than older GCs of the same metallicity. For instance, age differences measured with differential age-dating techniques from the main-sequence turn-off (MSTO) might be able to reproduce the differences in the HB morphologies in the pairs NGC 288/NGC 362 at a metallicity of $[\text{Fe}/\text{H}] = -1.2$ dex, where NGC 288 would be 2 ± 1 Gyr older than NGC 362 (Catelan et al., 2001) or for the pair M 3/M 13 at a metallicity of $[\text{Fe}/\text{H}] = -1.6$ dex, where M 13 would be 1.7 ± 0.7 Gyr older (Rey et al., 2001). Buonanno et al. (1991) found a “normal” age for NGC 7006 from the difference in luminosity of the HB and the MSTO. However, no precise relative age-dating is available in the literature.
- **CNO abundance:** CNO abundances affect both the energy production rate on the main-sequence (more CNO in the hydrogen-burning core would allow an increased energy production rate in the CNO cycle) as well as the stellar opacity; as a net-effect, increased CNO abundances would lead to redder horizontal branches. Especially in the case of NGC 7006 the total CNO element abundance was discussed as a promising second parameter: McClure & Hesser (1981) found very strong CH G band absorptions in red giant branch (RGB) stars of this cluster which might reflect a higher total abundance of CNO elements. Nevertheless, Cohen & Frogel (1982) could not confirm an overabundance of CNO elements in NGC 7006. These authors found that the infrared CO molecule absorption strengths of RGB stars are in between those of M 3 and M 13; both GCs have bluer HB morphologies than NGC 7006. Finally, Wachter et al. (1998) found a depletion of carbon in NGC 7006 giants, which is consistent with

the existence of internal C→N processing where nitrogen is nucleosynthesized by the CNO cycle in the stellar interior at the cost of carbon and oxygen. Internal mixing processes could dredge-up this material to the stellar surface. These authors conclude that if the reduced carbon abundance measures the total CNO element abundance, the total amount of CNO is not likely to be responsible for the 2nd parameter effect in NGC 7006. However, deep mixing can significantly deplete the surface carbon abundance of RGB stars. Carbon abundance of stars alone might be an improper proxy for the total CNO abundance of NGC 7006. If CNO enhancement in NGC 7006 would be a second parameter of the HB morphology, increased CN and CH strength compared GCs of bluer HB morphology would be expected, which we do not find in this work.

- Rotational mixing as a second parameter:** Understanding the effect of rotation on stellar evolution is of particular difficulty, since transport of angular momentum in the interior of stars is poorly understood. Rotation can affect the later stellar evolution in several ways: Core rotation would delay the core helium flash, thus leading to higher core masses, resulting in hotter HB stars. Additional mass-loss due to reduced equatorial surface gravity in the later RGB phase would result in lower-mass stellar envelopes, also producing bluer HB stars. Norris (1981) suggested a scenario in which stars with sufficiently high angular momentum would start internal rotationally induced mixing (e.g. the detailed investigation by Sweigart 1997). Such stars with increased internal mixing could dredge-up CNO-cycled, or incompletely CN-cycled or ON-cycled, material. The CNO-cycle at work in the hydrogen-burning shell of RGB stars alters the relative abundances of the CNO elements, increasing N at the cost of C and O. This nucleosynthesized material if transported to the surface would alter the apparent chemical composition of a star's atmosphere. At the same time, the increased angular momentum could lead to increased core masses as well as increased mass-loss during the RGB evolutionary phase thus leading to blue HB stars. Slow rotators on the other hand, would appear CN-poor, would have lower mass loss and would therefore end up as red HB stars. *In this scenario a correlation between CNO surface abundances of RGB stars in a GC and the HB morphology would be expected.* Norris (1981) found a similarity between the bimodal distribution functions of star colors along the HB and the CN absorption strengths of RGB stars, which would be consistent in this picture. The scenario in which the angular momentum distribution of stars in a GC would form a second or third parameter of HB morphology seems very promising. However, recent measurements of rotation speeds of HB stars in the GCs M 13 and M 15 (Behr et al., 2000; Behr, Cohen, & McCarthy, 2000) identified the red HB stars as having higher mean rotational speeds (i.e., as found from the distribution of $v \sin i$) than the blue HB stars. In the rotational mixing scenario the opposite distribution would be expected. These observations could still fit a rotational second parameter scenario if increased mass-loss due to increased rotation speed would also imply increased loss of angular momentum, e.g., in the stellar winds.

In order to trace internal nucleosynthesis of material followed by a dredge-up on the RGB, we are interested in particular in C and N abundances for a large set of RGB stars. These could be obtained by high-resolution spectroscopy, but this approach is time-consuming at

the telescope. It is much more efficient to investigate molecule absorption bands: the CN and CH bands are ideal tools to investigate differences in C and N abundances within a star cluster. As nitrogen is the minor component in GC stellar atmospheres compared to C, an enrichment of N at the cost of C by the CNO-cycle will result in an enhanced CN molecule formation. Stars with increased angular momentum are *hypothesised* to experience rotationally induced mixing and a dredge-up of processed material to the surface, and thus would exhibit increased CN absorption strengths. Slowly rotating stars would retain their normal surface abundances.

To test the hypothesis that CN abundances trace internal mixing processes and are a diagnostic tool to identify rotation as a second parameter in the case of the GC NGC 7006, we aim to compare both the range of CN strengths exhibited by RGB stars, and the relative fraction of CN-rich and CN-poor stars, among a set of GCs with metallicities of $[Fe/H] \sim -1.6$ dex but different HB morphologies. For some GCs of this metallicity, but different HB morphologies, measurements of CN absorption strength are available in the literature. In the scenario of deep mixing one would expect, with metallicity as a fixed parameter, a correlation between the HB morphology of a globular cluster and the star-to-star CN abundance variations within a cluster. Besides the strong “global” second parameter at work in NGC 7006, Buonanno et al. (1991) found evidence for an “internal” second parameter effect in NGC 7006: The morphology of the HB becomes bluer with decreasing radial distance. Unless one accepts an age-spread of order of a few billion years within a globular cluster, such an internal second parameter effect provides evidence of additional *third* parameters other than age. It will be therefore interesting to test if this internal HB gradient is also reflected by a gradient in the CN band strengths.

2.1.2 Need for new data

Although NGC 7006 is an extreme example of the second-parameter effect in GCs, it is poorly studied. Only a few measurements of CN absorption strength are available in the literature. The major difficulty of this object is its large distance (57.4 kpc), and only the tip of the RGB has been explored spectroscopically so far. For example, Kraft et al. (1998) detected from high-resolution spectroscopy of six stars in NGC 7006 with the Keck telescope a Mg-Al anti-correlation which is a strong indication of material nucleosynthesized by hydrogen-shell burning. Due to the large distance of NGC 7006, high-resolution spectroscopy for a large sample of stars is unaffordable for this cluster. A common and well established tool to investigate star-to-star inhomogeneities in the CNO elements are the CN and CH molecule absorption bands. The S(3839) index measures the flux depression in the blue 3883Å CN band compared to a nearby comparison region. CH absorption can be quantified from the 4300Å G-band. The study of these molecular *bands* in contrast to atomic absorption *lines* is possible with intermediate resolution spectra and is therefore more efficient for larger samples of stars. The trade-off of the reduced telescope time requirements is the loss of detailed information on individual elements: The absorption in the CN band depends on the relative abundances of both C and N. Previous studies of NGC 7006 have investigated CN band absorption, but did not publish information about the S(3839) index. This index is

Table 2.1 : L

O

Star-ID	Date	Exposure Time
II-18	19/09/96	3×2700 s
II-46	19/09/96	3×2700 s
V-19	20/09/96	3×2700 s
V-54	20/09/96	1×2700 s
II-103	02/08/97	2×3600 s
II-89	02/08/97	2×3600 s + 1×2700 s
III-1	03/08/97	1×3600 s + 1×1800 s
II-85	03/08/97	2×3600 s + 1×2700 s
II-4	25/08/97	3×3600 s
III-46	25/08/97	2×3600 s + 1×2400 s
III-33	04/07/00	2×3600 s + 2×2700 s
III-40	05/07/00	3×3600 s + 1×2700 s

established as a common tool in CN studies, and in order to provide CN band absorption measurements that can be compared with other GCs of similar metallicities we present here new S(3839) measurements of red giants in NGC 7006.

2.2 Data and Reduction

During several campaigns in the years 1996, 1997, and 2000, spectra of 12 stars among the bright end of the RGB of NGC 7006 were observed with the KAST spectrograph on the Lick 3m Shane telescope by G. H. Smith. The grism No. 1 was used, resulting in a wavelength coverage from 3200 Å to 6500 Å at a dispersion of 2.8 Å/pixel. A Reticon 1200 × 400 CCD with a pixel size of 27 μm and 6 e⁻ readout noise was used as detector. Per observing run typically 20 bias observations and 20 dome flat fields were taken. HeHgCd arc lamp exposures for wavelength calibration and flux standard star observations were obtained. A logbook of the observations is given in Table 2.1; the identification of the observed stars is the same as in Sandage (1967).

The data were reduced separately for each observing campaign using IRAF¹ data reduction routines. The KAST CCD readout system automatically subtracts a bias level from the images estimated from the CCD overscan. We found that the illumination level on the chip affects the estimate for the overscan level (in particular for highly illuminated flat fields). This effect leads to an overestimation of the overscan level in some images. Since the subtracted overscan is stored in the last column of each KAST CCD image, we added back the overscan level. All bias frames were combined and this masterbias was subtracted from all

¹see Acknowledgements

frames. In a subsequent step the flat fields were combined. A polynomial of 25th order in the dispersion direction was used to eliminate both spectral sensitivity and the energy distribution of the quartz lamp from the flat field. The normalized flat field was used to flatten all data.

The long exposure spectra of NGC 7006 are affected by cosmic ray hits. We found that the best way to remove them was to use the `lacos_spec` task (van Dokkum, 2001). Most of the stars were observed several times, and we coadded the available CCD frames to a final deep, almost cosmic-ray-free image. The spectra were extracted with the `specred` package in IRAF. From the typically five flux standards stars observed per campaign the spectral sensitivity function was determined and used to flux-calibrate the stellar spectra. Note that the spectra are only calibrated with respect to relative spectral sensitivity, but not in absolute sensitivity.

For each spectrum we measured the centers of the Ca II H+K lines with the `rvidlines` task in the `rv` package under IRAF to determine the radial velocities of the stars. Since we want to measure spectral indices in the rest frame wavelength, we corrected the spectra for the measured Doppler shift. The final extracted spectra of all stars are plotted in Fig. 2.1.

Additionally we measured relative radial velocities via cross-correlation relative to the star II-4 using the `fxcor` task in the IRAF `rv` package. We found a nearly Gaussian distribution of relative velocities with a dispersion of ~ 50 km/s, but with one significant outlier: The star III-1 was found to have a relative radial velocity of +245 km/s compared to II-4. We conclude that all stars in our sample but III-1 are members of NGC 7006. The spectrum of III-1 is peculiar and dominated by prominent molecular bands (see Fig. 2.2). According to its features (strong C₂ and CH absorption bands and strong Mgb lines) we identify this star as a foreground dwarf carbon star. We will comment on this class of stars in Chapter 8.

2.2.1 Spectral Indices

From the spectral energy distribution we measured the strength of the absorption by the CN molecule at the 3883 Å band. The CH absorption strength was measured from the 4300 Å G-band. The spectral indices S(3839) and CH(4300) are established tools to quantify the absorption strengths in these molecular bands, as they measure the flux depression in the molecular bands relative to a nearby continuum. The indices are defined according to Norris et al. (1981), but we modified the definition of the CH index continuum passband to avoid strong sodium sky emission lines. The CN index definition remains unchanged, allowing a direct comparison to results of other studies:

$$S(3839) = -2.5 \log \left(\frac{\sum_{3846}^{3883} F_{\lambda}}{\sum_{3883}^{3916} F_{\lambda}} \right) \quad (2.2)$$

$$CH(4300) = -2.5 \log \left(\frac{\sum_{4280}^{4320} F_{\lambda}}{\sum_{4250}^{4280} F_{\lambda} + \sum_{4320}^{4340} F_{\lambda}} \right) \quad (2.3)$$

Larger index values correspond to increased molecular band absorption. An additional spectral index S(4241) to measure CN absorption in the molecular band at 4215 Å is not

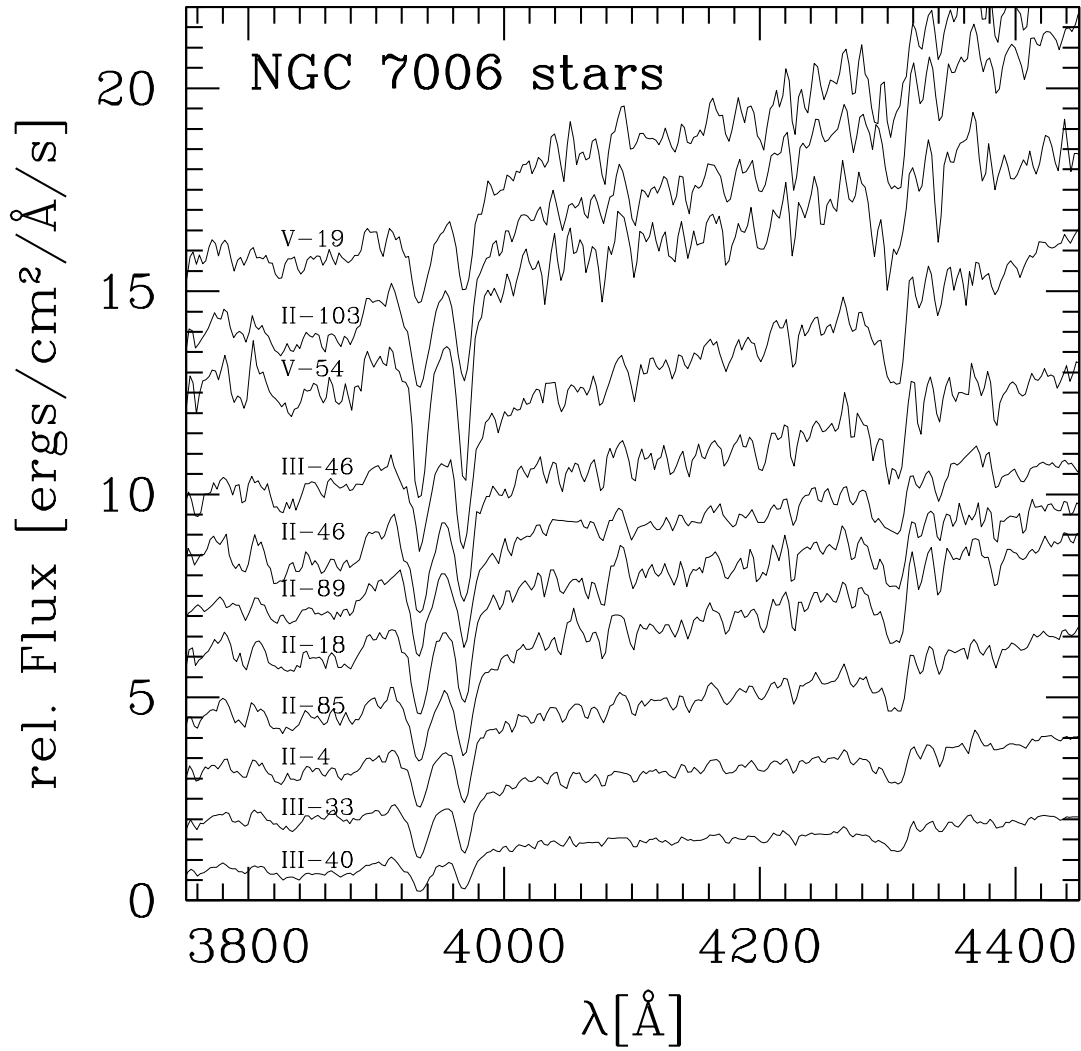


Figure 2.1 : Spectra of all stars in our sample; the peculiar star III-1 is excluded. The spectra are shifted to avoid overlap.

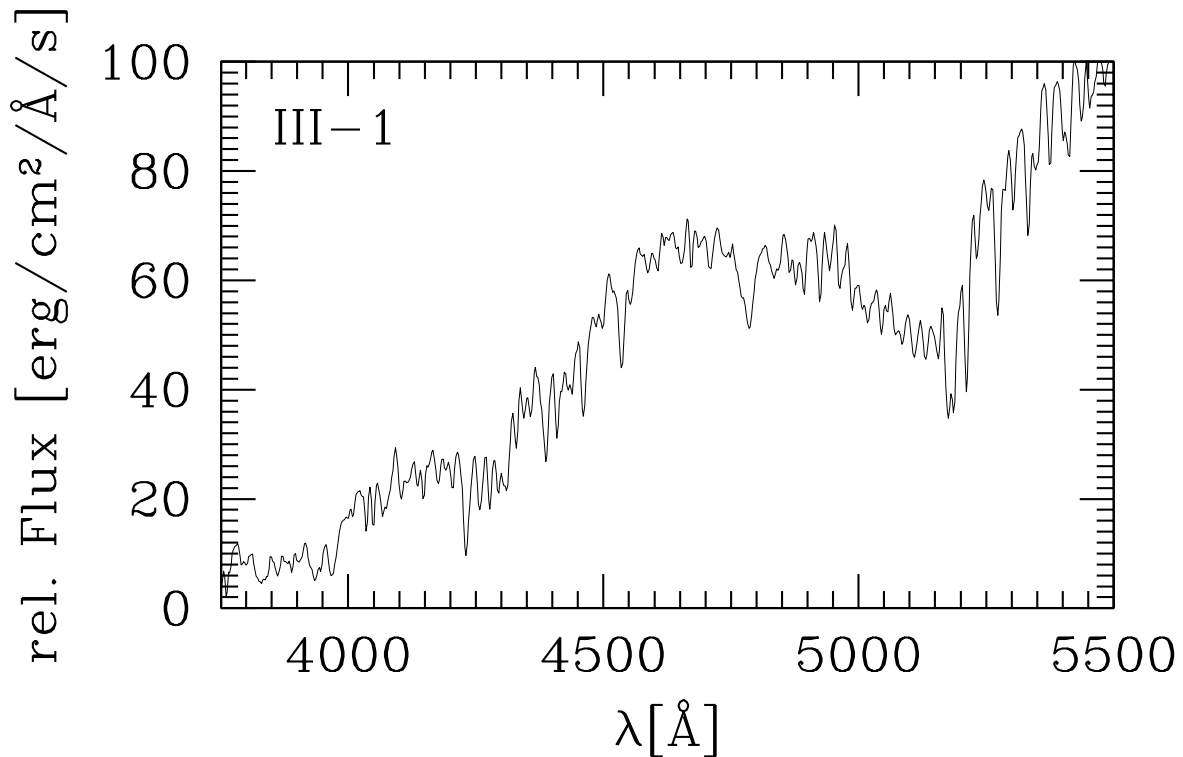


Figure 2.2 : *Spectrum of the peculiar star III-1. Note the strong absorption bands due to CH and C₂.*

considered here, since the absorption in this molecular band is very low for metal-poor stars. Most of the stars were observed several times. For two representative stars we tested if the individual measurement of the S(3839) index would reproduce the measurement on the combined spectrum. The typical scatter in S(3839) among the short exposures is of order $\sigma_{S(3839)} = \pm 0.03$ dex. To account for different exposure times of the stars, we determine the uncertainty of the CN and CH indices based on the Poisson noise of the number counts within the index passbands. The measured indices as well as photometry from Sandage (1967) are listed in Table 2.2.

2.3 Results

The formation of CN and CH molecules is affected by temperature as well as by gravity effects. Since our sample spans only a small range in color (temperature) and luminosity, this dependence of the molecule formation cannot easily be determined. We compare the NGC 7006 S(3839) strengths to those of the well studied GCs M 3 and M 10, which have the same metallicity as NGC 7006. Smith (2002b) homogenized CN S(3839) measurements of stars in M 3 from numerous sources in the literature. For M 10, we use the measurements of Smith & Fullbright (1997). One result of the Smith (2002b) study is a good description of the dependence of the CN absorption strength on the luminosity/temperature for stars on the upper RGB. A prominent feature is the decrease of CN absorption strengths for stars

Table 2.2 : P

Star-ID	V	(B-V)	S(3839)	CH(4300)
II-103	16.23	1.41	0.302 ± 0.06	1.367 ± 0.03
II-18	16.32	1.33	0.149 ± 0.07	1.338 ± 0.04
II-4	16.62	1.21	0.139 ± 0.07	1.404 ± 0.04
II-46	16.38	1.38	0.239 ± 0.07	1.374 ± 0.04
II-85	16.60	1.20	0.115 ± 0.07	1.410 ± 0.04
II-89	16.53	1.21	0.243 ± 0.07	1.324 ± 0.04
III-1	16.44	1.37	-0.017 ± 0.07	1.428 ± 0.04
III-33	16.77	1.10	-0.038 ± 0.07	1.341 ± 0.05
III-40	16.96	1.12	0.208 ± 0.09	1.404 ± 0.06
III-46	16.78	1.24	0.042 ± 0.06	1.409 ± 0.04
V-19	15.50	1.72	0.120 ± 0.07	1.367 ± 0.04
V-54	15.85	1.35	0.066 ± 0.05	1.289 ± 0.03

brighter than $M_V \leq -1.8$ mag. In Fig. 2.3 we compare our measurements of the 3883 Å CN band for NGC 7006 (filled circles) with the literature data for M 3 (tripods) and M 10 (open squares). The temperature effect on the CN formation efficiency is clearly visible in the M 3 sample; with increasing luminosity (=decreasing surface temperature) the formation of CN becomes more efficient. At the turnover at $M_V = -1.8$ mag the CN formation is reduced for increasing luminosities as described by Smith (2002b). We observed only the brightest stars in NGC 7006, in particular all stars are at the luminosity of or brighter than the CN-turnover luminosity. Two bright (and red) stars in our sample were identified as variable stars; at their location in the color-magnitude diagram the risk of AGB star contamination is very high, and for a comparison between M 3, M 10, and NGC 7006 we favour concentrating on the stars at the turn-over region.

Range of CN absorption strengths

The range of CN absorption strengths at a given magnitude in NGC 7006 (see Fig. 2.3) is comparable, within the errorbars, to the range covered by the globular clusters M 3 and M 10 . Both comparison clusters have metallicities comparable to NGC 7006 (see Tab.2.3), but bluer HB morphologies (HB-values of 0.08 and 0.98, respectively). There is no clear indication in NGC 7006 of a bimodal distribution of CN absorption strengths as is observed in M 3, M 10, or in other globular clusters. A continuous distribution of S(3839) absorption strengths is suggested for NGC 7006, although the small size of our measurements prohibits a unique determination of the NGC 7006 CN distribution function.

In the scenario of rotation as the second parameter we would expect stars in GCs with blue HB morphologies to have on average higher angular momentum than stars in GCs with red HB morphologies. We consequently expect that stars in NGC 7006 should be slower

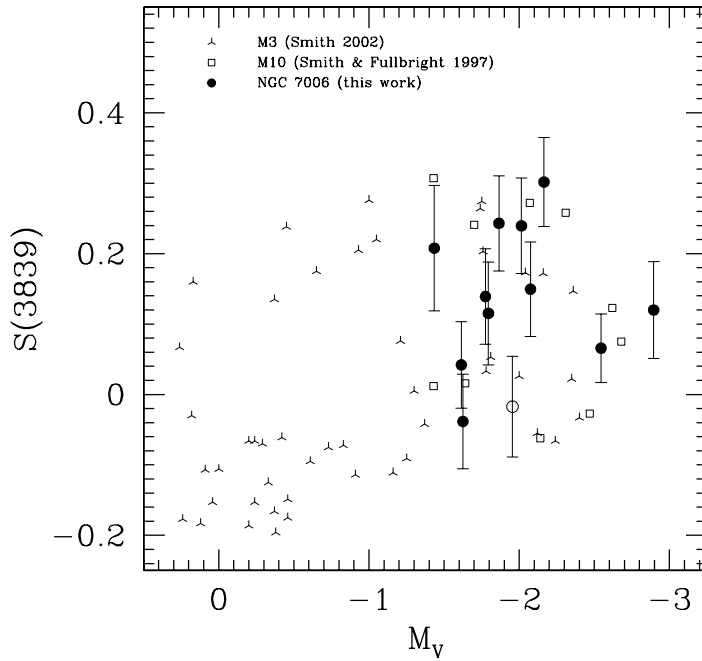


Figure 2.3 : Comparison of $S(3839)$ absorption strength in NGC 7006 (filled circles), M3 (stars) and M10 (open boxes). In the magnitude range covered by our observations the scatter in the NGC 7006 CN absorption strength compares well to those in M3 and M10. There is no clear bimodal signature as is visible in M3. The foreground dC star III-1 is plotted with an open circle.

rotators than stars in M3 or M10. Under this assumption, stars in NGC 7006 would experience less rotationally induced mixing, and less nucleosynthesized material should become dredged-up to the stellar envelope. If rotation were primarily responsible for determining both HB morphology and CN inhomogeneities a smaller range in CN absorption strength and/or a preference for stars with low CN abundances would be expected in NGC 7006. Our observation of a range of $S(3839)$ absorption strengths in NGC 7006 that is comparable to those seen in GCs with bluer HB morphology contradicts — within the limitations of the small sample — the predictions of this scenario.

Ratio of CN-strong/CN-weak stars

We could not identify a correlation between the range of CN absorption strengths in NGC 7006, M3, and M10 and the HB morphology. In a second attempt we investigate the ratio by number $r = \frac{\#CN\text{-strong}}{\#CN\text{-weak}}$ of CN-strong to CN-weak stars in GCs with metallicities comparable to NGC 7006: In the scenario of rotationally induced mixing the distribution of CN absorption strengths should prefer CN-poor stars in GCs with low mean stellar angular momentum (and relatively red HB morphologies), while CN-strong stars should be preferred in GCs with high mean stellar angular momentum (and bluer HB morphologies).

For GCs with bimodal distributions of CN absorption strengths a clear classification into CN-strong and CN-weak stars is possible. We collect the fraction r for GCs with metallicities comparable to NGC 7006 where data are available from the literature in Table 2.3. The metallicities and HB morphologies are taken from Harris (1996). In NGC 7006 the classification of CN absorption strengths of stars is ambiguous: if we consider all NGC 7006 stars with magnitudes $M_V \geq -2.4$ and $S(3839) \geq 0.1$ as CN-strong (see Fig.2.3), we obtain a number ratio of $r = \frac{7}{2} = 3.5$. Ignoring stars with intermediate $S(3839)$ absorption strengths

Table 2.3 : CN

Cluster	[Fe/H]	HB	r	Sources
M 10	-1.52	0.98	0.71	1,2
M 13	-1.54	0.97	3.2	3
M 3	-1.57	0.08	0.42	4
NGC 3201	-1.58	0.08	1.00	5
NGC 1904	-1.57	0.89	2.60	6
M 22	-1.64	0.91	0.42	7
NGC 6752	-1.56	1.00	0.95	8
NGC 6934	-1.54	0.25	0.58	9
M 2	-1.62	0.96	3.5	10
NGC 7006	-1.63	-0.28	(2-3.5)	this work

[Fe/H] and HB morphologies from Harris (1996); r is the number ratio $r = \frac{\#CN-strong}{\#CN-weak}$;

References: 1 – Briley & Smith (1993); 2 – Smith & Fullbright (1997), 3 – Norris (1987), 4 – Smith (2002b), 5 – Smith & Norris (1982); 6 – Langer, Suntzeff, & Kraft (1992), 7 – Norris & Freeman (1983), 8 – Norris et al. (1981); 9 – Smith & Bell (1986), 10 – Smith & Mateo (1990)

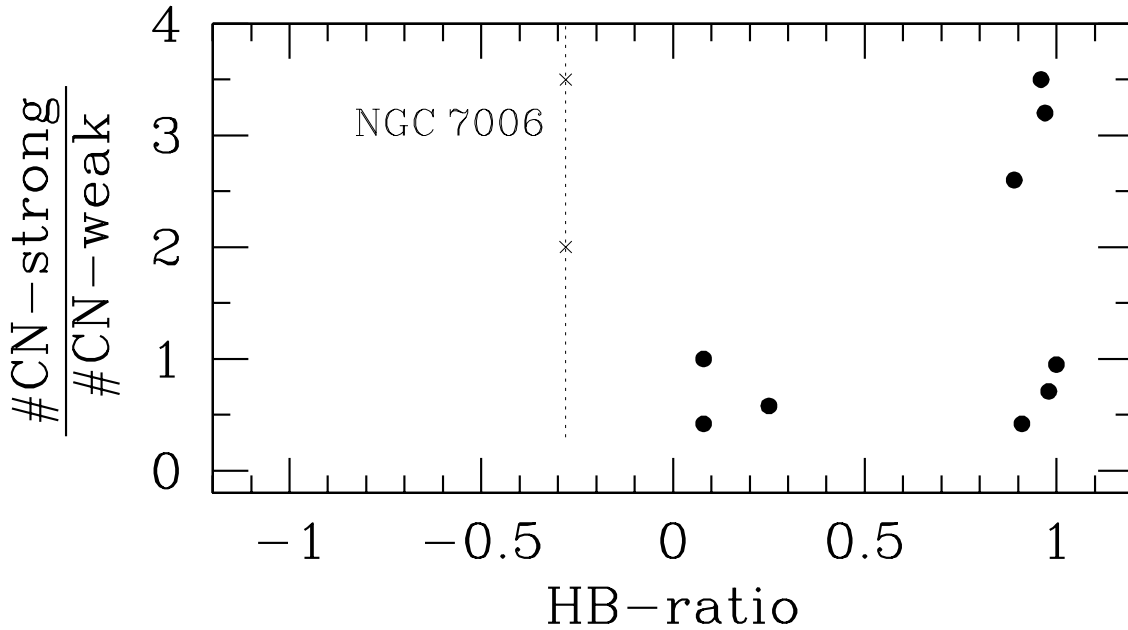


Figure 2.4 : Comparison of the HB morphology and the content of CN-enhanced stars in GCs. We plot the HB morphology index $= \frac{\#B-\#R}{\#B+\#V+\#R}$ vs. the number ratio r between CN-enhanced and CN-weak stars. The crosses represent two different estimates of r in NGC 7006 (see text). The dotted line indicates the range r in NGC 7006 consistent with the uncertainties of the number counts.

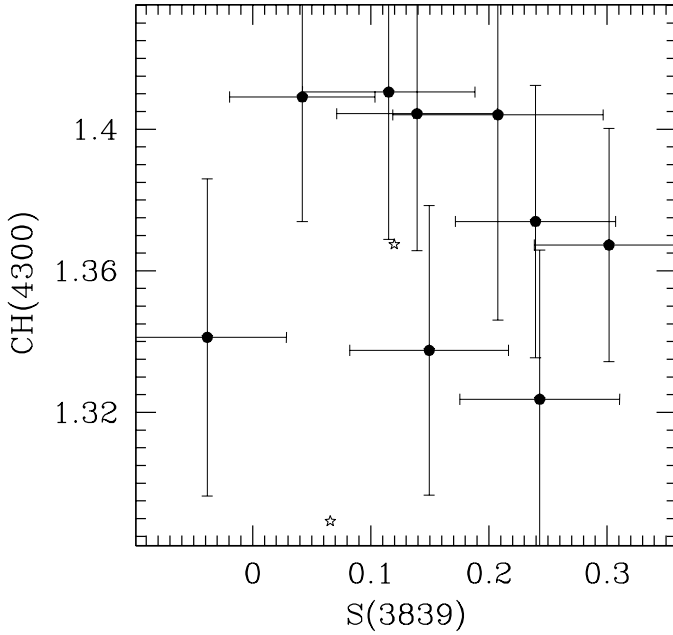


Figure 2.5 : Comparison of the CN and CH absorption strengths in NGC 7006. Stars with $M_V \geq -2.2$ mag are plotted with filled circles. The two brightest giants in the sample are plotted with open stars.

($0.1 \leq S(3839) \leq 0.18$), results in $r = \frac{4}{2} = 2$.

Fig. 2.4 shows the HB index vs. the CN-ratio r for the sample of GCs with metallicities comparable to NGC 7006. Due to the ambiguity of r in NGC 7006 we refrain from boldly plotting it in this diagram. In this sample, no clear correlation between the HB morphology and the ratio of CN-strong to CN-weak stars is apparent, as also found in a similar study by Smith (2002a). M 2 and NGC 1904 fulfill the expectation of the rotation plus mixing scenario that GCs with extremely blue HB morphology should have more CN-strong stars than GCs with a redder HB morphology. But at the same time there are GCs with very blue HB morphologies and low number ratios r comparable to GCs with normal HB morphologies. NGC 7006 seems to have a too large ratio r to support the scenario of an r -HB-type correlation. If the distribution of angular momentum among stars in a GC is correlated with the fraction of CN-enhanced stars, stellar rotation cannot be identified as a second parameter of the HB morphology, at least for our sample of GCs with metallicities of $[\text{Fe}/\text{H}] \sim -1.6$. We would like to point out that a correlation between the distribution of CN absorption strengths and stellar rotation in GCs still has to be proven. Since the initial distribution of angular momentum can only be measured on the main-sequence of GCs with high-resolution spectroscopy, limitations in telescope size and instrumentation have not permitted such studies so far. While main-sequence stars in GCs such as M 3 and M 13 are now in reach of large telescopes, the distant cluster NGC 7006 is still too far away for efficient studies of such stars.

2.3.1 An anti-correlation between CN and CH?

For a variety of GCs with CN abundance variations an anti-correlation between the CN band and CH G-band absorption strengths has been detected, e.g., in M 2, M 3, M 10, M 13, and NGC 6752. Such a CN-CH anti-correlation is expected if CN variations are produced by

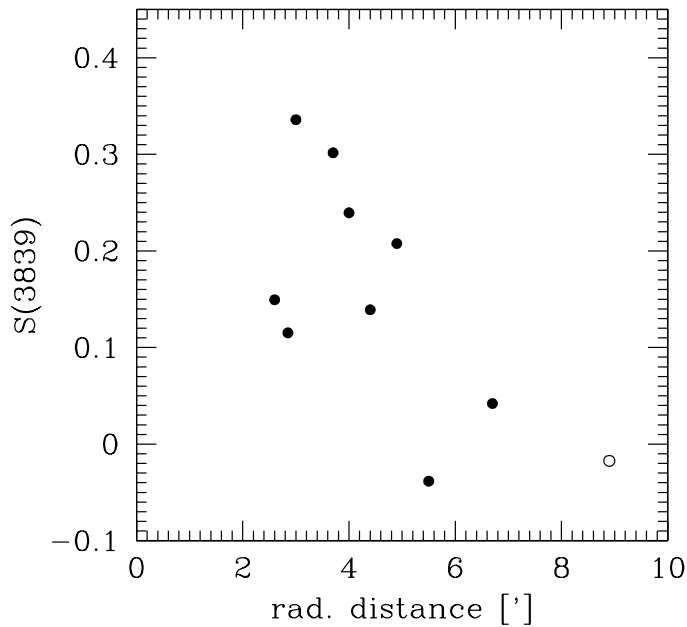


Figure 2.6 : A plot of the CN absorption strength of NGC 7006 giants vs. projected distance to the cluster center. Stars with strong CN bands are found at small radial distances, while the two CN-weak stars have large radial distances. Note that there are no CN-weak stars with a radial distance $\leq 5'$. Only stars with $M_V \geq -2.3$ are plotted with filled circles. The open circle indicates the location of the field star III-1.

nucleosynthesis of material in the CNO cycle. Nitrogen would be enriched at the cost of carbon and oxygen. The N-enhancement will lead to CN-strong stars, while the reduced carbon content in such stars would suppress CH molecule formation. In Fig. 2.5 we plot the S(3839) vs. CH(4300) spectral index for stars in the narrow luminosity range from $M_V = -2$ mag to -1.5 mag. The impact of temperature effects on the molecule formation is therefore expected to be negligible. The uncertainties in the CH indices, coupled with an apparently small range in CH(4300) values among our NGC 7006 giants, do not allow quantification of the true scatter in CH absorption strength. We conclude that there is no evidence of a CN-CH anti-correlation from Fig. 2.5, although it might be hidden in the observational uncertainties.

2.3.2 Radial distribution of CN strengths

NGC 7006 has been reported to show — besides its global second parameter effect — an internal “second” parameter effect. The morphology of the HB changes with the radial distance to the cluster’s center (Buonanno et al., 1991): The HB morphology appears bluer in the central parts than in the outskirts. It appears therefore interesting to address the question if a similar trend can be found for the distribution of CN absorption strength. Our sample of eleven NGC 7006 stars lacks the statistical significance of a large survey. Nevertheless, we investigate the radial distribution of CN-weak and CN-strong stars in our sample. In Fig. 2.6 we plot the CN absorption S(3839) vs. the projected radial distance on the sky. Surprisingly, all CN-enhanced stars have distances smaller than $4.5'$, while the two CN-weakest stars have larger distances. A radial distance of $4.5'$ corresponds to approximately 0.7 tidal radii ($r_t = 6.34'$; Harris 1996). The lack of CN-strong stars at large radial distances is an uncertain result due to the small number of observed stars; the absence of CN-poor stars in the cluster’s

inner part is worth noting. We test the significance of the radial gradient in the distribution of CN-strong ($S(3839) \geq 0.1$) and CN-weak ($S(3839) \leq 0.1$) stars with a Kolmogorov-Smirnov test. This test results in a 0.6% probability that CN-strong and CN-weak stars follow the same radial distribution.

A radial gradient in the distribution of CN strengths has been found in the globular cluster 47 Tuc (Norris & Freeman, 1979). In this cluster, CN-strong stars are more centrally concentrated than CN-weak stars. Briley (1997) pointed out that there are no CN-weak stars in the very center of 47 Tuc. The same situation might be seen in NGC 7006. Although the gradient in NGC 7006 has to be proven by a larger sample, the existence of such a gradient is not unrealistic as it is not without precedent.

If this gradient in CN absorption strength is indeed real, its implication is not unique. In the scenario of rotationally induced mixing this gradient would reflect a gradient in the angular momentum distribution of the stars, where stars in the inner part of NGC 7006 would have higher angular momentum. Accordingly, the central stars would experience enhanced internal mixing (\rightarrow enhanced CN) and enhanced mass loss (\rightarrow evolving to the blue HB). It is not clear if the distribution of angular momentum dates to the star formation epoch of NGC 7006, or if close stellar encounters with transfer of angular momentum lead to a spin-up of those stars orbiting preferentially within the inner parts of the GC.

In other scenarios, such as accretion of CNO processed stellar winds (see Chapter 3), the gradient in CN strengths would reflect different efficiencies of the accretion process. Thus, one would expect stellar winds to settle at the center of a GC; stars with orbits restricted to the GC central regions would accrete more material than stars on more extended orbits. Thus, the central concentration of CN-enriched stars could be consistent with the accretion scenario. A more detailed investigation of the suggested gradient in CN absorption strengths in NGC 7006 appears desirable.

Sodium, Oxygen, and CN among NGC 7006 giants

In GCs with CN abundance variations, a positive correlation between the sodium abundance and CN is often found. At the same time, CN and the oxygen abundance tend to be anti-correlated (e.g., the review by Kraft 1994). An oxygen-CN anti-correlation is a natural consequence of CNO-processing. The situation is less clear in the case of the sodium-CN correlation: initial interpretation of this correlation was that material in CN-strong GC red giants had been nucleosynthesized by neutron-addition reactions in more massive AGB stars, whose stellar ejecta were accreted by those stars seen at the present time. However, a neon \rightarrow sodium proton capture chain was identified as a possible mechanism to allow internal sodium enhancement even in low-mass stars (Denisenkov & Denisenkova, 1990; Langer, Hoffman, & Sneden, 1993; Cavallo, Sweigart, & Bell, 1996, 1998). If this process is indeed present in RGB stars, the internal mixing scenario would still be consistent with a sodium-CN correlation as has been argued by a number of authors (e.g., Weiss, Denisenkov, & Charbonnel 2000).

Does NGC 7006 obey the general correlations between CN, sodium, and oxygen observed in other GCs? In Fig. 2.7 we compare the CN absorption strengths measured in this study

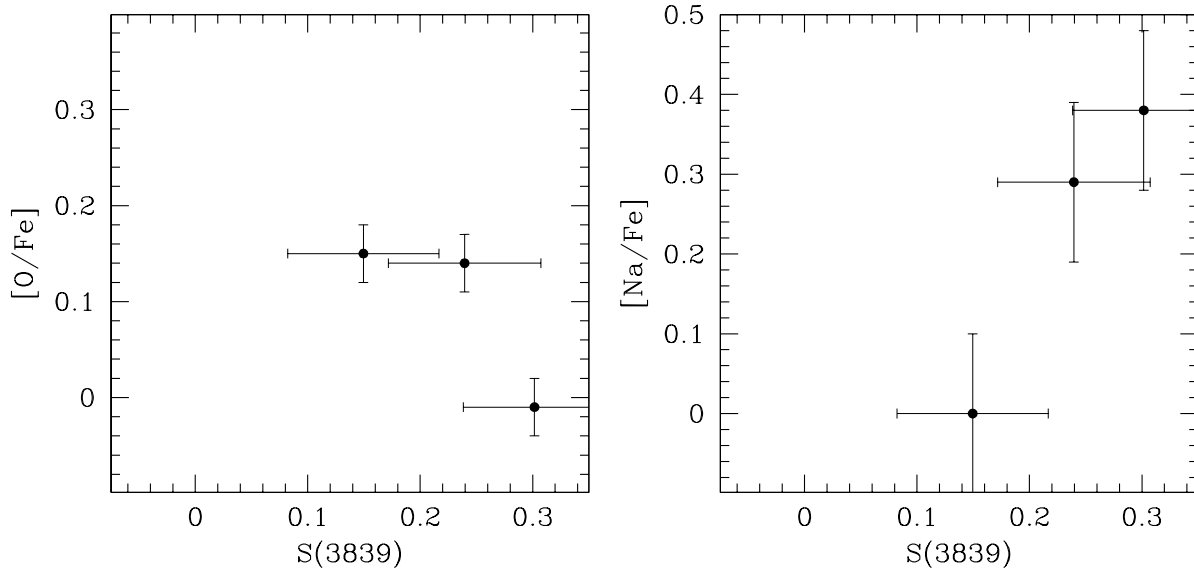


Figure 2.7 : Comparison of CN $S(3839)$ band strength with oxygen (left) and sodium (right) abundance measurements for stars in common with Kraft et al. (1998). Within the strong limitation of the dataset, an oxygen-CN anti-correlation and a positive sodium-CN correlation is consistent with the observations.

to the sodium and oxygen abundances measured by Kraft et al. (1998) from high-resolution spectroscopy obtained at the Keck telescope. There are five stars in common with this study, including the two peculiar variable stars which are excluded from this comparison. The three stars with measured oxygen and sodium abundances are III-33, III-48, and III-46. All stars are intermediate or strong in CN; no CN-poor stars are included in this common sample. Although lacking strong significance, a CN-oxygen anti-correlation as well as a CN-sodium positive correlation is suggested.

2.4 Summary

Based on single-slit spectroscopy at the 3m Shane telescope requiring seven nights of observing time we have presented CN and CH molecule absorption strengths for twelve stars in NGC 7006. We discussed the variations in CN and CH in the context of the second parameter effect of horizontal branches in GCs. Within the limitations of this modest set of CN observations in NGC 7006 obtained so far, we found indications of (i) a continuous distribution of CN $S(3839)$ band strength, (ii) a range in CN absorption strength among RGB stars comparable to the CN spread present in the GCs M 3 and M 10, and (iii) more RGB stars seem to be CN-enriched in NGC 7006 than in the two comparison clusters. A radial gradient in the CN enrichment of stars in NGC 7006 is suggested.

For GCs of a metallicity of $[Fe/H] \sim -1.6$ dex, we found that the range of CN strengths within a GC is not different in GCs of different HB morphologies, as it would be expected in a scenario of internal nucleosynthesis and subsequent dredge-up of material due to rotationally induced mixing. Thus, stellar rotation could not be clearly identified as a second parameter

of horizontal branch morphology. However, the small sample of stars observed in NGC 7006 do not allow us to finally disprove this scenario.

If the distribution of angular momentum is a second parameter, it might not necessarily be traced in a sufficient way by CN variations on the RGB, since an abundance spread due to internal stellar evolution could be hidden by stronger, primordial CN variations. It is therefore mandatory to investigate the true origin of CN variations in GCs. We will come to this point later in Chapter 3.

A direct measurement of the angular momentum distribution (i.e., the distribution of $v \sin i$) in GCs at the main-sequence turn-off (MSTO) is the more appropriate method to investigate the effect of rotation on stellar evolution². In particular, a measurement of the angular momentum distribution would allow a quantitative approach to the connection between rotation and HB morphology and would not suffer from the model uncertainties of the qualitative approach of CN abundances and internal mixing as proxies for rotation. Fiber-fed spectrographs at large telescopes (i.e., FLAMES at the VLT which became available for observations in 2003) will allow measurement of rotation speeds of the faint MS stars in nearby GCs. Moreover, sensitive tracers of internal mixing such as the $^{12}\text{C}/^{13}\text{C}$ isotope ratio will allow detailed studies of internal mixing processes along the RGB in the future.

²As bright RGB stars have very extended stellar envelopes, conservation of angular momentum requires extremely low rotation speeds of these stars; the broadening of absorption lines in stellar spectra can not be used to determine $v \sin i$.

Chapter 3

Cyanogen abundance variations on the Main Sequence of 47 Tuc

Abstract

We report on a deep spectroscopic survey for star-to-star CN variations along the main sequence (MS) of the globular cluster 47 Tuc with ESO's VLT. We find a significant bimodal distribution in the S(3839) index for main-sequence stars in the mass range of ~ 0.85 to $0.65 M_{\odot}$, or from the main-sequence turn-off down to ~ 2.5 mag below the main sequence turn-off. An anti-correlation of CN and CH is evident on the MS. The result is discussed in the context of the ability of faint MS stars to alter their surface composition through internal evolutionary effects. We argue against internal stellar evolution as the only origin for the abundance spread in 47 Tuc; an external origin such as pollution seems to be more likely.

3.1 Introduction

Globular clusters (GCs) are well suited to the study of ancient star formation and the evolution of low-mass stars. In standard formation scenarios all stars of a GC formed at the same time from a single gas cloud; as a consequence all stars within a cluster should have the same age and the same initial chemical composition. Indeed, within many globular clusters the star-to-star iron abundance spread is smaller than typical (spectroscopic or photometric) measurement errors (e.g., as reviewed by Suntzeff 1993a, or in recent work by Gratton et al. 2001). Nevertheless, detailed studies have revealed that there are significant star-to-star abundance variations of certain light elements including sodium, aluminium, carbon, nitrogen, and oxygen in globular clusters (e.g., the review by Kraft 1994). One of the first discoveries of chemical inhomogeneities in GCs was made by Osborn (1971), who found two red giant stars in M10 and M5 to have enhanced CN molecular absorption strengths compared to other stars in these clusters.

The first detailed studies of the abundance spread phenomenon concentrated on the brightest stars at the tip of the red giant branch (RGB); increasing telescope size and improved instruments have allowed investigation of the chemical compositions of stars along the RGB

down to the subgiant branch (SGB) (e.g., Bell et al. 1983; Bell et al. 1984; Hesser et al. 1984; Smith et al. 1989; Suntzeff & Smith 1991; Briley et al. 1992; Cohen, Briley, & Stetson 2002). Even the main sequence turn-off (MSTO) region of a few nearby GCs has been reached (Hesser, 1978; Briley et al., 1991, 1994; Suntzeff & Smith, 1991; Cannon et al., 1998; Cohen, 1999a,b; Briley & Cohen, 2001; Gratton et al., 2001). The main result of all these efforts in the last thirty years is the discovery of abundance variations in some GCs along the whole stellar evolutionary sequence from the RGB to the SGB and even to below the MSTO. Some of the better studied examples of globular clusters with abundance variations are 47 Tuc, M13, and M3.

The ultimate tool for studying the chemical compositions of GC stars is high-resolution spectroscopy of element absorption lines. Unfortunately, for stars near the MSTO of globular clusters this approach requires extremely long exposure times even with the present day 10-meter-class telescopes. However, the study of absorption bands produced by molecules can serve as a useful tool to investigate abundance variations even with moderate resolution spectra. For example, the broad CN and CH absorption features at 3883 Å and 4300 Å respectively are measurable for faint stars at the limits of large telescopes by either medium-resolution spectroscopy or narrow-band photometry.

To investigate the origin of abundance inhomogeneities in globular clusters, we have performed the deepest survey to date of CN band absorption in main sequence stars of the globular cluster 47 Tuc. In this chapter we report on our observations with the Very Large Telescope (VLT), which has resulted in the detection of significant star-to-star differences in the CN abundance 2.5 mag below the MSTO (i.e. $V=21.5$ mag) of 47 Tuc. In Sections 3.2 & 3.3 we briefly review current scenarios that could explain abundance spreads in GCs and describe earlier work on 47 Tuc. Sections 3.4 & 3.5 describe our observations and the data analysis. Our conclusions are presented in Section 3.6.

3.2 Scenarios for Abundance Inhomogeneities in Globular Clusters

Although the problem of abundance inhomogeneities, especially in the CN molecule, within globular clusters was recognized over thirty years ago, their origin is still unresolved. Over these thirty years three scenarios have received considerable discussion in the literature: (i) abundance changes produced internally by the evolution of GC stars, (ii) GC self-pollution, and (iii) primordial inhomogeneities or cluster self-enrichment. An excellent review of these scenarios can be found in Cannon et al. (1998), whose arguments we summarize here.

Stellar Evolution

If all stars in a globular cluster started with the same initial chemical composition, the surface abundances of many of them evidently have since changed by varying amounts during their subsequent evolution. In the stellar evolution scenario CNO-cycle processed material from the interior of hydrogen-burning stars is dredged up (e.g. by rotational mixing) to the

stellar surface. The efficiency of this dredge up is reflected by changes in the surface chemical composition. This scenario can explain why chemical inhomogeneities are generally found in the CNO elements, but not in the iron-peak elements. Although according to conventional stellar evolution models the dredge up of processed material happens only on the RGB, CN variations are evident along the RGB, SGB, and at the MSTO of a number of globular clusters such as 47 Tuc, M71, and M5, e.g., Hesser (1978); Hesser & Bell (1980); Cannon et al. (1998); Cohen (1999a); Cohen, Briley, & Stetson (2002). As such, it is not currently possible to account for the luminosity behaviour of CN variations in GCs by a stellar evolution scenario. In many clusters the CN band strengths at a given stellar luminosity show a bimodal distribution (see e.g., Norris 1987; Smith 1987); the reason why stellar evolution would routinely produce a bimodality rather than a more uniform distribution is not yet understood.

Self Pollution

Asymptotic giant branch (AGB) stars with masses of $\sim 5 M_{\odot}$ eject stellar winds that contain considerable CNO processed material (e.g., Ventura, D'Antona, Mazzitelli, & Gratton (2001)). Other types of stars such as planetary nebulae progenitors or novae could also eject CNO-enriched material. These stellar winds may be accreted by other stars, including the present day MSTO, SGB, and RGB stars. Stars that accreted such material would show different surface compositions than stars that accreted no material. If only the stellar surfaces were polluted, deep convective mixing during the evolution along the RGB should dilute the chemical inhomogeneities. This effect is not seen at least in the case of the nitrogen abundance, although the [C/Fe] abundance is found to decrease with luminosity on the RGB in some clusters such as M92 and M13 (Carbon et al., 1982; Suntzeff, 1981). Also, a bimodal abundance distribution might not be expected from such a phenomenon, but rather a range in the surface contamination.

Primordial variations

The assumption that all stars in a globular cluster had the same chemical composition from the very beginning may not necessarily be true. For instance, two molecular clouds of different chemical composition could have merged and formed a globular cluster. If the gas was not mixed, stars would reflect the chemical composition of one or the other cloud. Here, a bimodal distribution could be explained. An imperfect merging of the gas clouds would lead to a range of abundances. Also, the first supernovae during the star forming epoch of a GC may have polluted the parent molecular cloud. Stars that formed after these events would be enriched in a variety of elements. These two primordial scenarios may explain abundance variations in the CNO elements, but they lack an easy explanation of the chemical homogeneity of the iron-peak elements. In a third “primordial” scenario two globular clusters experienced a collision and merged after they had completed their star formation. The result would be a bimodal abundance distribution, but again the homogeneity of the iron-peak and other heavy elements is a problem.

3.3 The Globular Cluster 47 Tuc

The globular cluster 47 Tuc is a very attractive object for a detailed chemical investigation. It has a distance of only 4.5 kpc and it is after ω Cen the second-brightest cluster ($M_V = -9.4$ mag) in the Milky Way. Due to a tidal radius of 47.25' it is quite an extended object on the sky. The intermediate metallicity of the cluster RGB stars ($[Fe/H] = -0.7$ dex) makes the formation of CN molecules in their atmospheres more efficient than in metal-poorer GC giants. Not surprisingly, a number of studies of CN abundance variations in 47 Tuc have been carried out. In one of the earliest studies McClure & Osborn (1974) found star-to-star differences in the DDO C(41-42) CN index. The distribution of CN band absorption strengths at a given point on the RGB was shown to have a bimodal signature by Norris & Freeman (1979), with there being indications of an anticorrelation between CN and CH band strengths (Norris, Freeman, & Da Costa, 1984). The main results from studies in the last 30 years show CN variations along the RGB of 47 Tuc down to the MSTO. In the latest large photometric narrowband filter survey of 47 Tuc, Briley (1997) verified the existence of a bimodal distribution of CN band strengths, with a radial gradient in the relative fraction of stars with strong and weak CN bands; in the inner part of the cluster there is a higher fraction of stars with strong CN absorption than in the outer parts. The existence of this gradient had been first noted by Norris & Freeman (1979), and further documented by Paltoglou (1990). References to additional studies can be found in Briley (1997).

The deepest CN survey done in 47 Tuc so far (and in GCs in general) extends to one magnitude below the MSTO (Cannon et al., 1998). These authors pursued deep spectroscopic work at the limits of a 4m-class telescope. They showed that the bimodal distribution of CN band strengths still exists on the upper main sequence. With the recent availability of 8 to 10-meter-class telescopes and with the capability of multi-object spectroscopy, large samples of stars on the fainter main sequence now become accessible for chemical abundance studies. The investigation of chemical inhomogeneities on the fainter main sequence can contribute new evidence for or against the various scenarios described above.

3.3.1 New information on the main sequence

In the evolutionary scenario of GC abundance variations all stars in a cluster started with the same initial chemical composition; internal evolutionary effects like deep mixing changed the star's surface composition at a later date. To change the surface element abundances, two mechanisms are required: (i) a nuclear process must change the abundance of a certain element (in the case of the CNO process the ratio of the elements C, N, and O would be altered), and (ii) some interior mass transport mechanism(s) must dredge up the processed material to the stellar envelope. In this study we concentrate on abundance variations in the C and N elements since they can easily be detected spectroscopically by variations in the CN bands.

In the low-mass stars on the main sequence of globular clusters the pp-chain is the dominant process to produce nuclear energy in the stellar core. In addition the CNO process is contributing to the total energy output. Although the CNO cycle is a catalytic process, it

can alter the abundance ratios of the elements involved due to the different time-scales of the various reactions in this cycle. Especially the nitrogen content increases at the cost of carbon and oxygen; the sum of C+N+O remains constant. The efficiency of the CNO process depends strongly on the temperature; therefore this cycle is the dominant nuclear process in young massive main sequence stars, but its contribution to the energy output is marginal for stars of a solar mass and below. According to stellar models globular cluster stars at the upper main sequence with masses of $\sim 0.8 M_{\odot}$ should not support deep mixing processes (the convective envelope being relatively shallow at least in terms of the contained mass) so that the stellar evolution scenario seems to fail to account for observed CN variations at the MSTO. Additionally, mixing processes would add fresh fuel to the hydrogen burning cores of the MS stars that would affect the lifetime of their core-burning phase. As pointed out in, e.g., Cannon et al. (1998), no such effect can be seen in 47 Tuc. Nevertheless, the understanding of deep mixing or other material transportation processes is still incomplete and other mechanisms like diffusion should still be taken into account.

Turn-off stars in 47 Tuc have masses of $0.85 M_{\odot}$ (see Fig 3.1). Cannon et al. (1998) showed that stars at the turn-off and below down to a magnitude of $V = 18.6$ mag or a mass of $\sim 0.75 M_{\odot}$ exhibit CN abundance differences. In our study, we have measured stars with magnitudes down to $V = 20$, or 2.5 mag below the MSTO, which have masses around $0.65 M_{\odot}$ (Fig. 3.1). The (model-dependent) core temperature of these stars is $\log(T_c) \sim 7.10$ at the MSTO and $\log(T_c) \sim 7.01$ for the fainter stars. These stellar parameters were taken from isochrones for a metallicity of $Z = 0.004$ and an age of 14 Gyr (Girardi et al., 2000). Due to the strong dependence of the CNO cycle energy production rate ϵ_{CNO} on the temperature ($\epsilon_{CNO} \propto T^{17}$), the contribution of the CNO cycle relative to the energy production by the pp-chain ($\epsilon_{pp} \propto T^6$) will be reduced by a factor of approximately ten in the fainter stars. This estimate is based on the decreased core temperature only and does not account for a decreasing core density. Therefore the CNO cycle efficiency in stars 2.5 mag below the MSTO is suppressed by *at least* this factor of ten. If hydrogen-burning products could be dredged up to the surface, the amount of CNO processed material that could lead to CN variations would also be reduced by a factor of at least ten for the fainter stars.

This simple calculation can be summarized in the following statement: along the main sequence the production rate of N due to the CNO cycle becomes completely suppressed for the lower mass stars with masses of $\sim 0.65 M_{\odot}$. If there is still some scatter in the CN content between faint stars along the MS, internal stellar evolution cannot explain this scatter because there is no internal CNO-process working to change the ratio of the CNO elements, and external processes (outside a given star) must have played an important role. If the abundance spread disappears among the fainter stars, this would be clear evidence for internal mixing processes as the origin of the CN abundance riddle. Measurements of the CN content of faint main sequence stars can therefore distinguish between the internal evolutionary scenario of CN variations and external scenarios. However, CN measurements alone cannot distinguish between different external scenarios. The main sequence study of Cannon et al. (1998) extends to a mass of $\sim 0.75 M_{\odot}$. At this mass, the CNO process efficiency is reduced by only a factor of ~ 3 . Surveying CN bands at even lower masses can greatly strengthen the constraints placed on the stellar evolution scenario by way of the above CNO-cycle efficiency argument.

3.4 Data and Reduction

3.4.1 Observations

Target selection from WFI imaging

Candidate stars in 47 Tuc for spectroscopy with the VLT of the European Southern Observatory (ESO) at Cerro Paranal, Chile, were chosen from CCD images of the cluster. In September 2000 we observed 47 Tuc with the MPG/ESO 2.2-m telescope at La Silla, Chile, using the Wide Field Imager (WFI) (Baade et al., 1998) with Johnson B and V filters. The exposure times were 3×300 s in each filter. Conditions were non-photometric with a seeing of $1.5''$. The WFI offers a field of view (FoV) of 34 arcmin^2 and consists of a mosaic of eight 4096×2048 CCDs. The WFI was centered on the globular cluster. The radius of the FoV is $\sim 0.8^\circ$, which is approximately half the tidal radius of 47 Tuc. The basic processing of the raw CCD frames was done using the tasks `esowfi` and `mscred` in IRAF. To facilitate proper sky subtraction and to reduce the incidence of blended images we decided to only select stars in the outer, less-crowded regions of 47 Tuc for the follow-up spectroscopy. We therefore concentrated on chip #1 of the CCD mosaic (at the north-east corner of the FoV) to define the sample of spectroscopy candidates. With chip #1 we sample a radial coverage from $8'$ to $25'$, or 0.3 to 0.5 tidal radii. For the selected chip we performed PSF photometry using the DAOPHOT (Stetson, 1992) implementation in IRAF. Since the observations were obtained under non-photometric conditions and no local standard stars are available in the area covered by chip #1, we matched the observed MS and the SGB to fiducial lines published by Hesser et al. (1987). The calibrated photometry was dereddened assuming $E(B - V) = 0.04$ (Harris, 1996). The resulting, dereddened color-magnitude diagram is shown in Fig. 3.1.

Spectroscopy with the VLT/FORS2/MXU

The goal of our spectroscopic observations was to measure the strengths of the 3883 \AA and 4215 \AA CN absorption bands. We used the Focal Reducer and Low Dispersion Spectrograph 2 (FORS2) at the ESO VLT. FORS2 is equipped with a mask exchange unit (MXU) which allows multi-slit spectroscopy with freely defined metal slit masks and a FoV of $6.8 \times 6.8 \text{ arcmin}^2$. We defined three slit masks with the FORS instrument mask simulator (FIMS) software package provided by ESO. The positions of the program stars were determined on CCD images that were obtained at the FORS/MXU. The exposure time for the preimages was 45 seconds with a V filter. The slit width on the masks was fixed to $1''$ and the slit length was chosen to be at least $8''$ to allow for local sky subtraction. Typically 35 slits were fitted onto one mask. In some cases two stars could be observed with one slit. We selected the grating B600 with a dispersion of 50 \AA mm^{-1} or $1.2 \text{ \AA pixel}^{-1}$. In combination with the $1''$ slit width this results in a nominal spectral resolution of 815, or a line width of $\leq 5 \text{ \AA}$. The actual spectral coverage depends on the location of a star on the mask, but we took care to cover at least the range 3800 \AA to 5500 \AA . All program stars are listed in Table 1. The observations were carried out in service mode between 2001 July 18 and 2001 July 26. Each mask configuration was observed four times with exposure durations of

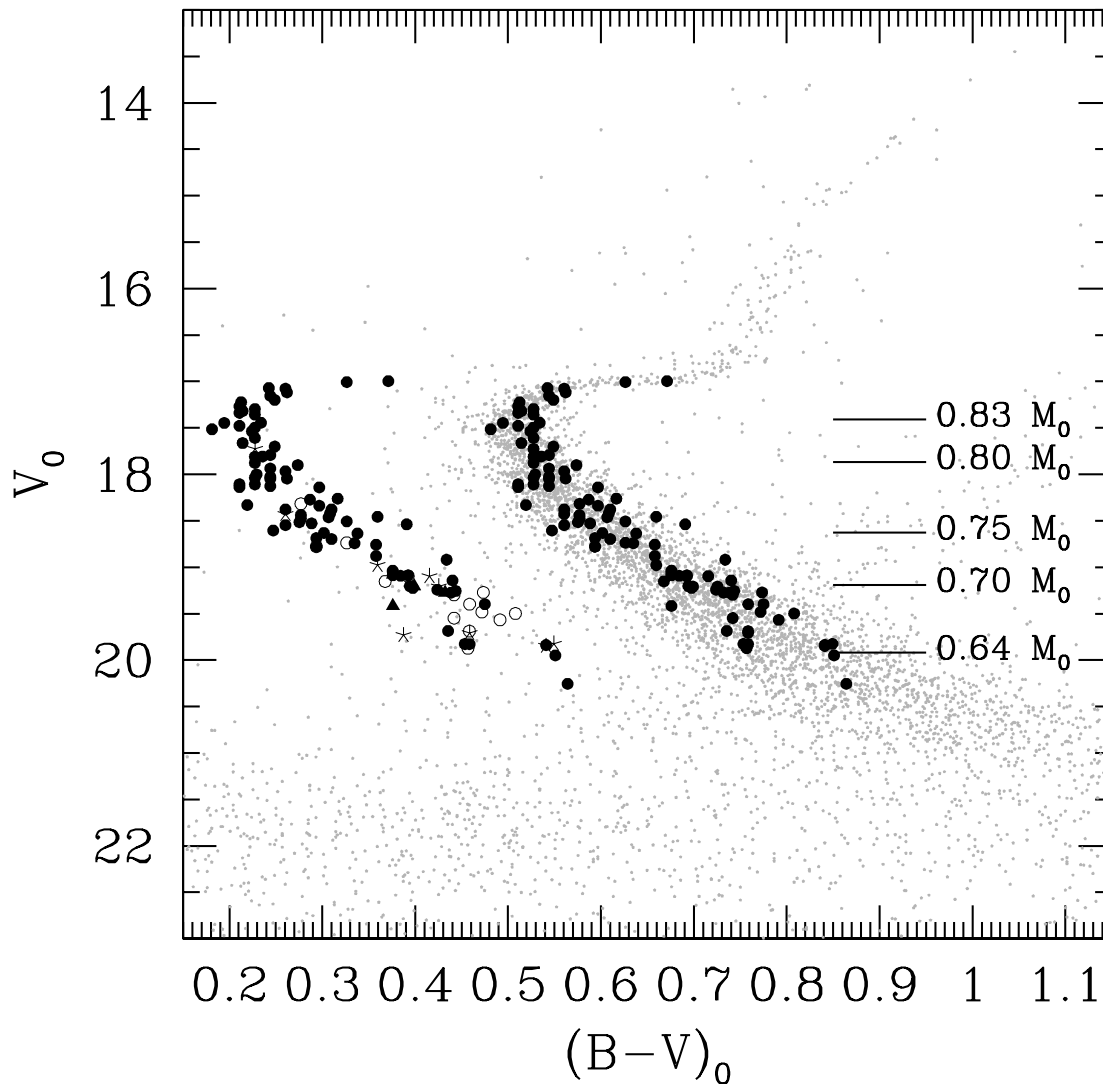


Figure 3.1 : Color magnitude diagram of 47 Tuc based on WFI observations. All program stars are plotted on the main sequence with filled dots. Based on isochrones for $Z = 0.004$ and an age of 14 Gyr (Girardi et al., 2000) we show the stellar masses at various points along the main sequence. For better visibility, all program stars are plotted again with an offset of 0.3 mag in $(B-V)$. Stars with clean CN measurements are plotted with filled circles (quality="0"), while ambiguous measurements (quality="1") are indicated by open circles. Four cluster non-members, that are possibly SMC giants, are marked with triangles. Program stars with unreliable spectroscopy are marked by asterisks (quality="2").

2925 s each, leading to a total exposure time of 3.25 hours per mask. The seeing conditions were almost always better than 1'' according to our specification for the service observations. Additionally, bias, flat field, and wavelength calibration observations were obtained.

3.4.2 Data reduction

All data were reduced using the `ccdred` and `specred` packages under IRAF. First all frames were overscan and bias corrected. The flat fields for each night and mask were stacked. Since each slit mask was observed four times and the alignment of the frames was excellent, we coadded the four frames for a given slit mask with cosmic ray rejection enabled. The resulting frames were almost free of cosmic rays. For further analysis we extracted the area around each slit and treated the resulting spectra as single-slit observations. The wavelength-calibration images and flat fields were treated in the same manner. We fitted a tenth-order polynomial to the flat field images to correct for the continuum. The (separated) object spectra and arc images were flat-field calibrated with these continuum-corrected flat fields. The `doslit` task was used to wavelength calibrate, sky-subtract, and extract the stellar spectra. The wavelength solution from the HgCd arcs was fitted by a fourth-order spline. The typical rms of the wavelength calibration is on the order of 0.2Å, which is expected at the given spectral resolution.

Spectral indices

We measure the strength of the CN absorption bands at 3883 Å and 4215 Å using spectral indices $S(3839)$ and $S(4142)$ similar to those of Norris & Freeman (1979); Norris et al. (1981). These indices basically quantify the CN content of the atmospheres of red giant stars. Unfortunately, the main sequence stars we are considering here have strong hydrogen lines in the region of the $S(3839)$ spectral index. We therefore modify this index according to Cohen (1999a) to exclude these hydrogen lines. Additionally we quantify the CH molecular absorption at 4300 Å using a $CH(4300)$ index defined according to Cohen (1999a,b). As a check we additionally extract an HK index that measures the absorption strength of the Ca H+K lines. The index definitions are:

$$S(3839) = -2.5 \log \frac{F_{3861-3884}}{F_{3894-3910}} \quad (3.1)$$

$$S(4142) = -2.5 \log \frac{F_{4120-4216}}{0.4 F_{4055-4080} + 0.6 F_{4240-4280}} \quad (3.2)$$

$$CH(4300) = -2.5 \log \frac{F_{4285-4315}}{0.5 F_{4240-4280} + 0.5 F_{4390-4460}} \quad (3.3)$$

$$HK = -2.5 \log \frac{F_{3910-4020}}{F_{4020-4130}} \quad (3.4)$$

where $F_{3861-3884}$, for example, is the summed spectral flux (in our case ADU counts) from 3861Å to 3884Å. Each index quantifies the absorption strength of a molecular band or atomic

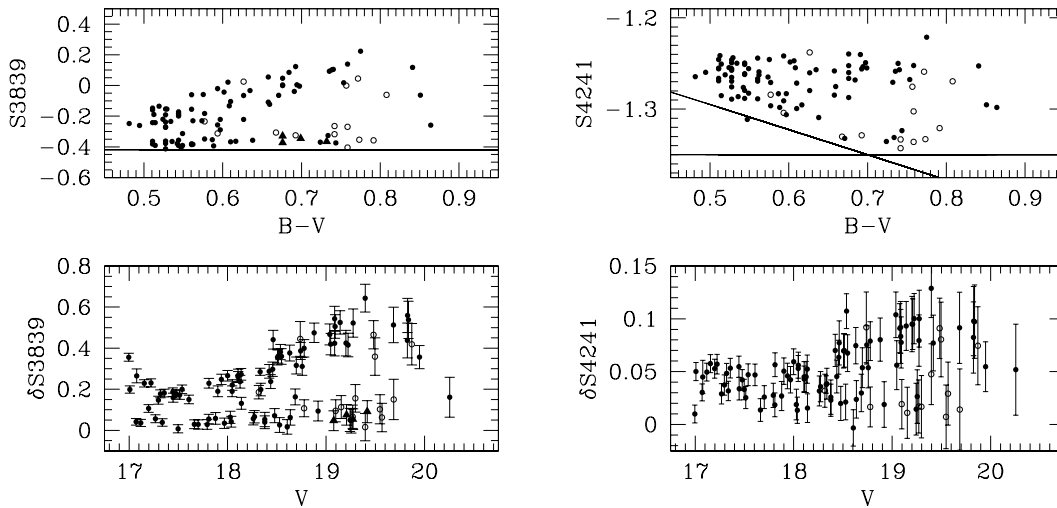


Figure 3.2 : *Left: The CN index $S(3839)$ plotted against the $B-V$ color of 47 Tuc main sequence stars (upper panel). We correct for a zeropoint such that CN-weak stars have a corrected index $\delta S(3839) = 0$. This corrected CN index is plotted in the lower panel versus the stellar V magnitude. Note the significant scatter in the $\delta S(3839)$ index even for the faintest stars. For stars fainter than $V = 17.5$ mag the separation between CN-strong and CN-weak stars is more than 0.2 in $S(3839)$ and increases with increasing magnitude. The distribution of CN-poor and CN-enhanced stars does not seem to be random but is bimodal. Symbols are the same as in Fig. 3.1. Right: Same as at the left side, but for the weaker CN band index $S(4142)$. Since a baseline to the $S(4142)$ index exhibits a stronger dependency on the temperature we correct with a linear fit (the pair of solid lines). Note the increased bimodality for the fainter stars.*

lines relative to a nearby pseudo-continuum. For stronger band absorption the index values increase.

The derived indices $S(3839)$ and $S(4142)$ are plotted versus the $(B - V)$ color of each star in the upper panels of Fig. 3.2 and Fig. 3.2. The formation efficiency of the CN molecule depends on the temperature, and therefore the indices can have a dependence on the color of the stars. For $S(3839)$ the effect here is negligible. To correct for this effect in the $S(4142)$ index, we assume a combination of two straight lines (see Fig. 3.2) as a lower envelope and subtract this fit from the data. A constant value (see Fig. 3.2) is subtracted from $S(3839)$ such that the corrected values approximately equal zero for the CN-poor stars. The corrected CN indices will be referred to as $\delta S(3839)$ and $\delta S(4142)$; they are plotted versus the stellar V magnitudes in the lower panels of Fig. 3.2 and Fig. 3.2. The derived index values can be found in Table 3.1. The plotted error bars are calculated assuming Poisson statistics in the flux summations.

To verify the reliability of the $S(3839)$ index we visually classified the CN absorption strength for all stars into five classes. We found an excellent correlation between the $S(3839)$ index value and our visual classification. We have assigned a "quality" flag to the data for each star. Stars for which spectra show clean CN absorption bands with few noise imperfections and for which a reasonably confident CN classifications was felt to be obtainable

have been assigned a data flag of “0”. In some cases, however, we could not judge a unique CN classification by eye, especially for a few faint stars near to the center of 47 Tuc. Such instances tend to occur when spectra have a low S/N or do not show consistent trends in the three main absorption features at 3860 Å, 3875 Å, or 3889 Å of the blue CN band. These stars may be blended with others (as suspected by their proximity to the cluster center) and are flagged with a “1” in Table 3.1. Nevertheless, the stars in this quality class generally follow a relation between the visual classification and the measured S(3839) absorption strength. For a few stars the data reduction produced poor S/N spectra. This may probably be due to a misalignment of the slits. These stars are flagged by a “2” in Table 3.1 as poor quality spectra. In Figs. 3.2 and 3.2 stars for which the spectrum obtained is assigned to quality class “1” are plotted with open circles. Stars that did not permit visual classifications are not plotted.

3.4.3 Membership of program stars

Field star contamination

We estimate the expected number of galactic foreground stars in our 47 Tuc field. According to Ratnatunga & Bahcall (1985) the expected contamination by the Milky Way is ~ 3.5 field main sequence stars per arcmin² in a 2 mag interval from $V = 18$ to $V = 20$ and a 0.5 mag interval in $(B - V)$ centered on the main sequence fiducial. We selected our spectroscopy candidate stars from a 0.05 mag wide region in $(B - V)$ about the 47 Tuc main sequence over a luminosity range from $V \sim 17.5$ mag to ~ 20 mag. We used only a small fraction of the FoV of FORS for candidate star selection due to our constraints on the wavelength coverage. Per mask configuration an effective FoV is $\sim 6' \times 2' = 12$ arcmin². The expected number of field stars in the field of view of our three slit masks is therefore $\frac{3.5 \text{ stars/arcmin}^2}{2 \text{ mag} \cdot 0.5 \text{ mag}} \cdot 2.5 \text{ mag} \cdot 0.05 \text{ mag} \cdot 3 \text{ masks} \cdot 12 \text{ arcmin}^2 \sim 16$ stars. The number of stars observed in the FoV of three slitmasks and the selected part of the 47 Tuc main sequence is ~ 2500 . In our sample of 115 spectroscopic survey stars we therefore expect a total number of $\frac{115}{2500} \cdot 16 \sim 1$ field star. We conclude that the contamination by galactic field stars that cannot be identified by their radial velocity has a negligible effect on our results and does not account for the CN bimodality seen within our sample of stars.

Contamination by the SMC

In the color magnitude diagram of 47 Tuc (Fig. 3.1) the RGB of the Small Magellanic Cloud (SMC) crosses the main sequence of 47 Tuc at a magnitude of $V \sim 20$ mag. The SMC has a radial velocity of $+163 \text{ km s}^{-1}$, while the radial velocity of 47 Tuc is -18 km s^{-1} . We determined the radial velocities (RVs) of the observed stars by measurement of the center of the calcium H+K lines as well as the H δ absorption line. The typical rms of the RV measurement for a single star is of order 30 km s^{-1} to 40 km s^{-1} . For the well-sampled spectra we expect an accuracy of $\sim \frac{c}{850} \times \frac{1}{10} = 35 \text{ km s}^{-1}$, which is in good agreement with the actual measured scatter. The `rvidlines` task in the `rv` package in IRAF was used to

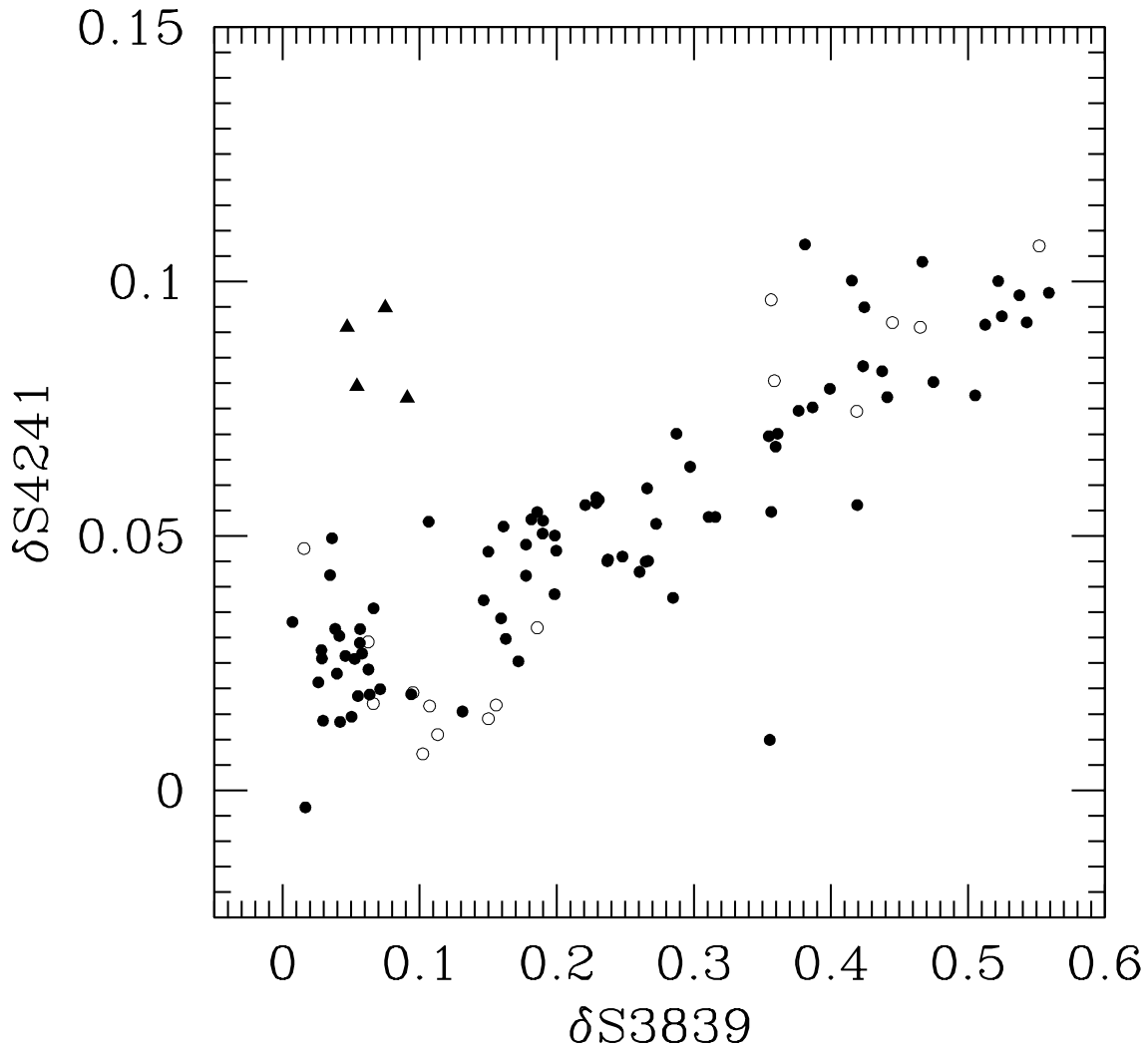


Figure 3.3 : Comparison of the CN indices $\delta S(3839)$ and $\delta S(4142)$. Both indices, which measure absorption by the same molecule, are well-correlated. Symbols are the same as in Fig. 3.1.

determine the centers of the absorption lines. We found four stars with notably different radial velocities from the rest of our sample; they have magnitudes from $V = 19$ mag to $V = 20.25$ mag. These stars (number 3206, 4592, 5296, and 6335 in Table 1) could be SMC members from their location in the CMD, but since they are among the fainter stars in our sample the measured RVs could be affected by errors.

3.4.4 A correlation between CN absorption bands

As a diagnostic we plot $\delta S(3839)$ vs. $\delta S(4142)$ in Fig. 3.3. Again, stars having spectra with some ambiguities (quality class “1”) are plotted with open circles. The outstanding group of four stars at $\delta S(3839) \sim 0.08$ and $\delta S(4142) \sim 0.08$ (plotted with filled triangles) are the stars

noted in Section 3.4.3 as having radial velocities well off the measured RV distribution of 47 Tuc and are probably not cluster members. Although there is scatter present, the correlation between the two CN indices stands out. The star at $\delta S(3839) = 0.35$ and $\delta S(4142) = 0.01$ that does not follow the correlation is the reddest SGB star (compare to Fig. 3.1). Since the $\delta S(4142)$ index is less sensitive to CN abundance, and in any event correlates with $\delta S(3839)$, we will concentrate on the $\delta S(3839)$ index in the remainder of this study.

3.5 CN variations on the main sequence

In the lower panel of Fig. 3.2 the $\delta S(3839)$ index is plotted versus the stellar V band magnitudes. A pronounced variation in the measured CN index across the whole luminosity range covered is obvious. Even more, the distribution of CN absorption strength is bimodal: stars seem to be either CN-strong or CN-weak. There might be a possible turn-over at the faint end of our sample, although this could be an effect of increasing measurement errors. Our data demonstrate that CN variations exist in 47 Tuc even 2.5 mag below the MSTO. The range of the CN variations becomes more evident for lower luminosities ($V \geq 18.5$), which is probably an effect of the decreasing surface temperature and therefore increased efficiency of molecule formation. Rose (1984) showed for a sample of nearby dwarf stars that from spectral type G0 to K the CN 3883 band strength steadily increases, with the metal-richer stars showing a steeper increase as a function of spectral type. The increasing amplitude of the bimodal CN distribution is also evident in the less sensitive $\delta S(4142)$ index in Fig. 3.2 (lower panel). Note that this effect was not seen in the study of Cannon et al. (1998), which only extends to a magnitude of $V = 18.6$ mag. At this luminosity the bifurcation of the CN band strength starts to increase. In Fig. 3.4 we show spectra of CN-strong and CN-weak stars in three luminosity bins. Differences in CN band absorption are clearly visible, which was also seen in Fig. 3.2. We wish to point out here that at the luminosity of $V \sim 19.25$ the CN-weak sample suffers from SMC field star contamination. The two faintest stars with good quality spectra have luminosities of $V = 19.25$ mag. CN-weak stars fainter than this luminosity still have reliable spectra, albeit of more limited S/N. Nevertheless, a verification by additional observations appears appropriate.

3.5.1 A Test of the CN Bimodality

The bimodality of the CN absorption strength is an outstanding feature of the main sequence of 47 Tuc. A bimodal CN distribution has been reported previously for the RGB, the SGB and the turn-off region (e.g., Norris & Freeman 1979, Cannon et al. 1998, and references therein). In Fig. 3.5 we plot histograms of the CN band strength $\delta S(3839)$ for magnitude ranges $V \leq 18.5$ mag and $V \geq 18.75$ mag. The thick line is a smoothed plot of the $\delta S(3839)$ values, where each measurement was folded by a Gaussian having a width equal to the error bar. The division into two luminosity bins is motivated by the increased absorption strengths of CN-enriched stars fainter than $V = 18.5$ mag. A histogram of the CN absorption strength of all stars would smear out the bimodality due to the different range in index values at different magnitudes.

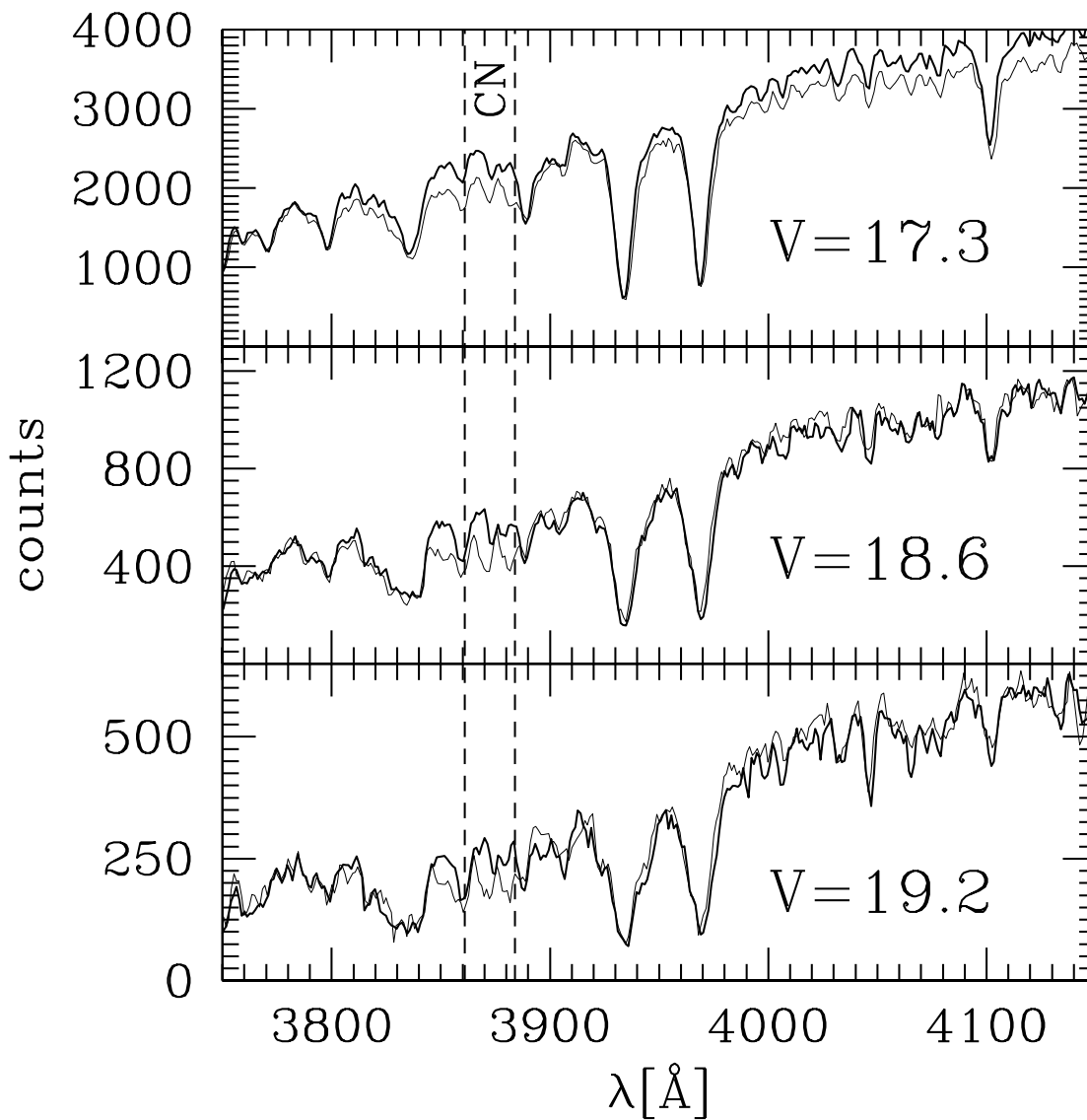


Figure 3.4 : Demonstration of the different CN absorption band strengths at 3883\AA (between the dashed lines). We show example spectra of CN-strong (thin lines) and CN-weak (thick lines) stars at three different V magnitudes. The stars plotted are #806, #3060, #4344, #5545, #5759, and #5809.

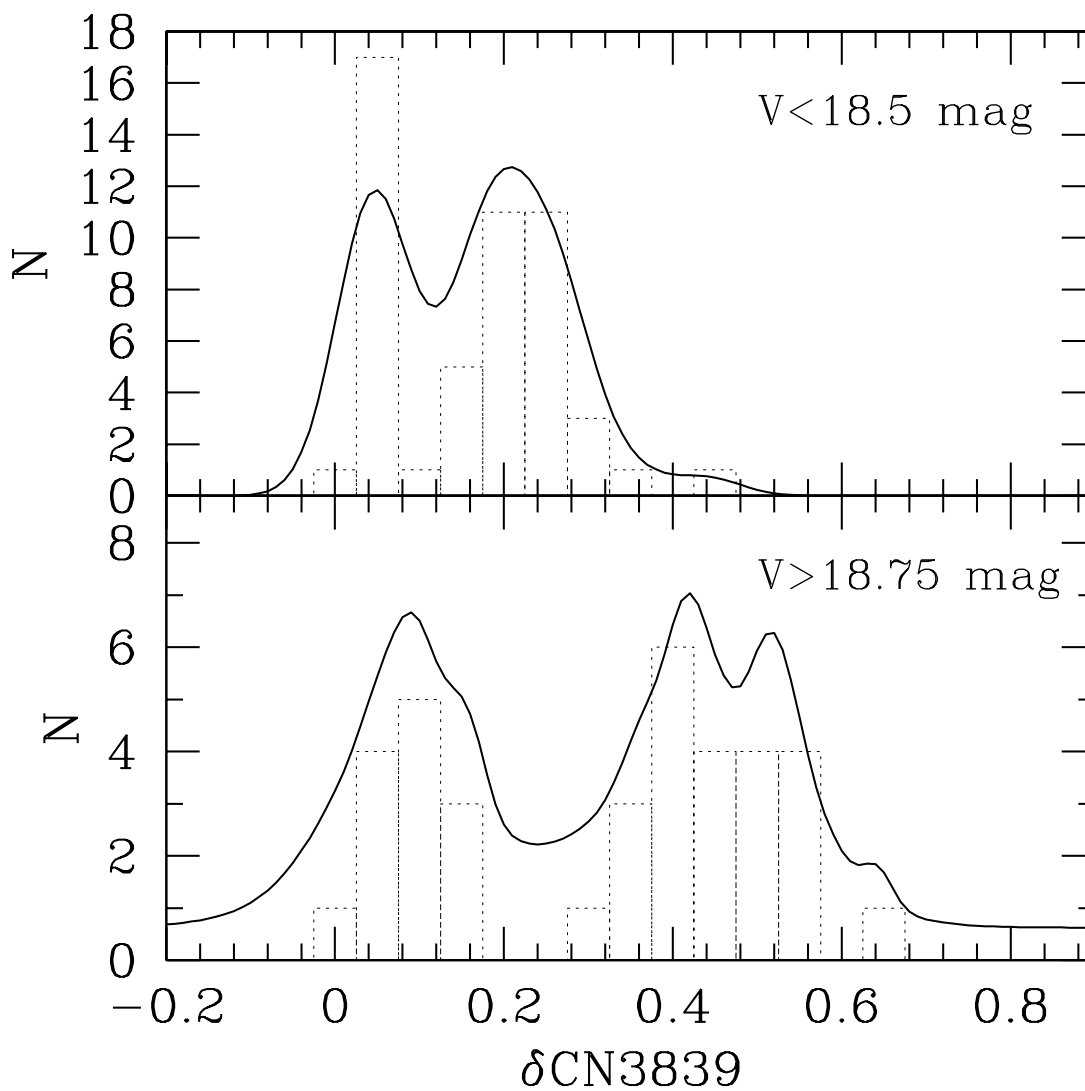


Figure 3.5 : *Distribution of the CN absorption strengths $\delta S(3839)$ for stars brighter than $V = 18.5$ mag (upper panel) and fainter than $V = 18.75$ mag (lower panel). The histogram bars show absolute number counts. The thick line is an error-folded density plot of the $\delta S(3839)$ distribution. The bimodality of the distributions stands out in both sub-samples.*

We quantify the significance of this bimodality with a *kmm*-test (Ashman, Bird, & Zepf, 1994). For the bright and faint samples we obtain confidence levels of 99.996 % and 99.999 % respectively for the distributions to be bimodal. This is very significant (indeed, the significance for the faint sample reached the numerical accuracy of the program used to calculate it).

In order to double-check if the bimodal distribution of CN strength could be caused by observational effects or errors in the data reduction, we plot the Ca H+K index defined in equation (4) versus the stellar V magnitude in Fig. 3.6. Higher values of HK indicate stronger calcium absorption. No bifurcation as for the CN indices is apparent. In this plot we mark CN-rich and CN-poor stars with filled and open circles, respectively. Although there is no clear trend, CN-poor stars might tend to have higher HK absorption and vice versa, but this effect is within the errors of the index measurements. We conclude that there is no obvious effect in the data that could mimic the bimodal distribution in the CN absorption strengths.

3.5.2 The CN/CH anti-correlation

In 47 Tuc an anti-correlation between CN and CH absorption band strength was reported in earlier studies of red giants (Norris, Freeman, & Da Costa 1984; Briley et al. 1994, and references therein). Such an anti-correlation indicates that an enhancement of CN coincides with a decrease in CH, or with a depletion of carbon at the expense of nitrogen. Such an anti-correlation is expected if CN variations are caused by variable amounts of CNO cycle processing. If the CNO process only alters the ratio of the CNO elements, the sum C+N+O must stay constant. An increase of nitrogen at the cost of carbon would (to a certain limit) increase the CN abundance but decrease the absolute content of carbon. As a result, the formation of the CH molecule would be suppressed.

In Fig. 3.7 we plot the measured CH(4300) index versus the V band magnitude for all stars with good spectra (quality flag = “0”). Stars classified as CN-strong are plotted with filled circles, CN-weak stars are drawn with open circles. It is evident that stars with the strongest CH bands are weak in CN absorption. For the faintest stars in the sample ($V \geq 19.5$) this anti-correlation does not stand out clearly; we find that increasing absorption line strengths for these cooler stars affects the measurement of the comparison regions in the CH index.

3.6 Summary and Conclusions

Bimodal CN variations are detected in 47 Tuc among main sequence stars with masses down to $0.65 M_{\odot}$ or 2.5 mag below the MSTO. This extends earlier studies to stars that are nearly 1.5 magnitudes fainter. There is an anticorrelation between the CN and CH absorption strengths on the main sequence of 47 Tuc.

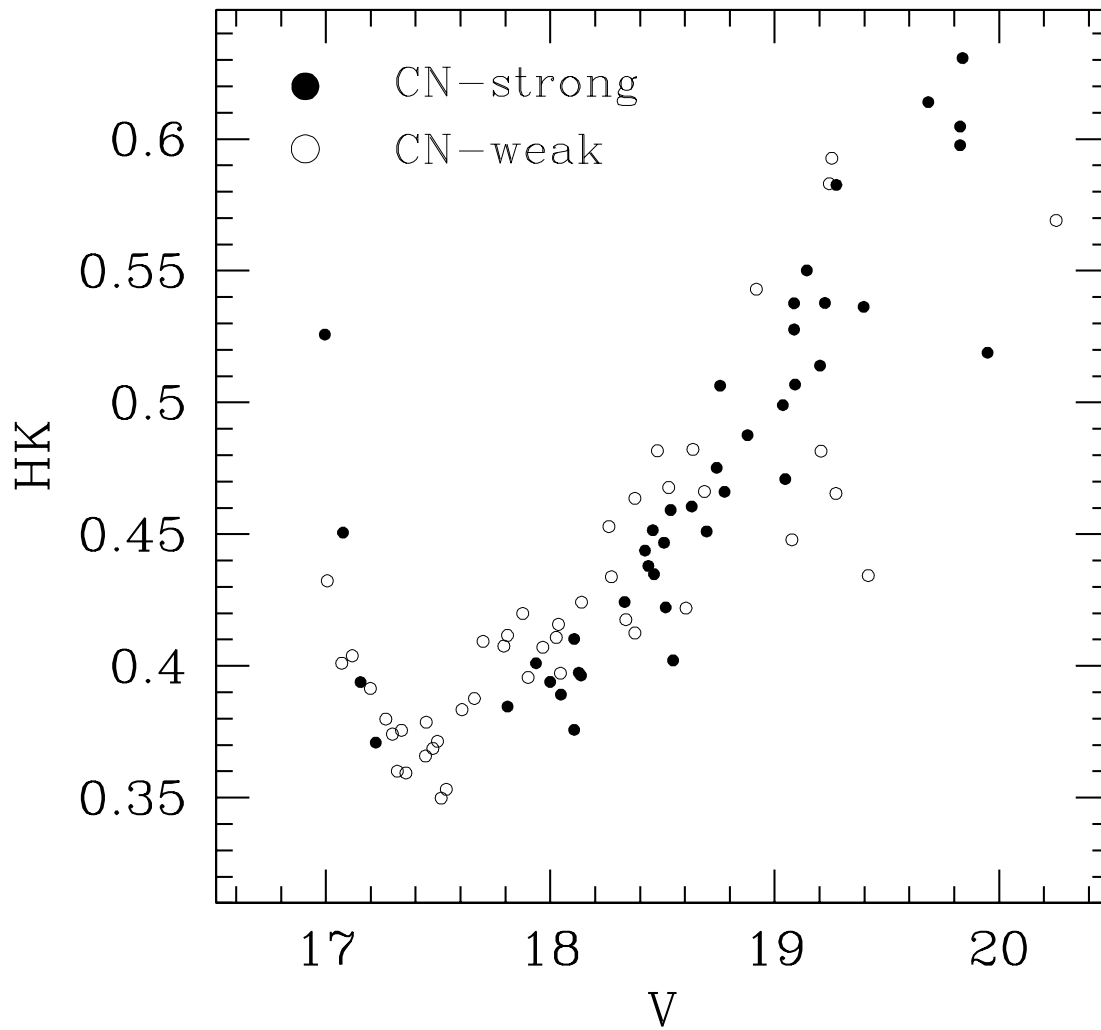


Figure 3.6 : Distribution of Ca H+K absorption strength as a check of the data reduction. No bimodality such as for the CN distribution is seen, but a very weak anti-correlation between the CN and HK absorption.

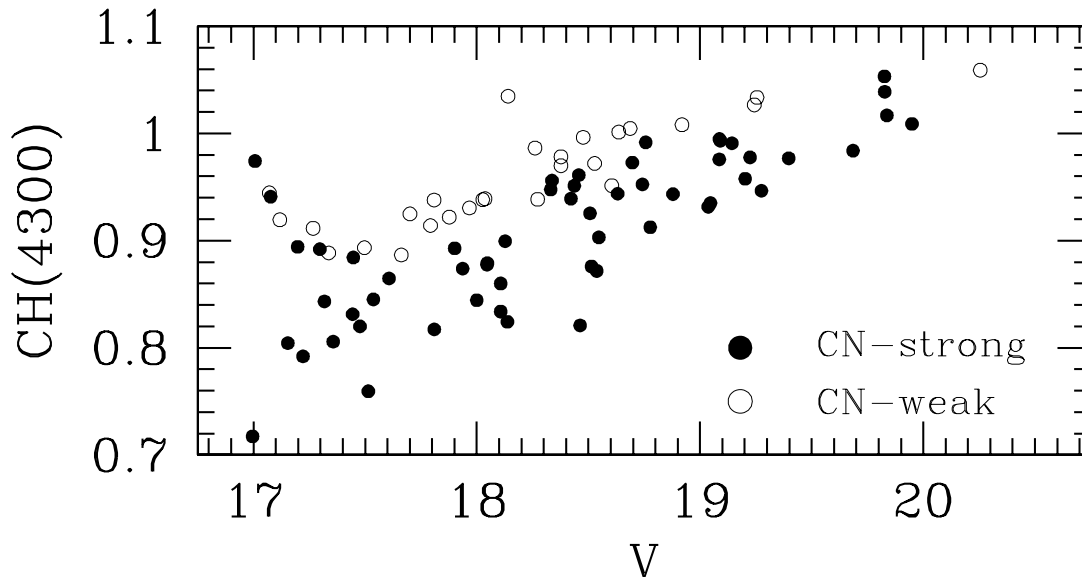


Figure 3.7 : $CH(4300)$ index plotted vs. the stellar magnitude for all stars with clean CN measurements (quality = “0”). Stars classified as CN-strong are plotted with filled circles; CN-weak stars are plotted with open circles. Note that all CN-weak stars have strong CH absorption.

3.6.1 External vs. evolutionary scenarios

In Section 3.1 we argued that for stars 2.5 mag below the MSTO the CNO-cycle contribution is reduced by at least a factor of ten relative to the MSTO. Despite the fact that the faint stars in our sample should not be able to alter their chemical composition by themselves (by CNO-cycling plus mixing processes), they still show clear and significant star-to-star CN variations. Evidently the internal stellar evolution scenario seems to be ruled out, at least as the *only* explanation for the CN-variation phenomenon in 47 Tuc. It is important to mention that from the tip of the RGB to the faint main sequence both (i) a bimodal CN distribution, and (ii) a CN/CH anti-correlation, are found in 47 Tuc. This suggests that the same effect causes the abundance spread from the tip of the RGB to the faint main sequence.

A caveat of our results is that an increased CN formation efficiency in the cooler atmospheres of the faint MS stars may compensate for any vanishing scatter in the CN content. The greater separation between CN-strong and CN-weak stars at the faint end of our sample in Fig. 3.2 may indicate that this effect is important. We plan to investigate temperature effects on CN formation in our sample by model atmosphere calculations in a future paper; preliminary results presented in the appendix of this chapter demonstrate that the CN scatter at the faint end of our sample is driven by abundance spreads. Additional observations would help to make our result more secure: for stars just one magnitude fainter than our sample the efficiency of the CNO-cycle relative to the pp-chain drops down by another factor of ten. Any diminution in the effects of internal evolution on the behaviour of CN would be even more evident among such stars than in our current study.

If internal stellar evolution can be ruled out, external scenarios remain to be discussed;

either self-enrichment during the star forming episode of 47 Tuc or later self-pollution. However, early self-enrichment by high-mass stars is unlikely to produce only an imprint in the lighter elements like CNO. Self-pollution by high-mass AGB stars on the other hand could explain the lack of abundance variations in the heavy elements (e.g., as discussed in Cannon et al. (1998)). However, the bimodality of the CN band strength still needs to be explained, and the AGB-star enrichment/pollution scenario is not without other challenges (Denissenkov et al., 1997).

3.6.2 On the origin of the bimodality

Current scenarios can hardly explain all aspects of the bimodal distribution of CN absorption strengths in 47 Tuc or in other GCs. For example, it is not clear how internal pollution by AGB winds would lead to a bimodal abundance distribution. The measured bimodal CN distribution does not necessarily reflect a bimodal abundance spread: the distribution of CN absorption strengths reflects the true distribution of atomic abundances folded with the curve of growth (COG). It might be that all CN enhanced stars in 47 Tuc are polluted, but they would fall on the flat part of the COG. A continuum of atomic carbon and nitrogen abundances could therefore lead to more or less the same CN absorption strength at a given effective temperature. Such a “saturation” of the CN S(3839) band was proposed by Suntzeff (1981) and Langer (1985) to explain the bimodality of CN absorption in GC RGB stars. The similarity of CN absorption strength for the CN-rich stars might be explained by this saturation scenario, but the homogeneity of CN strength of the CN-poor stars remains unsolved: These stars would fall on the raising part of the COG; if pollution leads to a spread of abundances one would expect a continuum of CN absorption strength until the flat part of the COG is reached. This is not seen in the bimodal CN distribution of 47 Tuc. If indeed saturation happens for the CN-strong stars, then the CN-weak stars may represent the unpolluted, chemically homogeneous fraction of the cluster whose CN abundance falls on the raising part of the COG. Due to their chemical homogeneity they would have the same CN absorption strengths at a given effective temperature. The bimodal pollution mechanism still remains to be explained.

Binarity combined with AGB star pollution might be a solution: Only stars in binary systems would have experienced pollution by accreting the stellar winds of their evolving higher mass AGB companion. If single stars accreted only a negligible fraction of intracluster gas during the AGB contamination phase, the bimodality in the CN distribution would simply reflect the binary fraction in the globular cluster. If pollution in binary systems played an important role in GCs, one might also expect to find a significant number of CH stars. However, despite intense searches only a handful of CH stars have been found so far (e.g., Côté et al. 1997 and references therein).

3.6.3 Where is the polluting gas?

If self-pollution happened in globular clusters, should the polluting gas still be visible? The present-day amounts of gas in GCs appear to be extremely small and below the detection lim-

its of classical approaches. Recently, ionized gas was detected in 47 Tuc from the measured radio dispersion of millisecond pulsar signals (Freire et al., 2001). The authors estimate the total gas mass in the cluster's center to be roughly $0.1 M_{\odot}$. This amount is only a thousandth of the expected gas loss from stellar winds that should be ejected into the cluster between two passages through the Milky Way disk; therefore effective mechanisms must be at work to expel the gas. Freire et al. (2001) argue that only 0.5% of the spin-down energy from the known millisecond pulsars in 47 Tuc would be required to expel this large an amount of gas from the cluster. Other mechanisms like novae and hot post-horizontal branch stars have also been under discussion as responsible for the mass loss from globular clusters. Smith (1999) showed that fast stellar winds ejected by main sequence stars can contribute to the gas loss. Therefore, at the present time pollution seems unlikely to happen. The crucial question then is whether during the era when intermediate mass stars evolved to AGB stars material from their stellar winds could have been retained in the globular cluster and have been re-accreted by other stars including the low-mass main-sequence stars that are observed at the present time. The mechanisms that are responsible for the ejection of stellar winds out of globular clusters were likely already at work in ancient times. Pulsars can form from stars with $M=10$ to $25 M_{\odot}$; therefore many of them should have already formed by the time that $5 M_{\odot}$ stars ejected their winds. Also main sequence star winds should have been present in ancient times. Nonetheless, Thoul et al. (2002) show that the overwhelmingly largest part of the gas from stellar winds is ejected within the first Gyr after the birth of a GC, so that the accretion scenario may be feasible in earlier times of cluster evolution.

3.6.4 Other support for external pollution scenarios

We have demonstrated that internal stellar evolution is unlikely to be the dominant origin of the CN variations in 47 Tuc. While primordial variations also have problems, the pollution scenario has its attractions, although it remains unproven.

Recent work by other groups add strong arguments that external enrichment processes can cause chemical inhomogeneities in GCs: from high-resolution spectroscopy Gratton et al. (2001) found a Mg-Al anti-correlation among turn-off stars in NGC 6752. The core temperatures of turn-off stars are too low to allow the proton capture process to convert Mg to Al and cause this anti-correlation. The authors conclude that internal mixing scenarios cannot account for the chemical inhomogeneities in this globular cluster (which also exhibits a bimodal CN distribution on the RGB; Norris et al. 1981). They propose external enrichment by AGB stars as the mechanism at work (see also Ventura, D'Antona, Mazzitelli, & Gratton 2001). In this regard, it is important to note that Briley et al. (1996) had earlier shown that Na abundance inhomogeneities exist among main sequence stars in 47 Tuc. Indeed, the relative behavior of CN-Na-Mg-Al has a rich literature that we have not delved into here. The review by Kraft (1994) provides a good introduction. Detailed abundance analysis of RGB stars in ω Cen has revealed imprints of supernova Type Ia enrichment processes (Pancino et al., 2002), but Cunha et al. 2002 argue against this enrichment mode. Furthermore, the mostly metal-poor ω Cen also contains a metal-rich stellar population (e.g., Pancino et al. 2000) and has consequently been proposed to be the core of a disrupted dwarf galaxy (e.g.,

Freeman 1993; Hughes & Wallerstein 2000; Gnedin et al. 2002). As such, it may be an atypical example of self-enrichment processes in a globular cluster.

The question of the origin of the polluting gas in 47 Tuc can be addressed by searching for the fingerprints of different enrichment processes: cluster self-enrichment by massive stars versus accretion of material ejected in winds from intermediate-mass stars. Do the CN-strong main sequence stars have abundance enhancements in the elements Na, Mg, and Al, which can be produced by proton-addition reactions in intermediate-mass red giants, or by carbon burning in even more massive stars? Do they show enhancements in the much heavier r- and s-process elements such as Ba and Sr? High resolution spectroscopy might provide answers to these questions.

Table 3.1 : D P S 47 T

ID	α_{2000}	δ_{2000}	V	$(B - V)$	$\delta S(3839)$	$\delta S(4142)$	CH(4300)	HK	Flag ^a
90	00 26 05.54	-71 58 30.50	19.567	0.791	0.062	0.032	1.057	0.614	1
94	00 26 12.36	-71 58 11.10	18.547	0.561	0.360	0.053	0.896	0.402	0
341	00 26 03.55	-72 01 13.10	17.447	0.494	0.159	0.026	0.879	0.379	0
596	00 26 05.55	-71 58 34.20	19.547	0.742	0.102	0.011	1.050	0.617	1
806	00 26 43.04	-71 56 15.50	19.224	0.697	0.415	0.102	0.969	0.538	0
977	00 26 04.52	-72 02 44.60	18.697	0.610	0.316	0.047	0.969	0.451	0
1152	00 26 10.13	-72 02 32.40	19.207	0.725	0.869	-0.035	0.893	0.697	2
1173	00 26 20.17	-71 52 12.50	17.662	0.514	0.030	-0.003	0.885	0.388	0
1304	00 26 15.29	-71 50 28.80	17.537	0.524	0.200	0.032	0.839	0.353	0
1329	00 26 33.55	-71 50 10.70	18.273	0.587	0.066	0.022	0.938	0.434	0
1351	00 26 50.58	-71 49 47.80	17.793	0.544	0.028	0.019	0.914	0.408	0
1366	00 26 16.10	-72 02 15.30	20.247	0.891	0.249	0.083	0.824	0.394	0
1462	00 25 59.22	-72 02 07.50	18.137	0.511	0.273	0.059	0.811	0.396	0
1498	00 26 55.20	-71 47 39.40	17.514	0.481	0.172	0.007	0.763	0.350	0
1587	00 25 58.24	-72 01 54.50	17.967	0.560	0.035	0.026	0.926	0.407	0
1675	00 26 10.83	-72 01 42.90	18.427	0.561	-0.124	-0.021	1.059	0.817	2
1833	00 26 04.95	-72 01 24.10	19.707	0.758	0.056	0.022	1.055	0.597	2
1890	00 26 03.53	-72 01 16.10	17.727	0.527	0.420	-0.002	0.919	27.031	2
1992	00 26 10.19	-72 01 03.10	18.687	0.593	0.163	0.018	1.007	0.466	0
2060	00 25 56.72	-72 00 53.80	18.047	0.544	0.221	0.051	0.870	0.389	0
2186	00 26 04.69	-72 00 38.90	18.777	0.594	0.399	0.092	0.897	0.466	0
2284	00 26 01.69	-72 00 26.30	19.827	0.759	0.559	0.121	1.027	0.605	0
2379	00 26 09.14	-72 00 15.60	18.331	0.519	0.285	0.035	0.943	0.424	0
2409	00 26 09.15	-72 00 11.90	17.077	0.561	0.265	0.040	0.937	0.451	0
2556	00 26 09.91	-71 59 51.20	19.097	0.693	0.095	0.009	1.048	0.583	1
2629	00 26 05.13	-71 59 41.50	18.037	0.527	0.042	0.008	0.939	0.416	0
2738	00 26 05.38	-71 59 29.00	19.837	0.841	0.538	0.111	1.008	0.631	0
2821	00 26 12.39	-71 59 16.00	19.037	0.676	0.467	0.110	0.916	0.499	0
2947	00 26 09.49	-71 59 00.00	18.477	0.577	0.071	0.012	0.999	0.482	0
3060	00 25 59.94	-71 58 45.80	17.337	0.511	0.038	0.019	0.887	0.376	0
3137	00 26 31.88	-71 58 33.10	17.071	0.542	0.042	0.017	0.944	0.401	0
3206	00 26 11.39	-71 58 22.50	19.417	0.676	0.091	0.090	0.862	0.434	0
3230	00 26 11.42	-71 58 19.60	18.977	0.660	0.098	0.177	-0.161	0.594	2
3343	00 26 28.31	-71 58 02.60	18.514	0.575	0.361	0.080	0.860	0.422	0
3371	00 26 10.95	-71 57 58.40	17.297	0.527	0.147	0.034	0.888	0.374	0
3394	00 26 29.74	-71 57 55.60	18.742	0.635	0.387	0.068	0.943	0.475	0
3456	00 26 10.89	-71 57 47.30	19.397	0.759	0.016	0.034	1.045	0.591	1
3521	00 26 28.20	-71 57 37.10	18.337	0.597	0.198	0.035	0.955	0.418	0

^aQualityflag: 0=good quality spectra; 1=some ambiguities; 2=poor quality spectra - unreliable.

Table 3.1 : D P S (continued)

ID	α_{2000}	δ_{2000}	V	(B - V)	$\delta S(3839)$	$\delta S(4142)$	CH(4300)	HK	Flag ^a
3522	00 26 34.72	-71 57 36.90	19.826	0.754	0.437	0.120	1.039	0.598	0
3532	00 26 05.67	-71 57 36.70	17.267	0.511	0.056	0.018	0.910	0.380	0
3631	00 26 00.64	-71 57 23.40	19.497	0.808	0.359	0.100	0.994	0.655	1
3701	00 26 04.00	-71 57 12.40	19.087	0.676	0.423	0.084	0.985	0.528	0
3769	00 26 00.29	-71 57 01.90	18.107	0.527	0.267	0.032	0.850	0.410	0
3797	00 26 35.15	-71 56 58.20	17.809	0.536	0.053	0.007	0.940	0.411	0
3823	00 26 35.60	-71 56 54.80	18.140	0.597	0.151	0.015	1.059	0.429	0
3853	00 26 06.92	-71 56 50.60	18.127	0.544	0.237	0.037	0.893	0.397	0
3872	00 26 42.89	-71 56 47.70	18.261	0.617	0.057	0.018	0.989	0.453	0
3929	00 26 02.24	-71 56 40.30	19.297	0.742	0.156	0.007	1.050	0.571	1
3942	00 26 23.93	-71 56 38.10	19.270	0.773	0.066	0.028	1.014	0.543	1
4014	00 26 11.53	-71 56 27.90	18.027	0.544	0.063	0.006	0.940	0.411	0
4019	00 26 30.36	-71 56 26.60	19.824	0.849	0.113	-0.001	1.019	0.595	2
4023	00 26 13.09	-71 56 26.50	19.482	0.772	0.465	0.109	0.983	0.548	1
4115	00 26 11.27	-71 56 12.60	17.877	0.527	0.058	0.016	0.919	0.420	0
4188	00 26 12.11	-71 56 03.10	19.687	0.758	0.150	0.040	1.054	0.723	1
4298	00 26 54.92	-71 55 44.30	18.422	0.608	0.287	0.068	0.928	0.444	0
4344	00 26 33.67	-71 55 37.70	17.607	0.527	0.150	0.035	0.859	0.383	0
4421	00 26 34.06	-71 55 26.00	18.631	0.602	0.376	0.066	0.934	0.461	0
4452	00 26 17.37	-71 55 21.80	18.605	0.547	0.017	-0.014	0.953	0.422	0
4465	00 26 17.62	-71 55 19.90	18.463	0.607	0.441	0.108	0.800	0.435	0
4521	00 26 33.71	-71 55 12.00	19.202	0.694	0.424	0.115	0.946	0.514	0
4554	00 26 36.04	-71 55 06.40	16.996	0.671	0.341	0.041	0.781	0.532	0
4592	00 26 47.32	-71 55 00.60	19.273	0.732	0.054	0.087	0.834	0.465	0
4600	00 26 42.57	-71 54 59.70	18.777	0.594	0.107	0.004	1.037	0.483	1
4643	00 26 54.87	-71 54 52.20	17.497	0.527	0.007	0.018	0.890	0.371	0
4707	00 26 46.78	-71 54 42.90	18.000	0.529	0.266	0.061	0.832	0.394	0
4790	00 26 56.83	-71 54 27.50	18.437	0.577	0.237	0.028	0.947	0.438	0
4877	00 26 46.37	-71 54 14.00	18.457	0.659	0.297	0.052	0.956	0.452	0
4936	00 26 53.02	-71 54 03.20	17.937	0.544	0.248	0.041	0.866	0.401	0
5049	00 26 50.13	-71 53 43.50	17.007	0.626	0.199	0.023	0.973	0.432	0
5146	00 26 54.38	-71 53 26.80	19.949	0.851	0.357	0.044	1.006	0.519	0
5154	00 26 48.22	-71 53 26.00	18.377	0.561	0.040	-0.004	0.973	0.413	0
5188	00 27 04.02	-71 53 18.70	17.357	0.527	0.181	0.054	0.795	0.359	0
5205	00 26 19.88	-71 53 16.60	17.222	0.513	0.231	0.058	0.775	0.371	0
5214	00 26 51.50	-71 53 13.20	19.731	0.688	0.388	4.746	0.799	0.401	0
5219	00 26 20.25	-71 53 13.50	18.528	0.589	0.026	0.005	0.971	0.468	0
5231	00 26 51.88	-71 53 10.60	18.737	0.626	0.445	0.113	1.024	0.552	1
5235	00 26 56.51	-71 53 09.80	19.847	0.841	0.172	-0.007	1.041	0.628	2

^aQualityflag: 0=good quality spectra; 1=some ambiguities; 2=poor quality spectra - unreliable.

Table 3.1 : D P S (continued)

ID	α_{2000}	δ_{2000}	V	$(B - V)$	$\delta S(3839)$	$\delta S(4142)$	CH(4300)	HK	Flag ^a
5237	00 26 31.91	-71 53 09.50	19.255	0.744	0.046	0.007	1.040	0.593	0
5253	00 26 36.09	-71 53 07.60	18.879	0.658	0.475	0.069	0.932	0.488	0
5261	00 26 21.88	-71 53 06.80	20.255	0.864	0.161	0.041	1.066	0.569	0
5296	00 27 15.20	-71 52 58.70	19.077	0.676	0.047	0.082	0.850	0.448	0
5299	00 26 23.93	-71 53 00.30	19.153	0.668	0.113	0.011	1.046	0.591	1
5342	00 27 03.51	-71 52 51.40	17.477	0.511	0.178	0.029	0.813	0.369	0
5381	00 26 54.82	-71 52 42.70	19.047	0.676	0.419	0.048	0.936	0.471	0
5402	00 26 35.43	-71 52 38.60	18.377	0.610	0.053	0.021	0.977	0.464	0
5538	00 27 02.38	-71 52 12.80	18.317	0.577	0.186	0.022	0.959	0.428	1
5545	00 26 35.31	-71 52 11.50	18.636	0.638	0.063	0.006	1.004	0.482	0
5547	00 26 52.68	-71 52 10.60	19.397	0.775	0.643	0.136	0.954	0.536	0
5587	00 26 44.72	-71 52 01.60	17.701	0.549	0.029	0.013	0.926	0.409	0
5653	00 26 30.71	-71 51 47.60	18.046	0.562	0.190	0.038	0.871	0.397	0
5665	00 26 33.74	-71 51 43.60	17.154	0.544	0.229	0.061	0.790	0.394	0
5759	00 26 14.33	-71 51 26.10	17.318	0.514	0.178	0.036	0.836	0.360	0
5809	00 26 48.71	-71 51 16.90	19.243	0.724	0.050	0.006	1.035	0.583	0
5836	00 26 35.80	-71 51 11.60	18.757	0.658	0.311	0.036	0.991	0.506	0
5942	00 26 52.82	-71 50 48.50	19.143	0.740	0.525	0.099	0.980	0.550	0
5950	00 26 33.32	-71 50 47.50	19.096	0.716	0.420	0.530	-0.000	-0.000	2
6043	00 26 48.02	-71 50 24.60	17.810	0.527	0.229	0.064	0.803	0.385	0
6047	00 26 51.54	-71 50 23.80	17.118	0.562	0.036	0.029	0.917	0.404	0
6220	00 26 39.76	-71 49 42.70	18.537	0.691	0.381	0.103	0.856	0.459	0
6248	00 26 52.04	-71 49 35.70	18.919	0.734	0.094	0.009	1.014	0.543	0
6264	00 26 40.87	-71 49 33.80	19.871	0.757	0.419	0.112	0.978	0.671	1
6335	00 27 02.56	-71 49 16.80	19.207	0.699	0.075	0.093	0.812	0.482	0
6380	00 26 50.93	-71 49 09.30	19.685	0.735	0.513	0.111	0.976	0.614	0
6452	00 26 48.80	-71 48 50.70	18.507	0.626	0.355	0.037	0.922	0.447	0
6455	00 26 58.61	-71 48 49.70	17.901	0.574	0.190	0.030	0.888	0.396	0
6537	00 26 32.22	-71 48 29.00	17.198	0.549	0.106	0.042	0.887	0.391	0
6591	00 26 55.56	-71 48 14.60	17.444	0.534	0.186	0.034	0.823	0.366	0
6622	00 27 09.57	-71 48 04.80	21.893	0.219	0.071	-0.039	0.729	0.272	2
6641	00 27 13.08	-71 48 00.70	19.275	0.739	0.522	0.106	0.931	0.583	0
6648	00 26 45.61	-71 47 59.50	19.091	0.684	0.505	0.088	0.980	0.507	0
6723	00 26 48.58	-71 47 39.90	19.086	0.693	0.543	0.056	0.973	0.538	0

^aQualityflag: 0=good quality spectra; 1=some ambiguities; 2=poor quality spectra - unreliable.

3.7 Appendix: Calibration of CN and CH indices on the Main Sequence of 47 Tuc

During the 2003 AAS winter meeting Mike Briley compared the CN and CH absorption strengths that we measured for 47 Tuc stars with indices derived from model atmospheres. Our observations are reproduced perfectly, and although this is work in progress, we will shortly summarize preliminary results here. Results are to be published in Harbeck, Briley, Smith & Grebel 2003, ApJL, in preparation.

A vanishing intrinsic abundance spread for the fainter MS stars of 47 Tuc (this would be expected if internal nucleosynthesis and mixing are causing the star-to-star CN variations observed in 47 Tuc) might be hidden by an increased CN and CH molecule formation efficiency in the atmospheres of the cooler stars. The observation of a spread in CN and CH molecule absorption strengths at the faint end of our sample therefore unfortunately inherits the ambiguity of the molecule formation process. It is therefore important to model the CN and CH molecule formation process in the stellar atmospheres.

Model atmospheres for stars on the fiducial of the main sequence were calculated using the MARCS program (Gustafsson et al., 1975) and converted into spectral energy distributions with the spectrum generating program SSG (Bell & Gustafsson, 1978). See Briley & Cohen (2001) for a detailed description of the modeling process. Two sets of models were created to describe both CN-weak and CN-strong stars, where the CN abundances were set to $[C/Fe]=0.0$, $[N/Fe]=0.4$ and $[C/Fe]=-0.3$, $[N/Fe]=1.4$, respectively. Oxygen was fixed to $[O/Fe]=0.3$. Due to the small radial velocity of 47 Tuc, the oxygen abundance could not reliably be measured for 47 Tuc so far, since telluric oxygen lines overlap with stellar features. As the formation of CN has to compete with the formation of the tightly bound CO molecule, the oxygen abundance has to be included into the calculation of the CN absorption strength. From the model spectra we extracted the CN S(3839) and CH(4300) index in the same way as we did for the stellar spectra.

In Fig. 3.8 we plot the CN and CH absorption strength versus the stellar luminosity. The calculated absorption strengths of the model atmospheres are overplotted for the CN-strong and CN-weak model. The adopted model perfectly describes the dependence of the CN and CH indices on the stellar luminosity. Note that no artificial zeropoint correction was applied to the models.

We conclude that CN abundance variations persist among the faintest stars in our sample; the spread in C and N abundances is of the same amplitude at the MSTO as for the faintest stars investigated here. Thus, our conclusion that internal stellar processes can not be responsible for CN variations in 47 Tuc has been convincingly confirmed.

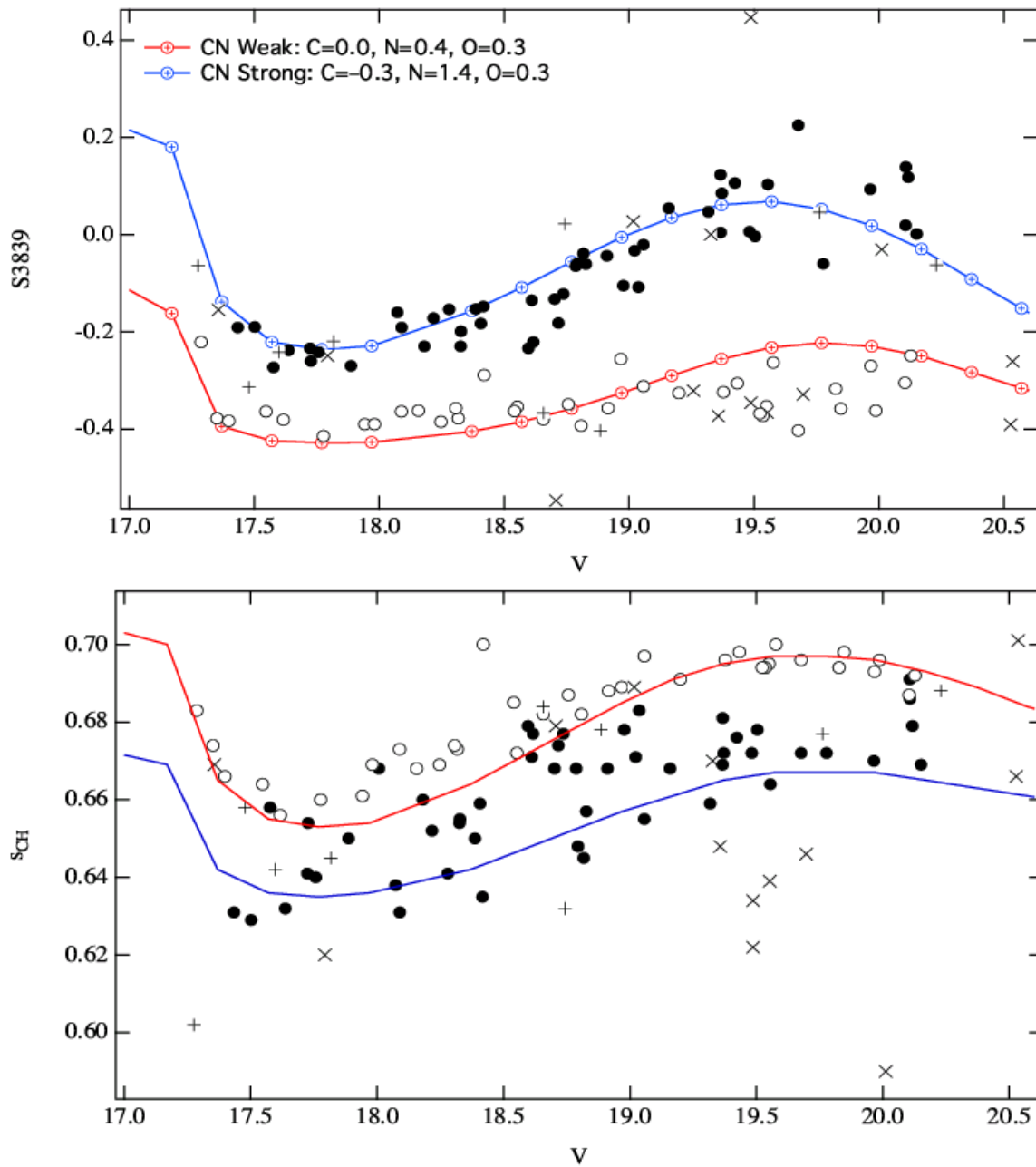


Figure 3.8 : $S(3839)$ and $CH(4300)$ indices of 47 Tuc stars plotted versus their luminosity. The red and blue lines describe the expected molecular absorption strengths from model atmospheres of best-fitting CNO abundances for CN-poor and CN-strong stars, respectively.

Chapter 4

Integrated spectra of the Second Parameter GCs M 13, M 3, and NGC 7006

Abstract

We present integrated spectra of the three globular clusters M 3, M 13, and NGC 7006. The effect of the horizontal branch morphology on the H_β , H_γ , and H_δ Balmer lines is studied. We find significant differences between Balmer line absorption strengths between M 13 and the two clusters NGC 7006 and M 3, fulfilling the predictions of the Lee, Yoon, & Lee (2000) model. The difference is more evident in the higher Balmer lines. We find that the integrated CH G-band absorption in the three clusters is the same, indicating that chemical inhomogeneities within the globulars have no effect on the integrated spectral energy distribution in the wavelength region that we have observed.

4.1 Introduction

How is the integrated energy distribution of globular clusters (GCs) affected by horizontal branch stars? Will the second parameter effect and internal star-to-star abundance variations leave a significant imprint on the integrated energy distribution of GCs? This question is of particular importance since all studies of unresolved stellar populations, e.g., of galaxies outside the Local Group or of unresolved GCs, depend on the interpretation of the integrated light emitted by these objects. Star clusters, and in particular old GCs, provide the observational reference frame of stellar population studies, because they are simple stellar systems consisting of stars of only one age and one metallicity, whose spectra are therefore amenable to modelling by libraries of synthetic stellar populations spectra (e.g., models by Bruzual & Charlot 1993). The existence of CNO abundance variations in GCs might imply that integrated properties of GCs, such as CN and CH molecular absorption bands, might also vary from cluster to cluster even if they have the same metallicity and age. Wirth (1985) found a large scatter in the integrated CN absorption strength of elliptical galaxies and suggested that the “variation in CN strength in ellipticals can be supposed to stem from the same effect that drives such variations in the CN features of globular cluster stars.” As the HB morphology

of GCs can differ from cluster to cluster at a given metal abundance, metallicity alone might not be sufficient to describe the integrated spectrum of an old stellar population. In particular Balmer line strengths and the UV flux of the spectral energy distribution (SED) will be affected by HB morphology.

A well established tool to interpret the integrated light of star clusters as well as of mixed stellar populations is the *Lick-index* system, which quantifies prominent absorption features in SEDs by spectral indices (Worthey et al., 1994). Studies of unresolved stellar populations suffer from a degeneracy in age and metallicity, as age and metallicity can change the SED in similar ways. Indices measuring the Balmer H_β as well as iron and magnesium line strengths play a key role in the study of elliptical galaxies and GCs, since the Balmer line strengths predominantly depend on the age of a stellar population, while iron and magnesium lines allow an independent determination of the metallicity. Strong H_β line absorption in elliptical galaxies is therefore often interpreted as an indication of an intermediate-age stellar population with ages from 1 Gyr to 10 Gyr (e.g., Faber et al. 1995). The index method finds a frequent application in the analysis of spectra of globular cluster systems as a means of identifying the epochs of GC formation in remote galaxies (e.g., Puzia et al. 1999; Schroder et al. 2002). In the context of large galaxy surveys the H_β lines are established tools to estimate luminosity-weighted ages of mixed stellar populations of galaxy samples (e.g., Trager et al. 2000a,b; Bernardi et al. 2003). However, Maraston & Thomas (2000) note that even a mixture of old stellar populations of different metallicities can produce the same Balmer line strength as an intermediate-age stellar population due to the contribution of blue HB stars to the integrated light. The age-metallicity degeneracy still remains an unsolved problem in the analysis of unresolved stellar populations.

The key assumption for the use of hydrogen absorption lines as an age dating tool is that these lines are produced in main sequence stars. Starting from old stellar populations with ages comparable to Milky Way GCs, with decreasing age the main-sequence turn-off (MSTO) will become brighter and bluer (i.e., higher effective temperature of the stars at the MSTO). As the stars become bluer, their Balmer line strengths will increase with a peak at a stellar color of $(B - V) \sim 0$. If stars become bluer and hotter than this, ionisation of hydrogen atoms decreases the formation of Balmer lines. A variable HB morphology for a stellar population of a fixed age and metallicity could substantially alter the total number of stars contributing to the generation of hydrogen absorption lines: for a very red morphology HB stars will barely contribute to the total Balmer line strengths. With increasingly bluer HB morphology, blue stars will add extra hydrogen absorption. For extremely blue HB morphologies, for which most HB stars are much bluer than $(B - V) = 0$, the hydrogen absorption strength will vanish. Lee, Yoon, & Lee (2000) investigated the influence of the HB morphology on the H_β Balmer line strength using synthesized SEDs. Their models find — at a given metallicity and age — the expected increase of the H_β line strength with increasing blueness of the HB, until H_β reaches a maximum strength and decreases for extremely blue HB types, see Fig. 4.1. In their calculation, Lee, Yoon, & Lee (2000) assume age as the driving second parameter of the HB morphology. Their models including the impact of HB stars on the Balmer lines are plotted with thick lines in Fig. 4.1, while a conventional model without taking into account HB stars is drawn with thin lines. Note the importance of HB stars in the models!

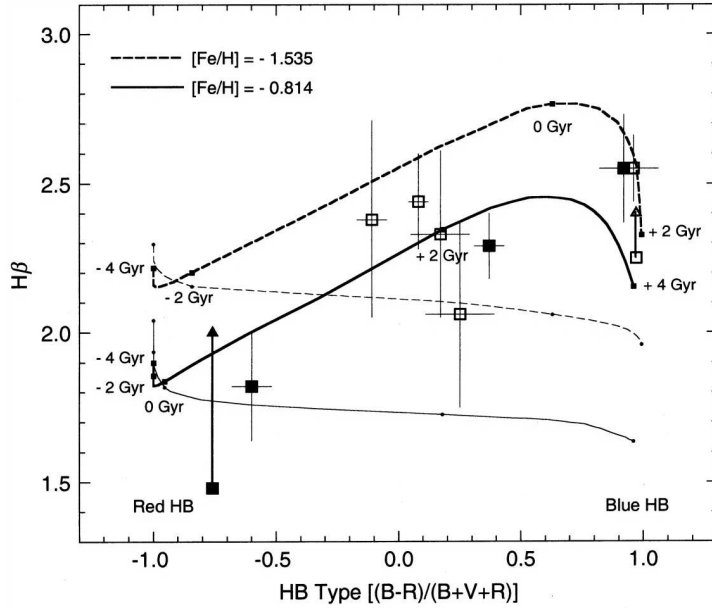


Figure 4.1 : Figure 7 of Lee, Yoon, & Lee (2000). Plotted is the expected H_{β} equivalent width at a given metallicity but different HB morphology (solid lines). The models include the effect of HB stars on the H_{β} -line formation (thick lines). For comparison, models without HB star contribution are plotted with thin lines. Models of two different metallicities are plotted with solid and dashed lines. The HB morphology is assumed to systematically vary with age (i.e., age as the only second parameter) as indicated by numbers in the graph. Reproduced with the kind permission of Lee.

Table 4.1 : L O .

Star cluster	[Fe/H]	Date	Exposure Time
NGC 7006	-1.63 dex	2001/06/15	3×900 s
M 3	-1.56 dex	2001/06/15	3×600 s
M 13	-1.57 dex	2001/06/14	3×600 s

In this chapter, we will investigate how the HB morphology and CNO abundance spreads influence the integrated spectra of GCs. We concentrate on the Balmer lines as they are important age-dating tools. The H_{β} line strengths have been studied for some GCs by Burstein et al. (1984). In particular we will investigate the dependence of the less established higher Balmer lines H_{γ} and H_{δ} on the HB morphology. We concentrate here on the three GCs M 3, M 13, and NGC 7006, for which we were able to obtain integrated spectra. All have a metallicity of $[Fe/H] \sim -1.6$ dex, but cover a wide range of HB morphologies (see Table 2.3). Motivated by the presence of star-to-star abundance variations within these clusters, we will also test if the integrated CH G-band absorption strength differs from cluster to cluster.

4.2 Data and Reduction

M 13, M 3, and NGC 7006 were observed in June 2001 at the Calar Alto 2.2m telescope with the Calar Alto Faint Object Spectrograph (CAFOS) in service mode¹. An overview of the observations is given in Tab. 4.1. We used a 9' long slit in combination with the GRISM B-100; at the slit width of 2" a spectral resolution of $R = 1000$ is achieved. The theoretically sampled wavelength range from $\sim 3200 \text{ \AA}$ to $\sim 6000 \text{ \AA}$ is reduced by the vanishing sensitivity of the CCD in the blue to $\sim 3700 \text{ \AA}$ to $\sim 6000 \text{ \AA}$. The spectra are sampled on the CCD with a resolution of $\sim 2 \text{ \AA}$ per pixel. At the beginning of each exposure the slit was positioned on the observed cluster such that the center of the GC fell on the first quarter of the slit. This method allows measurement of the sky on the edge of the scientific exposures (see Fig. 4.2). We applied an additional tracking during the exposure perpendicular to the spatial axis of the longslit. In this way, the slit is moved across the GC, evenly sampling different regions of it. The additional tracking speed was chosen such that during the exposure half of the core-radius was covered. This drift-scan technique prevents single bright stars from dominating the integrated spectrum of the GC.

During the observing campaign, bias and flat field frames were observed as well as HeCdHg arc lamps for wavelength calibration; all observations were bias-subtracted. Unfortunately, the flat field exposures contained no signal for wavelength shorter than 4500 \AA ! We assume that the quartz lamp used to illuminate the flat fields did not emit enough light in this wavelength range. Consequently, we *could not flat-field the spectra*. Since the GCs are extended objects, we may assume that pixel-to-pixel variations in the sensitivity cancel out once the long-slit spectrum of the extended GCs is collapsed to one dimension. The long exposures of the spectra are affected by numerous cosmic-rays. We found the most efficient way to remove them was to apply the `lacosmic_spec` cosmic-ray removing task (van Dokkum, 2001) on the single exposures. Each GC was observed three times. Since the single exposures did not start at exactly the same pointings, we did not coadd the single frames at this point of the reduction.

For further reduction, the two-dimensional wavelength calibration was calculated using the arc exposures. A fifth-order polynomial fit was sufficient for a residual-free wavelength calibration with a scatter of 0.2 \AA , which is expected at the given spectral resolution. Since the spectra observed with CAFOS show distortion, we used traces of outstanding bright star observations in M 3 to calculate the spatial rectification function. A third order polynomial was sufficient here to compensate for any distortion effects. Using both the wavelength calibration and the distortion correction, the observed spectra were rectified and calibrated. From the full CCD frames we cut out the spectrum of the clusters and used a nearby blank region to estimate the sky background. The regions selected for the cluster and sky spectra along the slit are marked in Fig. 4.2. The two-dimensional spectra of the clusters and the sky were collapsed to one-dimensional spectra. The normalized sky was subtracted from the cluster spectrum. Almost no residual sky was visible in the resulting spectra. As each

¹Based on observations in the framework of the ‘‘Calar Alto Key Project for SDSS Follow-up Observations’’ (Grebel 2001) obtained at the German-Spanish Astronomical Centre, Calar Alto Observatory, operated by the Max Planck Institute for Astronomy, Heidelberg jointly with the Spanish National Commission for Astronomy.

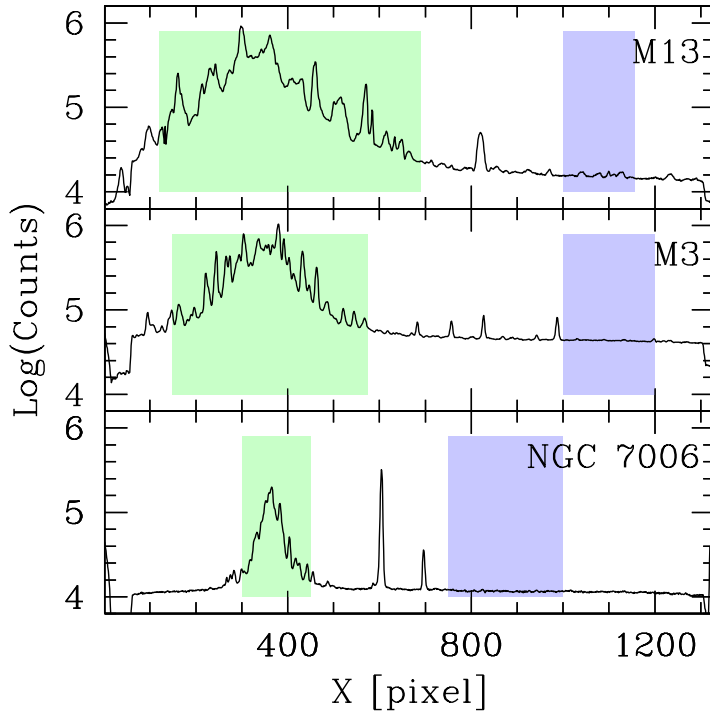


Figure 4.2 : Luminosity distribution of the observed globular clusters along the longslit. The central concentration of the globular cluster light at the $X=350$ pixel stands out. Regions used to determine the spectra of the clusters and the sky are shaded with green and blue, respectively.

cluster was observed three times, the three observations were scaled to the same intensity and averaged to the final GC spectrum. Using the Ca H+K, H_δ , H_γ , and H_β lines, the radial velocities of the GCs were determined, and the resulting Doppler shift was revoked to get rest-frame spectra. The resulting spectra are plotted in Fig. 4.3, where the intensities of the three spectra are scaled to be the same. For comparison, a typical sky spectrum (scaled to the same relative intensity as the GC spectra) is drawn in the same plot.

4.3 Results

The spectra of M 3, M 13, and NGC 7006 in Fig. 4.3 are remarkably similar. The spectrum of M 3 shows a slight deviation in the continuum level compared to M13 and NGC 7006. We assume that changing configurations of the spectrograph during the service mode observations might have caused this difference.

Spectral indices

We quantify the strength of the hydrogen absorption lines and the CH molecule absorption band with spectral indices. The H_β and the H_δ lines are quantified by the original Lick-index bandpass definitions (Worthey et al., 1994); for the H_γ -index we use the Lick passband defined to measure the flux within the hydrogen absorption line, but we use the same regions to measure the continuum level as we use for the CH index. The CH-index is defined as a logarithmic index, while the hydrogen lines are measured as equivalent widths: $EW(H_x) = \int_{\lambda_1}^{\lambda_2} (F_{\text{continuum}} - F_\lambda) d\lambda$. We actually calculated the equivalent widths of the Balmer lines more

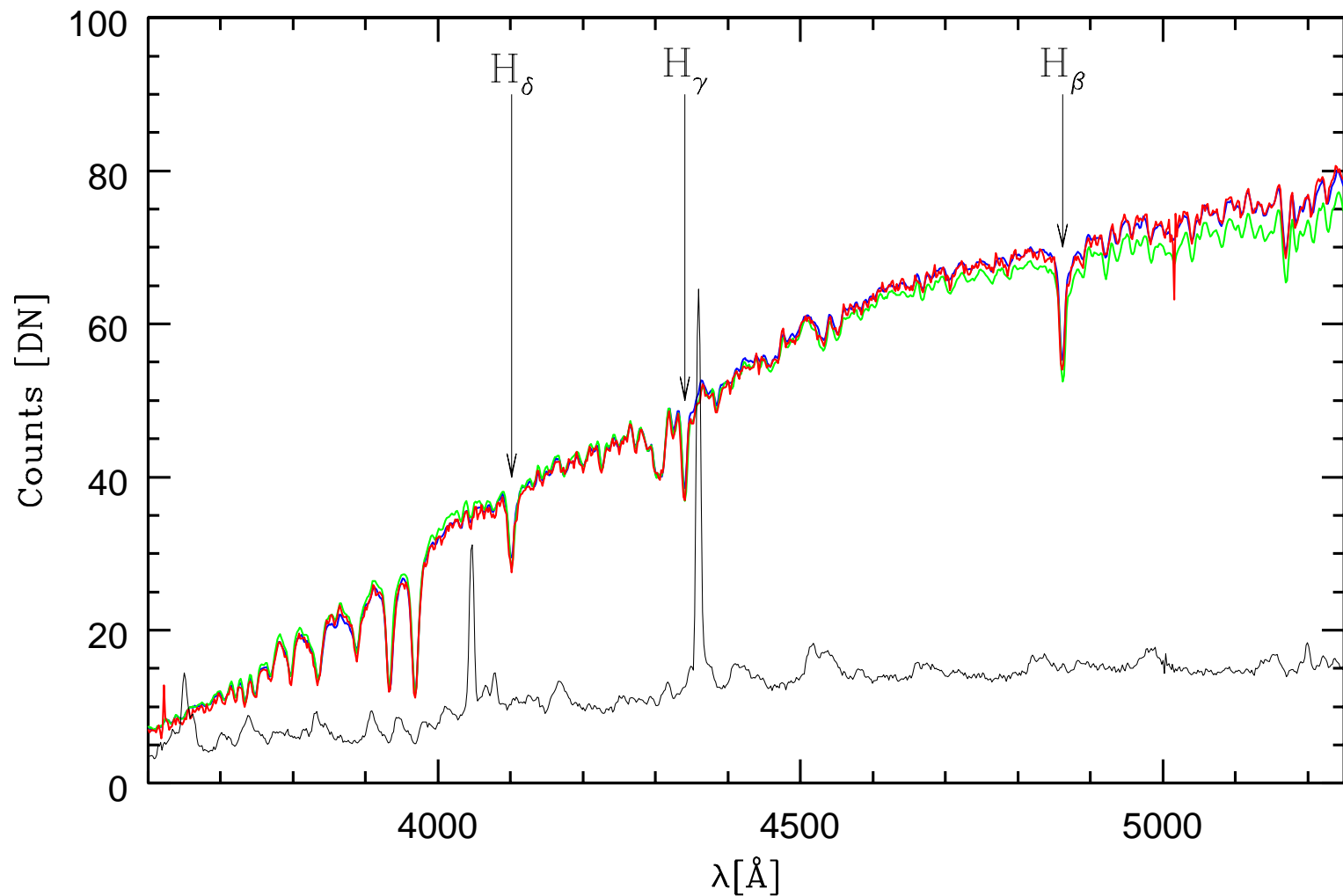


Figure 4.3 : -Integrated drift-scan spectra of the globular clusters M13 (blue), M3 (green), and NGC 7006 (red). The typically subtracted sky level is plotted with a black line. Note the similarity of the spectral energy distributions of these three clusters with metallicities of $[Fe/H] \sim -1.6$ dex. The three clusters cover a large range of HB morphologies.

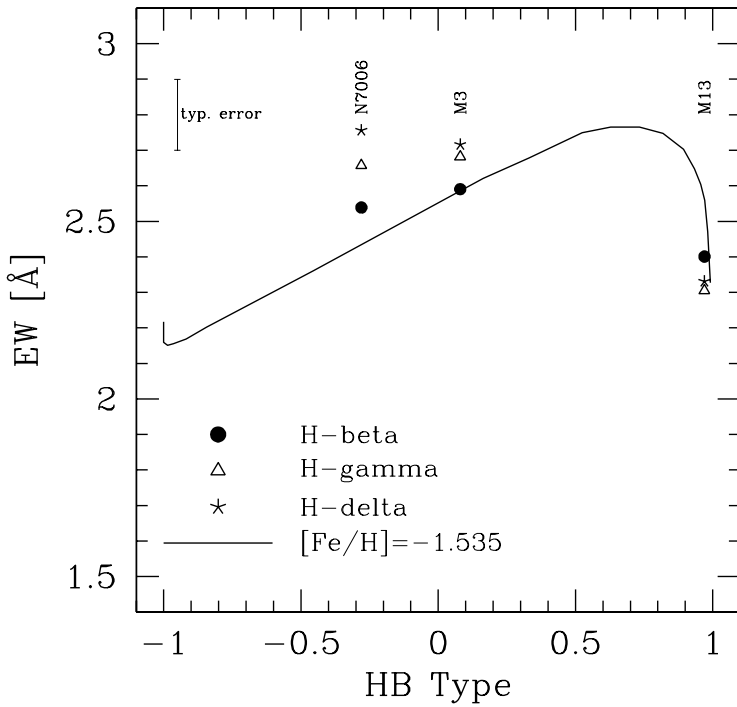


Figure 4.4 : Equivalent widths of the H_β , H_γ , and H_δ lines of M13, M3, and NGC 7006 are plotted versus the HB type of these clusters. The thick line is the fiducial for $[Fe/H]=-1.535$ dex from Lee, Yoon, & Lee (2000); also compare to Fig. 4.1. Note the systematic difference in the Balmer absorption strengths between M13 on the one hand, and M3 and NGC 7006 on the other hand. M13 is the GC with the bluest HB morphology in this sample.

conveniently by determining the flux within the line feature and in two nearby continuum sections:

$$EW = (\lambda_1 - \lambda_2) - F(\lambda_1 - \lambda_2) / (0.5 \cdot C(1) + 0.5 \cdot C(2)), \quad (4.1)$$

where λ_1 and λ_2 denote the lower and upper boundary of the absorption line, while $F(\lambda_1 - \lambda_2)$ is the integrated flux within the absorption line. $C(\lambda_1 - \lambda_2)$ is the normalized continuum level estimated in the region from λ_1 to λ_2 . The indices we use here are hence defined as:

$$EW(H_\beta) = 28.75 - \frac{2 \cdot F(4848 - 4977)}{C(4827 - 4847) + C(4877 - 4892)} \quad (4.2)$$

$$EW(H_\gamma) = 21 - \frac{2 \cdot F(4331 - 4352)}{C(4240 - 4280) + C(4390 - 4460)} \quad (4.3)$$

$$EW(H_\delta) = 21.25 - \frac{2 \cdot F(4091 - 4112)}{C(4057 - 4089) + C(4115 - 4137)} \quad (4.4)$$

$$CH(4300) = -2.5 \log \frac{F_{4285-4315}}{F_{4240-4280} + F_{4390-4460}} \quad (4.5)$$

The derived equivalent widths of the hydrogen lines and the CH index strengths are listed in Table 4.2. We are not able to quantify the integrated CN 3883 Å absorption strength for the GCs since this absorption is hidden in strong Balmer lines. We are lacking sufficient calibrations to transform our measured equivalent widths into the Lick reference system. We therefore use the equivalent width of M 13 derived by Cohen, Blakeslee, & Ryzhov (1998) as reference and add an offset of $\Delta EW = 0.21$ Å to the $EW(H_\beta)$ of the GCs for calibration. There are no EW measurements of the higher Balmer lines available in the literature for the

Table 4.2 : L

Star cluster	CH	EW(H_β) [\AA]	EW(H_γ)[\AA]	EW(H_δ)[\AA]
M 13	0.928 ± 0.007	2.40	2.30	2.31
M 3	0.924 ± 0.007	2.59	2.68	2.68
N 7006	0.923 ± 0.03	2.54	2.66	2.66

GCS observed here. We therefore decided to add the same offset determined for the H_β line to these EWs. Only relative differences will be meaningful in the H_γ and H_δ EWs. Assuming Poisson statistics for the integrated flux, we derive a typical error for the equivalent widths of $\sigma(\text{EW}) \sim 0.1 \text{ \AA}$.

Differences in the Balmer lines

In Fig. 4.4 we plot the derived hydrogen equivalent widths versus the HB morphology of the three GCS and compare the result with the fiducial from Lee, Yoon, & Lee (2000).

Within the error bars, the widths of the H_β Balmer lines in NGC 7006 and M 3 are indistinguishable, but M 13 as the GC with the bluest HB morphology, has significantly lower H_β absorption strengths. The prediction of the Lee, Yoon, & Lee (2000)-model is for these three star clusters. The H_β line strength of NGC 7006 appears to be slightly higher than predicted by the model, but we should note here that NGC 7006 is a bit metal-poorer than M 3 and M 13. The differences in the Balmer line strengths between M 3 and NGC 7006 on the one hand, and M 13 on the other, appear to be more pronounced in the H_γ and H_δ lines. Model calculations for these Balmer lines are not yet available in the literature, but in preparation (priv. comm. Lee). We will be able to check these models in the future with our observations.

Similarity in the CH absorption

The integrated CH(4300)-band absorption strengths of all three observed clusters is — within the observational error — the same (see Table 4.2). Whatever is causing the CNO abundance spreads in GCS, the effect summarized over all stars turns out to be the same. This might indicate that the mechanism behind the abundance spreads in these three clusters is also the same. The fact that there is no strong difference in the integrated CH absorption from cluster to cluster is not directly expected, since the three clusters have different number ratios of CN-strong to CN-rich stars ($\sim 3 : 1$ in M 13, and $\sim 1 : 2$ in M 3, compare with Table 2.3).

4.4 Conclusion

We have compared absorption strengths for the H_γ and H_δ Balmer lines and the CH 4300 \AA G-band of the three metal-poor GCS M 3, M 13 and NGC 7006. The observed H_β line

strengths are in good agreement with models of Lee, Yoon, & Lee (2000). The dependence of the Balmer absorption strengths on the HB morphology appears to be even stronger in the higher Balmer lines.

The problem of the age-metallicity degeneracy in *mixed* stellar populations as investigated by Maraston & Thomas (2000) cannot be solved by the use of higher Balmer lines as age indicators. For the study of the integrated light of unresolved GCs care has to be taken if the higher Balmer lines are used since they have an increased sensitivity to the horizontal branch morphology. In the scenario of Lee, Yoon, & Lee (2000) the variation of the HB morphology is directly linked to the age of a stellar population. If age can be confirmed as the only second parameter of HB morphology in GCs, the increased sensitivity of the higher Balmer lines to HB morphology could improve age estimates of distant GCs based on Balmer line strengths.

The homogeneity of the integrated CH absorption strength among the three clusters suggests that chemical inhomogeneities in CNO elements in an old stellar population might not affect its integrated CH properties. The scatter of CH band absorption in samples of elliptical galaxies (e.g., as discussed in Wirth 1985) would then represent a true scatter in the metallicities rather than a chemical inhomogeneity caused by strange effects of stellar evolution. However, the homogeneity in the CH band absorption does not prove the homogeneity in the integrated CN absorption; a similar study of the integrated CN absorption of metal-rich GCs (with more prominent CN bands) appears appropriate.

Chapter 5

A Wide Field Photometric Study of the Sextans Dwarf Spheroidal

Globular Clusters provide clues about the properties of old, single-age, single-metallicity stellar populations. With a good understanding of these simple stellar populations, we can start to investigate more complex systems. The dwarf spheroidal galaxies of the Local Group are the simplest galaxies known. Investigations of these satellites — they are supposed to be the unmerged remnants of dark matter halos in CDM simulations — can provide us information on their mode of formation and evolution. All Milky Way companions but the Sextans dSph are investigated by deep and wide-field photometric studies. In this chapter, we investigate the photometric properties of the resolved stellar populations in the Sextans dSph.

Abstract

We present wide field photometry reaching the main sequence of the Local Group dwarf spheroidal galaxy Sextans in the Washington photometric system. With a field coverage of 0.5° we are able to investigate the extended distribution in the stellar content of this galaxy. We detect a radial gradient in the horizontal branch (HB) morphology such that in the outer regions bluer HB stars dominate. From the distribution of red giant branch stars we conclude that there could be a radial gradient in the metallicity, too.

5.1 Introduction

Dwarf spheroidal (dSph) galaxies are the least massive, least luminous galaxies known and populate the faint end of the galaxy luminosity function. They are mostly close companions of more massive galaxies, as for example the Milky Way or the Andromeda galaxy in the Local Group (LG). They have low stellar densities and are mostly dominated by old and intermediate-age populations. Here we call a stellar population “old” if it is forming horizontal branch stars (i.e., older than 10 Gyr); stellar populations forming a red clump instead of a horizontal branch are referred to as “intermediate old”. While they are gas-deficient

in the present epoch, they experienced extended or multiple episodes of star formation in the past. In spite of their low mass, the dSph satellite galaxies of the Milky way exhibit an amazing diversity of star formation histories, e.g., Grebel (1997); Mateo (1998).

Table 5.1 : M S

[Fe/H]	Method	Reference
-1.5	photometric	Mateo et al. 1991
-1.7	Ca II triplet	Da Costa et al. 1991
-2.05	Ca II triplet	Suntzeff et al. (1993b)
-1.6	RR Lyrae stars	Mateo et al. 1995

The Sextans dSph galaxy, a faint Milky Way companion with an absolute magnitude of $M_V = -9.5$ mag was discovered only in 1990 (Irwin et al., 1990). Since its discovery, a variety of papers on the stellar content of the Sextans dSph were published (Mateo et al., 1991; Da Costa et al., 1991; Suntzeff et al., 1993b; Mateo, Fischer & Krzeminiski, 1995). These studies found Sextans to be nearby ($(m - M)_0 \sim 19.7$ mag), to have low reddening ($E(B - V) \sim 0.03$ mag), and a low metallicity. The stellar content of Sextans is dominated by old populations (i.e., a prominent horizontal branch is formed). The metallicity determinations for Sextans based on different methods in earlier papers are summarized in Tab. 5.1. The horizontal branch has a quite a red morphology for its low metallicity. The photometric work of Mateo et al. (1991) and Mateo, Fischer & Krzeminiski (1995) yielded a mean metallicity in order of $[Fe/H] = -1.5$ dex to -1.6 dex, which led to the suggestion that Sextans might be too metal-rich to follow the luminosity-metallicity relation for LG dwarf galaxies (see Fig. 5.1). Spectroscopic metallicity determinations by Da Costa et al. (1991); Suntzeff et al. (1993b) based on the Ca triplet pushed Sextans to lower mean metallicity with a large spread (-1.7 dex $> [Fe/H] > -2.25$ dex). With a metallicity in this range, Sextans obeys the luminosity-metallicity relation. The photometrically derived metallicities of earlier studies tend to be higher than the spectroscopic ones.

Sextans has the lowest central stellar density of all known Milky Way companions, distributed on a large area on the sky (its tidal radius is 160', Irwin & Hatzidimitriou 1995). From the dynamical mass based on the velocity dispersion of 21 red giants (assuming virial equilibrium) in Sextans and the baryonic mass seen in stars, Hargreaves et al. (1994) derived a very high mass to light ratio $M/L \sim 121$, indicating a very high dark matter content of this dwarf galaxy. Suntzeff et al. (1993b) found a smaller value of $M/L \sim 54$ or $M/L \sim 30$ based on the measurement of 33 giants, but those calculations depend on the assumed structural parameters of Sextans. The intrinsic uncertainties of the M/L ratios are of order of $\pm 70\%$.

Previous photometric studies cover only a small central part of the extended Sextans galaxy or are limited in depth. The deepest color-magnitude diagram obtained to date reaches barely the main-sequence turnoff region of the old population (Mateo et al., 1991). While all other Milky Way dSph companions have been studied in great detail, the star formation history of

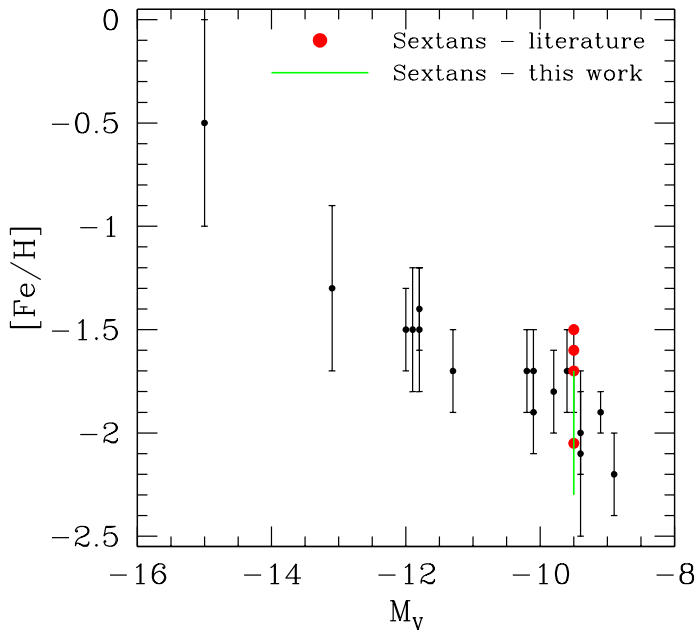


Figure 5.1 : Luminosity-metallicity diagram of Local Group dwarf spheroidal galaxies (data taken from Grebel, Gallagher, & Harbeck 2003). Measurements of the metallicity available in the literature (compare to Table 5.1) are plotted with red points. Early photometric studies measured a metallicity that was too large to strictly obey the general metallicity-luminosity relation. The range of metallicities obtained in this work is indicated by a green bar.

Sextans is still unknown as are details of its stellar content. We present here results from a deep, wide-field study of Sextans.

5.2 Observations and Reduction

We obtained images of Sextans with the Mosaic 2 camera at the CTIO 4 m telescope during an observing run from February 29th 2000 to March 2nd 2000. Observers at the telescope were E. K. Grebel and D. Geisler.

The Mosaic 2 camera is a wide-field CCD camera, consisting of a mosaic of 8 CCD chips with each 4096×2048 pixels. The total field of view is $35' \times 35'$, with small gaps between the chips. Sextans was observed in the broad Washington C and M filters, and in the Johnson R filter as an efficient replacement of the Washington T_1 filter (Geisler, 1996). In addition the narrow band DDO 51 filter was used for observations. The Washington photometric system was chosen for its outstanding sensitivity to metallicity of red giant branch stars (Geisler & Sarajedini, 1999). The narrow band DDO 51 filter is centered on the surface gravity sensitive magnesium Mgb and MgH lines. Combined with the Washington M filter for continuum information it provides the possibility to distinguish between red giants in Sextans and Galactic foreground dwarf stars (Geisler, 1984; Paltoglou & Bell, 1994).

We observed four overlapping fields of Sextans (referred to as pointings A, B, C, and D, see Tab. 5.2). In order to obtain photometries for both the very brightest and the faintest stars in Sextans, we obtained images with two different exposure times per filter. The pattern of the fields A to D was chosen to observe each (faint) star at least three times on at least two different chips of the mosaic of eight CCDs. In the central regions of Sextans each star was observed up to six times on four different CCD chips, thus providing high S/N photometry in the center. The complete set of dithered images covers a field of about 0.5×0.5 degrees². The

Table 5.2 : O

Pointing	RA ^a	DEC ^a	C	R	M	DDO 51	DATE-OBS
A	10 13 43	-01 27 23	1 × 230s	1 × 80s	1 × 30s	1 × 80s	2000/Feb/29
			2 × 2300s	2 × 800s	2 × 300s	2 × 800s	2000/Mar/01
B	10 12 26	-01 46 50	1 × 230s	1 × 80s	1 × 30s	1 × 80s	2000/Mar/01
			2 × 2300s	2 × 800s	2 × 300s	2 × 800s	2000/Mar/02
C	10 13 43	-01 37 24	1 × 230s	1 × 80s	1 × 30s	1 × 80s	2000/Mar/02
			2 × 2300s	2 × 800s	1 × 300s	1 × 800s	
D	10 12 26	-01 47 18	1 × 230s	1 × 80s	1 × 30s	1 × 80s	2000/Mar/02
			1 × 2300s	1 × 800s	1 × 300s	1 × 800s	

Note – ^aRA and DEC are given in h ' ' and ° ' ', respectively. Epoche is J2000.0

pointings and their exposure times are summarized in Tab. 5.2. The footprint of the covered area is shown in Fig. 6.2. The seeing conditions during the observations ranged from 0.8'' to 1.4'' on the images with a median value of 1''. Unfortunately, no comparison fields in the vicinity of Sextans were observed. Since Sextans is located at a modest distance from the galactic plane ($l = 243.47^\circ$, $b = +42.27^\circ$), field star contamination is an issue. It will turn out later on that the lack of a comparison field is a major constraint for this work.

The basic CCD reduction of the images was done by J. Holtzman using the VISTA software package. This basic reduction on a chip-by-chip basis included overscan subtraction, BIAS correction and flat fielding. The images were corrected for the non-uniform pixel scale of the Mosaic-2 instrument. Such a correction is necessary for wide field imaging cameras because the flat field correction already over-corrects for the variations in the pixel scale: after the flat-field correction is applied, the sky background appears flat. But since the number of photons within a point spread function (PSF) of a single star is constant irrespective of pixel scale, point source photometry would suffer from a non-constant photometric zeropoint over the field of view. Therefore the correction for the pixel-scale has to be revoked, leading to correct measurements of stellar luminosities, at the costs of a non-uniform background. Since local sky-subtraction will be enabled in the later photometry, the non-uniformity of the sky background will not affect the resulting photometry.

For the following photometric reduction we choose the *daophot* implementation in IRAF¹. Each chip of the mosaic was reduced separately because we found that the point-spread function (PSF) of the stars exhibits strong variations over the full field of view that can not be handled by *daophot* correctly even with a second order variable PSF. Aperture and PSF photometry was done for all observed fields and all filters. The intensity scale between the aperture and PSF photometry is not necessarily the same for all images since the result of the PSF photometry depends on the chosen reference stars to build the PSF model. The difference between aperture photometry and PSF photometry was determined using ~ 20 isolated and unsaturated bright stars. The typical uncertainty of this shift is of order of 0.02 mag. All photometries of chip #1 had a systematically higher deviation from the other chips, which

¹see Acknowledgments.

Table 5.3 : P

Filter	DATE-OBS	k	z	c	\bar{c}
C	2000/Feb/29	-0.210± 0.02	-3.401± 0.03	0.091 ± 0.005	0.082
	2000/Mar/02	-0.203± 0.03	-3.391± 0.04	0.084 ± 0.006	
	2000/Mar/01	-0.275± 0.03	-3.270± 0.04	0.072 ± 0.007	
T ₁	2000/Feb/29	-0.014± 0.02	-2.474± 0.03	0.020± 0.004	0.0215
	2000/Mar/02	-0.079± 0.02	-2.378± 0.02	0.021± 0.003	
	2000/Mar/01	-0.004± 0.02	-2.485± 0.03	0.023± 0.003	

may be caused by an extremely low full-well capacity of this chip (R. Schommer, priv. comm.). We exclude this chip from our further analysis; this explains the strange footprint of the observations in Fig. 6.2. We applied additional selection criteria for the photometries using the daophot sharpness and chi parameters: $|\text{sharpness}| \leq 0.25$ and $0.5 \leq \text{chi} \leq 1.5$. This selection rejects extended objects such as galaxies or saturated stars as well as photometry affected by blooming and cosmic ray hits. Using the USNO-A 2.0 catalog (Monet et al., 1996), we re-determined the astrometric calibration for all images on a chip-by-chip basis. The positions of all stars on the single chips were transformed to J2000 equatorial coordinates.

5.2.1 Calibration

In addition to the observed Sextans fields, standard stars for the C, T₁ filters (Geisler, 1996) were observed four times per night. The nights turned out to be photometric with the following calibration solutions:

$$\begin{aligned}
 C &= c \\
 &+ k_c \cdot X + c_c \cdot (C - T_1) + z_c \\
 T_1 &= r \\
 &+ k_{T_1} \cdot X + c_{T_1} \cdot (C - T_1) + z_{T_1}
 \end{aligned}
 \tag{5.1}$$

$$\tag{5.2}$$

Capital letters in these equations represent standard magnitudes, while lower case letters are instrumental magnitudes. X is the mean airmass during the observation, k_N is the airmass coefficient for the filter N , c_N the color term and z_N the zero point. The coefficients for all three nights were determined are listed in Tab. 5.3 (Jon Holtzman, priv. comm). Note that the Johnson R filter was used as a replacement of the Washington T₁ filter, and we use photometric standard stars of the Washington system. In the following we will refer to R observations as T₁ photometry. Because the color term is mainly determined by the wavelength

dependence of the instrumental transmission we construct the average color coefficient for each filter from the three nights, which is listed as $\overline{c_N}$ in Tab. 5.3.

The photometric corrections for airmass, zero points, and the shifts between aperture and PSF magnitudes were applied to all measured magnitudes. Unfortunately, no standard star observations for the DDO 51 and Washington M filter were available. Lacking a proper calibration relation, we used the extinction coefficients of the Washington C filter. Since the DDO 51 and Washington M filter have similar central wavelengths, this approach will not disturb relative differences between the M and DDO 51 photometries. Nevertheless, no absolute calibration for these filters will be feasible. The photometries of all stellar objects, that were observed several times in the same filter, were matched, and their fluxes were averaged. The star matching criterion was that a star's position in other pointings must not deviate by more than 1". Since almost always more than one measurement per star was available, we calculated the final photometric error (σ) assuming error propagation of the uncertainties of the individual measurements as they are given by daophot's *magerr* parameter. Additionally, the standard deviation of the different photometric measurements (δ) was calculated. Finally, the photometries of all filters were matched and the final photometry database was constructed. The correction for the color term in equation 5.1 was applied to the final photometry.

5.2.2 Reddening

Several determinations of the reddening towards Sextans can be found in the literature. E.g., Mateo, Fischer & Krzemiński (1995) estimated a reddening towards Sextans of $E(B - V) = 0.037$ from the location of the red edge of the BHB in the color-magnitude diagram. We prefer to use an estimation of the reddening that is independent from the analyzed object itself. In the extinction maps of Schlegel, Finkbeiner, & Davis (1997) the reddening towards the central position of Sextans is determined to $E(B - V) = 0.045$. In these maps, however, the reddening varies between 0.02 and 0.06 mag in one degree around Sextans' center. We adopt the slightly higher reddening correction of $E(B - V) = 0.045$ from the Schlegel, Finkbeiner, & Davis (1997) maps rather than the value determined by Mateo, Fischer & Krzemiński (1995). Note that the Mateo, Fischer & Krzemiński (1995) value is well within the range of extinction scatter in the vicinity of Sextans.

The star's colors and magnitudes were now dereddened using the relations by Geisler Clariá & Minniti (1991) with

$$\begin{aligned} (C - T_1) &= (C - T_1)_{red} - 1.97 \cdot E(B - V) \\ (T_1 - I) &= (T_1 - I)_{red} - 0.69 \cdot E(B - V) \\ T_1 &= T_{1red} - 2.62 \cdot E(B - V) \end{aligned} \tag{5.3}$$

The variations in the reddening $E(B - V)$ of ± 0.02 dex towards Sextans translates into a scatter of ± 0.04 in $C - T_1$ and ± 0.05 in T_1 .

Later in this chapter we will determine the distance modulus of Sextans. To correct for reddening of the determined distance modulus we will use the relation $(T_1 - t_1) = (M - m) - 0.54 \cdot E(B - V)$ (Geisler & Sarajedini, 1999).

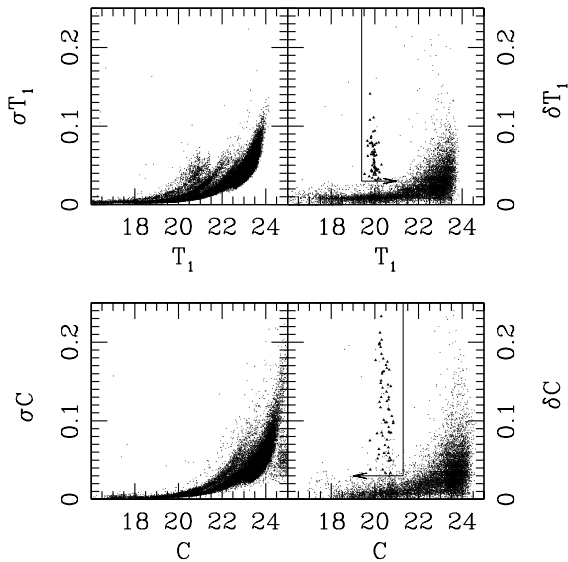


Figure 5.2 : *Left: The photometric error of the combined photometry: On the left we show the photometric error σ of the T_1 and C photometry depending on the star's magnitude. Right: The true scatter of multiple photometries of the stars (Eqn. 4.3, see text). Both error estimates are in good agreement. Only stars at $C \sim 21$ mag and $T_1 \sim 20$ mag show a significantly enhanced scatter and can easily be identified as RR Lyrae variables in the CMD. The line and arrows on the right side select RR Lyrae candidates.*

5.2.3 Photometric errors and Incompleteness

In Fig. 5.2 we show the resulting error of the photometry. On the left side the theoretical propagated error of the individual photometries is shown. One can clearly see different error paths, depending on how many photometries were actually combined. On the right side of this figure we show the real scatter δ of the combined photometries, calculated as

$$\delta = \sqrt{\frac{\sum_{i=1}^n (m_i - \bar{m})^2}{n}} \quad (5.4)$$

were m_i is photometry of a star detected on a single frame, \bar{m} the averaged magnitudes of all photometries of a star, and n is the number of photometries. One can clearly see that the real scatter is similar to the theoretical prediction, except for some stars in the region around $C = 20$ mag and $T_1 = 20$ mag. Stars exhibiting large scatter in this region can easily be identified as RR Lyrae stars (see also Stetson, Harris, & Smecker-Hane 1997).

In order to estimate the completeness of our photometry (i.e., the fraction of stars in the observed fields that are indeed identified by our photometric pipeline), we made an artificial star experiment for one representative, long exposure obtained in the C and in T_1 filters. Based on the PSF modelled during the photometry, artificial stars of a given magnitude were calculated and added to the images with the IRAF `addstar` task. In magnitude steps of 0.25 mag we typically added 10 000 stars per luminosity. The stars were distributed on a spatial grid with a grid-size of 20.14 pixels. Since the stars are not placed in the images randomly, the large amount of added stars per run will not introduce additional crowding effects as two artificial stars will not overlap! With the artificial stars added, we re-run the reduction pipeline on the images in the same way we obtained the original photometry. The number of artificial stars that are found by the photometric rerun measures the incompleteness for the given magnitude. We will refer to this incompleteness estimation later on.

While for single frame observations our model calculations are a good measure for the incompleteness, the matched photometries of multiple observations are more difficult: Due to improper star matching some stars might appear twice in the database. This would introduce an undetermined incompleteness, or better, over-completeness, in the photometry. For a complete description of the incompleteness effects in this matched photometries, artificial star experiments would have to be done for all observed frames and must be passed through the whole matching and calibration process. Since the photometric pipeline itself for all frames runs already requires two weeks computing time, a whole set of artificial star experiments is out of reach in a reasonable amount of time.

For a qualitative description of the color-magnitude diagram of Sextans we will use the combined photometries with an uncertain incompleteness. Later in this chapter we will investigate spatial distributions of sub-populations in Sextans. Since reliable star-counts are essential here we constructed a second photometric database, which uses only one exposure per filter and field on the sky. For this dataset the photometric error is of course larger than in the full, combined dataset, but it will not be affected by subtle incompleteness effects.

5.3 Color-Magnitude Diagram

The CMD of Sextans is plotted in Fig. 5.3. We use the full dataset, i.e., the averaged photometries. Prominent features are evident in the CMD: (i) the red giant branch (RGB), (ii) the blue and red horizontal branch, with a well-populated region of RR Lyrae stars in between, (iii) an old main-sequence turn-off (MSTO), and (iv) an extension of the main sequence. The extension from the MSTO region can be interpreted either as an intermediate old stellar population or as a prominent population of blue straggler stars. The width of the sub-giant branch is comparable with the photometric uncertainty. In this CMD the upper part of the RGB does not stand out due to the strong background contamination.

In section 5.2.2 we noted that the range of reddening towards Sextans would cause a scatter of ± 0.04 and ± 0.05 in $(C - T_1)$ and T_1 , respectively. In this plot, all stars over the large field of view are dereddened with the same reddening. In an experiment we dereddened all stars with individual values of $E(B-V)$ as they are proposed by Schlegel, Finkbeiner, & Davis (1997). We couldn't find evidence for an improvement in the photometry as it would be indicated by a narrower RGB; we therefore proceed here with one common dereddening vector for all stars in our sample.

There are only very few evolutionary models publicly available that were transformed into Washington colors. Experiments with different models showed that none of them perfectly fit the turn-off region and the RGB of Sextans at the same time. Nevertheless, we overplot in Fig. 5.3 isochrones from Lejeune & Schaerer (2001) to the CMD. The metallicity of $[Fe/H] = -1.67$ dex was chosen since this is the most metal-poor isochrone available; the two isochrones assume ages of 10 Gyr and 2.2 Gyr. As already mentioned by Mateo, Fischer & Krzemiński (1995), it is very suggestive that Sextans contains a minor intermediate old stellar population, although the dominant fraction of stars in Sextans is as old as 10 Gyr, or even older.

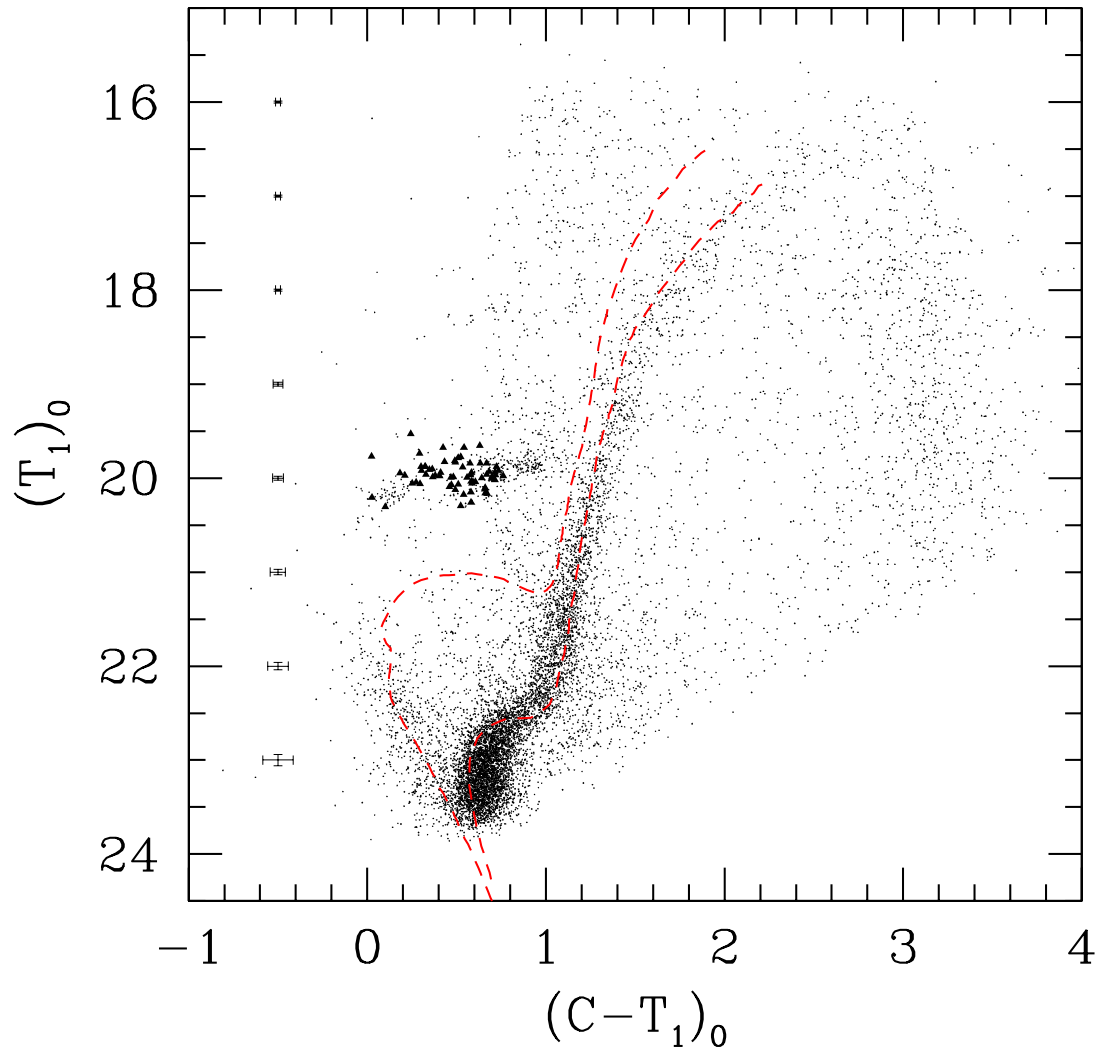


Figure 5.3 : Color-magnitude diagram of the full Sextans field. The RR Lyrae stars as identified in Fig.5.2 are marked as triangles. Lejeune & Schaerer (2001) isochrones for $[Fe/H] = -1.67$ dex and ages of 10 Gyr and 2.24 Gyr are drawn with red lines.

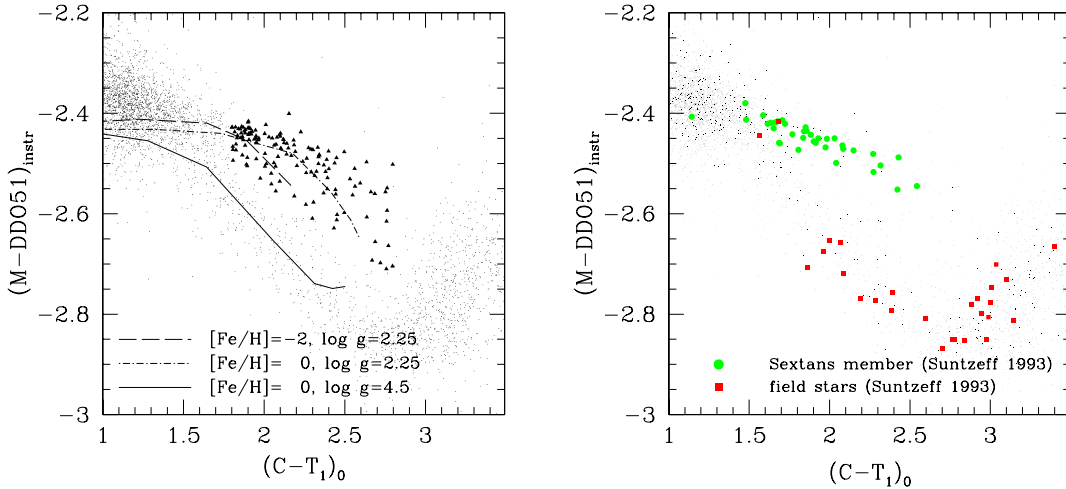


Figure 5.4 : *Separating Sextans giant stars from foreground field dwarfs: The M-DDO 51 index is dependent on the surface gravity for K stars. On the left side we show M-DDO 51 vs. the $C-T_1$ color. One can clearly see how the Sextans giant population separates in the upper branch from the field. The lines are model fiducials from Paltoglou & Bell (1994). In the color range $1.8 \text{ mag} \leq (C-T_1) \leq 2.8 \text{ mag}$ we selected the giant stars (marked with triangles). On the right plot we mark stars with known membership (from radial velocity, Suntzeff et al. 1993b) with green circles. Stars that are not members of Sextans are represented by red squares. Note the clear separation between these two populations.*

5.3.1 Distinguishing between foreground dwarfs and red giants

The narrow-band filter DDO 51 is centered on the Mgb and Mgh bands at 5100\AA . The strength of the absorption features depend on the surface gravity and can therefore be used to distinguish between foreground dwarf stars and red giants (Geisler, 1984; Paltoglou & Bell, 1994; Majewski et al., 2000). With the Washington M filter as continuum filter the color index $(M-DDO 51)$ measures the relative strength of this absorption feature. In Fig. 5.4 (left) we plot the $(M-DDO 51)$ color vs. the $(C-T_1)$ color. In the color range of $1.8 \text{ mag} \leq (C-T_1) \leq 2.8 \text{ mag}$ metal-rich foreground dwarfs and metal-poor giants occupy clearly distinct locations. Theoretical fiducials from Paltoglou & Bell (1994) for giants with $[Fe/H]=0$ dex and -2 dex and $\log g$ of 2.25 as well as dwarf stars with $[Fe/H]=0$ dex and $\log g = 4.5$ are overplotted here. As mentioned in section 5.2.1 there are no flux standard observations in the M and DDO 51 filters available. The M and DDO 51 photometries in this plot are therefore instrumental magnitudes. We applied an offset of -2.45 mag to the M-DDO 51 index of the fiducials to match the data points. We select RGB star candidates from the upper branch of stars in Fig. 5.4; the candidates are marked by triangles. There remains one caveat in this kind of RGB star selection: very metal-poor halo dwarfs will overlap with red giants, (Majewski et al. 2000; Morrison et al. 2000). Also unresolved, distant galaxies can mimic RGB stars.

Suntzeff et al. (1993b) measured radial velocities for ~ 80 stars in Sextans, of which 42 were confirmed as members. We could identify 41 of the confirmed Sextans members and

37 field stars of Suntzeff et al.’s spectroscopic sample in our data. In Fig. 5.4 (right) we mark these stars with circles (members) and squares (non-members). Note that all the spectroscopically confirmed members are located in the upper branch of the two-color diagram, while non-members lie at the expected location of Galactic foreground dwarfs. Thus the use of the DDO 51 filter to distinguish reliably between foreground contaminants and giants in Sextans is convincingly confirmed. Nevertheless, the usable color-range to distinguish between RGB and foreground stars is limited.

5.3.2 Distance modulus

With the help of the DDO 51 filter we are able to identify the Sextans stars at the tip of the RGB. Geisler & Sarajedini (1999) showed that old stellar populations with $[\text{Fe}/\text{H}] \leq -1.15$ dex have a constant T_1 luminosity of $M_{T_1\text{TRGB}} = -3.22 \pm 0.11$ mag at the tip of the RGB. In Fig. 5.5 we plot a blow-up of the tip of the RGB. Star-like objects that are classified as RGB stars according to Fig. 5.4 are plotted with filled circles. At the bright end, the tip of the RGB clearly separates from the background. Nevertheless, for fainter objects (i.e., $T_1 \geq 18.5$ mag), a lot of false identifications of RGB stars show up in the plot. Their number increases with decreasing luminosity. These objects cannot be RGB stars owing to their magnitudes and are most likely unresolved background galaxies (Grebel, Braun, & Burton, 2000).

The cumulative luminosity function for the Sextans’ DDO 51-selected giants is plotted in the upper left corner of Fig. 5.5. We identify the tip luminosity for Sextans at the increase of the luminosity function at $T_1 = 16.45 \pm 0.05$ mag. This results in a distance modulus of $T_1 - t_1 = 19.67 \pm 0.12$ mag. Using equation 5.3, the dereddened distance modulus towards Sextans is $M - m = 19.69 \pm 0.12$ mag. An additional error source for the distance modulus is the uncertainty in the reddening towards Sextans. But the scatter of $E(B - V) = \pm 0.02$ dex would cause an error in the distance modulus of only $\Delta(M - m) = 0.01$ dex and can therefore be neglected. Our distance determination towards Sextans is in excellent agreement with the the distance modulus derived by Mateo, Fischer & Krzeminiski (1995) ($(M - m) = 19.67 \pm 0.15$ mag).

5.3.3 Metallicity from the RGB

The width of Sextans’ tip of the RGB in Fig.5.5 is much larger than expected from the photometric errors and differential reddening effects alone. Since especially at the tip of the RGB the morphology strongly depends on metallicity, a large spread in the metallicity is suggested. Nevertheless, additional parameters like age also influence the morphology of the RGB, introducing a general ambiguity on the nature of the width of the RGB. The location of RGB stars in the CMD is therefore not a unique measure of the stars’ metallicities. For very old stellar populations (older than, e.g., 10 Gyr, see Fig. 6.1), there is no significant influence of age on the width of the RGB.

We overplot giant branches from fiducials for the RGB that were measured from globular clusters with known metallicities (Geisler & Sarajedini, 1999) in Fig. 5.5. We shifted the

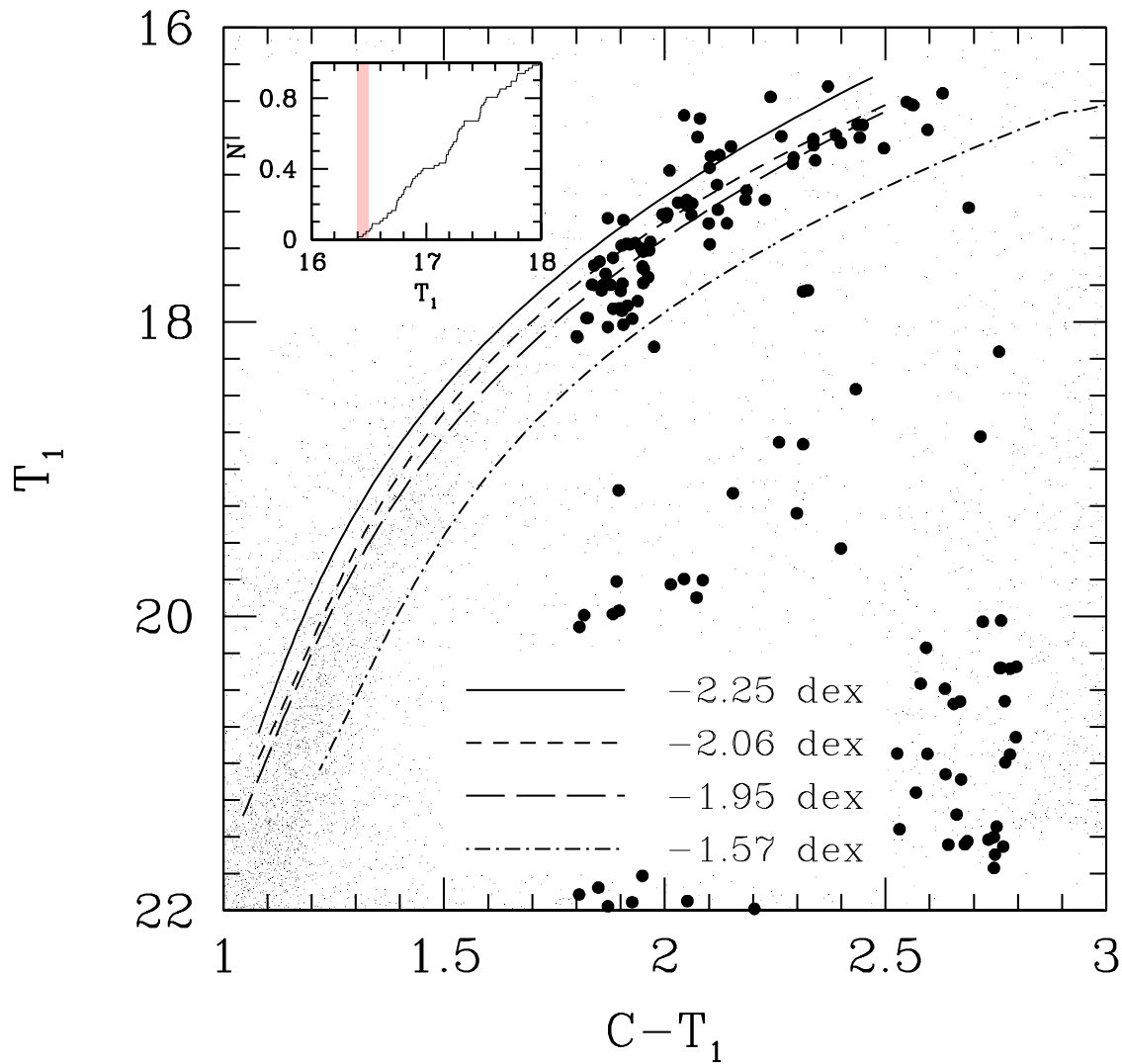


Figure 5.5 : CMD of the RGB. The giant stars identified by the DDO 51 photometry (see Fig. 5.4) are plotted with filled circles. The stars at the tip of the RGB clearly separate from the foreground dwarf stars. Towards fainter magnitudes there is an increasing contamination by unresolved redshifted galaxies that mimic RGB stars in the current selection. We overplot standard giants branches from Geisler & Sarajedini (1999) for metallicities of -2.25 dex, -2.06 dex, -1.95 dex, and -1.57 dex. In the upper left pannel the luminosity function for all DDO 51-selected giant stars at the tip of the RGB is plotted. The tip of the RGB is identified by the upturn in that luminosity function, which is marked by the red bar; the width of the red bar corresponds to the estimated uncertainty of this identification.

fiducials with a distance modulus of 19.7 mag and dereddened them to match the Sextans' data. In this diagram the fiducials of NGC 7078, NGC 4590, NGC 6397, and NGC 5272 with metallicities of $[\text{Fe}/\text{H}] = -2.25$ dex, -2.06 dex, -1.95 dex, and -1.57 dex, respectively, are shown. The metallicities on the Zinn & West scale (Zinn & West, 1994) are taken from Harris (1996). The first three fiducials fit the RGB quite well, while the last one with $[\text{Fe}/\text{H}] \sim -1.57$ dex appears too metal-rich. We conclude that Sextans has a metallicity in the range of approximately $-1.7 \text{ dex} < [\text{Fe}/\text{H}] < -2.3 \text{ dex}$, which is in good agreement with the earlier spectroscopic determinations, but more metal-poor than earlier photometric measurements.

5.3.4 The red bump

The red bump (RB) is a local maximum in the RGB stellar luminosity function. At the luminosity of the RB, the convective envelope of a star hits the hydrogen burning shell and the stellar evolution is slightly slowed down. The absolute luminosity at which the RB occurs depends on the metallicity and age of a stellar population. The RB luminosity relative to the HB luminosity $\Delta T_{1\text{HB}}^{\text{bump}} = T_{1\text{bump}} - T_{1\text{HB}}$ depends on the metallicity only and is therefore a suitable tool to derive metallicities of stellar populations (Fusi Pecci et al., 1990; Sarajedini & Forrester, 1995).

In Fig. 5.6 we select stars from the red giant branch as follows: We parameterize a Lejeune isochrone with $[\text{Fe}/\text{H}] = -1.7$ dex and an age of 12 Gyr by a third order polynomial. The blue and red boundaries of the RGB selection are defined by the mean RGB ridge line that was shifted by ± 0.2 mag in $C-T_1$ to take the intrinsic width of the RGB into account. This parameterization is shifted 0.02 mag bluewards to fit on the center of the RGB. This offset between the parameterization and the RGB is expected due to the fact that we find Sextans to have a mean metallicity of less than -1.7 dex. Only stars within the red and blue boundaries and with $T_1 < 21$ mag and $T_1 > 17$ mag were selected from the RGB.

For the RGB stars we calculate the luminosity function from which we identify an extended RB from $T_1 = 19.2$ mag to $T_1 = 19.7$ mag. To estimate the mean luminosity of the HB we calculate the mean luminosity of all identified RR Lyrae stars. This way we find $T_{1\text{HB}} = 19.99$ mag. The resulting difference of the HB and RB magnitude is therefore in the range $\Delta T_{1\text{HB}}^{\text{bump}} = -0.8$ mag to -0.3 mag.

According to Geisler & Sarajedini (1999) the relative T_1 luminosity of the red bump translates to a metallicity on the Zinn & West scale (Zinn & West, 1994) through the following relations:

$$[\text{Fe}/\text{H}] = -1.139 + 1.23 \times \Delta T_{1\text{HB}}^{\text{bump}} \quad (5.5)$$

The resulting range of metallicities of RGB stars in Sextans calculates to $[\text{Fe}/\text{H}] = -1.5$ dex to $[\text{Fe}/\text{H}] = 2.1$ dex. A major concern here is the strong field star contamination of the RGB at which the RB occurs, and the DDO 51 based identification of RGB stars does not work in this color range. A clear identification of the RB is therefore difficult and the full extent of the RB might be hidden in the noise. Nevertheless we find a good agreement between the estimated range of metallicities from the RGB fiducials in section 5.3.3 and from the RB method.

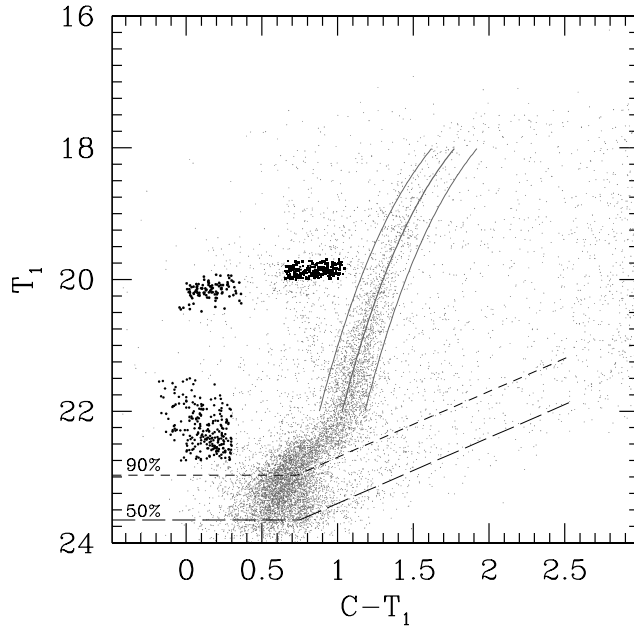


Figure 5.6 : Selection of subpopulations in the CMD: Blue horizontal branch (HB) red HB stars are plotted with squares. Stars in the region of an intermediate main-sequence (or blue straggler candidates) are drawn with hexagons. The center of the RGB is parameterized by a Lejeune isochrone with $[Fe/H]=-1.7$ and 12 Gyr. Limiting lines indicating the red and the blue envelope of the red giant branch were plotted by shifting the central ridge line in color. The dashed lines indicate the 90% and 50% completeness magnitudes.

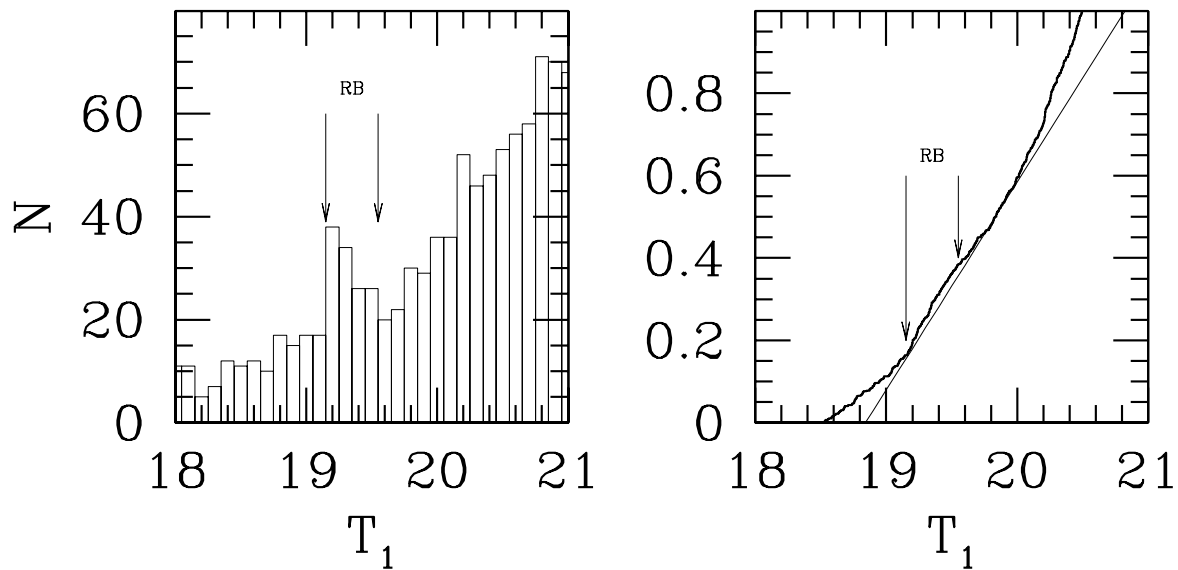


Figure 5.7 : Identification the RGB red bump from the RGB luminosity function. On the left side we show the luminosity function of the RGB (as selected in Figure 5.6). On the right side we present the cumulative luminosity function.

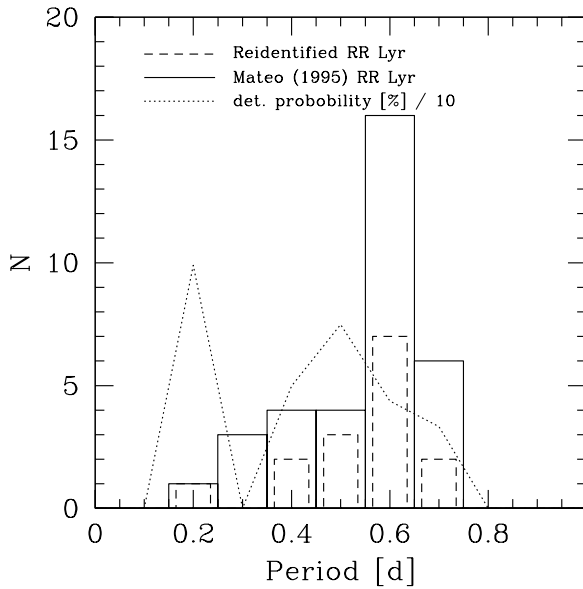


Figure 5.8 : *Detection probability for RR Lyrae stars in our observations depending on the period compared to the identification of variable stars in Mateo, Fischer & Krzeminski (1995).*

5.3.5 RR Lyrae stars in Sextans

Our observations of Sextans are distributed on several single exposures that are distributed over several nights. We are therefore able to detect variable stars with short periods. Variable stars with an amplitude of their light curves larger than the photometric error of the single observations can easily be identified due to their increased scatter of the photometries from different epochs. Our observations are distributed over three nights, allowing us to predominantly detect RR Lyrae stars, on which we will concentrate here. In Fig. 5.2 (right) we already plotted the true scatter of the multiple photometries (defined in formula 5.3) for all stars. Variable stars with sufficiently large luminosity variations within the time period covered by our observations show a significantly enhanced scatter compared to non-variable stars of the same luminosity (where the scatter represents the photometric uncertainty only) and can therefore be easily detected. This detection scheme is similar to the one developed by Welch & Stetson (1993). To detect RR Lyrae stars we require that the stars have to have a scatter in C and T_1 of at least 0.03 mag and lie within the magnitude range $C \leq 21.3$ and $T_1 \geq 19.5$. With this detection criterion we find a total number of 72 RR Lyrae in our sample. These variables are marked by triangles in Fig. 5.3.

Our observations were not optimized to detect variable stars and the detection of RR Lyraes is influenced by a large incompleteness. To quantify this incompleteness we compare our detections with the list of RR Lyrae stars of Mateo, Fischer & Krzeminski (1995). These authors surveyed a $18' \times 18'$ field in Sextans for variable stars through multi-epoch observations and found 38 RR Lyraes. Their central field on the center of Sextans is completely covered by our data. We re-identify 16 of Mateo et al.'s stars. In Fig. 5.8 we show the histogram of the periods for all stars of Mateo, Fischer & Krzeminski (1995) (solid line) and of stars with a re-identification in our sample (dashed line). Our detection probability peaks at a period of 0.5 days (dotted line). The overall detection probability for RR Lyrae stars is

$16/38 = 0.42$. We estimate that the total number of RR Lyrae stars in our Sextans field is $N_{RRLyrae} = 72/0.42 \sim 170$.

The comparison with the study by Mateo et al. (1995) allows us to obtain empirical boundaries of the RR Lyrae instability strip in Washington colors, which in turn helps us to constrain the blue edge of the non-variable red HB and the red edge of the blue HB. We will use this boundary in the next section.

5.4 Radial gradients in post main-sequence populations

Among a variety of galaxy types, population gradients are a common feature. These population gradients are in general reflected by gradients in the colors of galaxies. The integrated colors of the galaxies do not provide the full information on the stellar content, since both age and metallicity affect the integral properties of a galaxy. Without detailed knowledge on the stellar content of a galaxy it is impossible to identify the driver of these gradients. The Local Group of galaxies is the only place in the universe where we can resolve stars outside the Milky Way. In particular the uncrowded environment of dSphs allows us to study population gradients — in this type of galaxy at least — with the help of resolved stellar populations. In a few dSphs with predominantly old stellar populations, the red HB has been found to be more centrally concentrated than the blue HB (e.g., Da Costa et al. 1996; Majewski et al. 1999; Hurley-Keller, Mateo, & Grebel 1999). Such radial gradients in the HB morphology can even be found in some globular clusters (e.g., in NGC 7006; (Buonanno et al., 1991)). In dSphs containing intermediate old and relatively young stellar populations, the younger populations tend to be more centrally concentrated (see Grebel 2000 for a review). So far, no population gradients could be identified in Sextans since photometry over a sufficient large field was missing.

We investigate possible spatial variations in stellar populations in the Sextans galaxy. Since completeness effects might play an important role, we switch to the use of the reduced dataset here (see Section 5.2.3), since it does not contain any incompleteness effects due to failed pair matching. This dataset uses only one deep exposure per filter in contrast to the combined dataset where repeated photometries are averaged. We select stars only well above the cut-off magnitude near $T_1 = 23$ mag (see Fig. 5.6). Since crowding does not play a role at all, even in the center of Sextans, incompleteness effects will not affect our results.

We select blue and red horizontal branch stars from Fig. 5.6. We separate blue and red HB stars at the RR-Lyrae instability strip, excluding the region of the variable stars in this selection. In addition, stars from the RGB are selected according to the selection in this CMD. We distinguish between stars that are redder (RRGB) and bluer (BRGB) than the mean ridge line of the RGB. Finally, stars at the location of an intermediate old main sequence (or possible blue straggler stars) are selected (MSBS).

Fig. 5.9 (left) shows the cumulative radial distributions for all RGB stars (i.e., RRGB and BRGB stars), for all HB stars (i.e. blue and red HB stars, but without variable stars), and for MSBS candidates. For comparison, the distribution of galactic foreground stars with $(C-T_1) \geq 2$ mag and $T_1 \geq 19$ mag is shown. All sub-populations of Sextans show a central

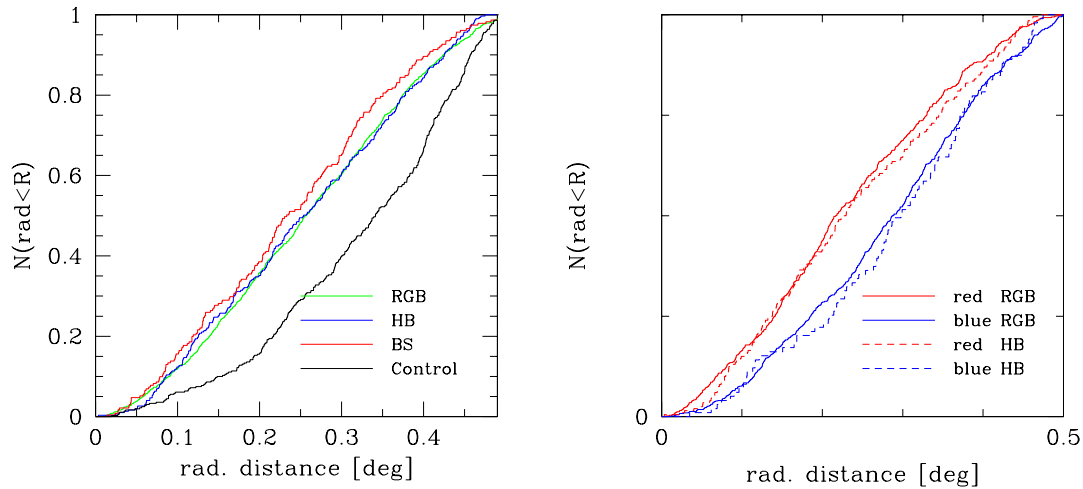


Figure 5.9 : Cumulated radial distributions of different sub-populations in Sextans. The whole RGB, the blue and red HB stars, and the stars at the location of an intermediate old / blue straggler population are plotted. There is no significant difference in their radial distributions. On the right side we distinguish between red and blue HB stars and red and blue RGB stars. Note the central concentration of the red HB and red RGB stars. The selection of stars is the same as in Fig. 5.6

concentration compared to the evenly-distributed field-stars. The HB and the RGB have an indistinguishable radial distribution. The MSBS candidate stars seem to show a slightly stronger central concentration, but their distribution is still nearly indistinguishable from the HB and RGB star distributions. A Kolmogorov-Smirnov (K-S) test gives a probability of 95% that RGB and HB were drawn from the same population. The same test applied to the RGB and MSBS stars gives a probability of $\sim 26\%$. The picture looks completely different if we distinguish between the radial distribution of red and blue HB stars, and between the red and blue RGB stars. Selecting RGB stars either redwards or bluewards of the mean RGB ridge line effectively selects stars that are on average more metal-rich or more metal-poor than the mean population, respectively, providing that age differences can be neglected. For individual stars this selection criterion isn't accurate enough, especially at the lower RGB where the metallicity dependence of the RGB morphology is smaller. Nevertheless, for a large sample of stars such a selection is still meaningful. Fig. 5.9 (right) shows the radial distribution of the so-selected stars: the red HB stars and red RGB stars tend to be more concentrated than the blue ones. We quantify this result with a K-S test. We find a probability of 0.3% that the red and blue HB stars have the same radial distribution. For the red and blue RGB stars the probability decreases to 0.0003%.

We quantify the blueness of the RGB or HB by the number ratio $i = n_{blue} \cdot (n_{red} + n_{blue})^{-1}$, where n_{red} and n_{blue} is the number of red and blue stars. i is calculated for the inner and outer regions of Sextans (radial distance $r = 0 \dots 0.25^\circ$ and $r = 0.25 \dots 0.5^\circ$, respectively). The adequate statistical tool to compare those number ratios is the T_2 -statistic² (Da Costa et al., 1996). When the two number ratios are derived from the same distribution the T_2 value has a

²see also Chapter 6

normal distribution around zero with a width of 1. For the red and blue RGB stars we obtain a T_2 value of 3.8 and for the HB stars $T_2 = 2.9$. Therefore, these distributions are unequal at $\sim 4\sigma$ and 3σ levels, respectively.

In contrast, the probability that the red HB stars and the red RGB stars are drawn from the same distribution is much higher: The K-S test gives 77% for the red stars and 58% for the blue stars. This result may suggest that the metal-poor, less centrally concentrated RGB stars of Sextans would evolve to become blue HB stars. The gradient in the HB and RGB morphology would then represent a gradient in the mean metallicity.

5.5 Blue stragglers vs. young stars

The main goal of the observations of Sextans was to derive a full star formation history from modeling of the CMD. Unfortunately, the lack of a comparison field and the dominant background contamination makes this sophisticated kind of interpretation impossible.

We have to leave the question open if the extension of the main sequence towards apparently younger stellar populations indeed reflects an extended star formation in Sextans after the bulk of very old stars was formed. In globular clusters blue straggler stars are found at the same location in the CMD; those stars are probably close binary stars that might have merged or experienced mass transfer while one companion evolved on the RGB. BS stars therefore would appear as more massive stars on the younger main-sequence. We analyzed Hubble Space Telescope photometry of star clusters in the Large Magellanic Clouds with ages from three to five Gyrs in order to estimate how many RC stars would be expected to be seen in Sextans if the MSBS stars were indeed intermediate main-sequence stars. We counted stars in the red clump as well as stars in a similar selection of the main-sequence as it was defined for the MSBS sample. This selection suffers from various uncertainties, since it is defined in different photometric systems, and thus we refrain from giving well defined number ratios between MSBS stars and RC stars here. But in general this number ratio is small enough to allow an intermediate old stellar population without forming a prominent red clump that would stand out from the high background contamination. Our observations are consistent with both scenarios of the blue stragglers and the intermediate old stellar population in Sextans.

5.6 Discussion

We presented the first deep wide-field photometric study on the Sextans dSph galaxy. From the comparison of Sextans' RGB with fiducial in the Washington photometric system we derive a metallicity for Sextans in the range from -2.3 dex to -1.7 dex. This result is in excellent agreement with the spectroscopic results of Suntzeff et al. (1993b), but is slightly more metal-poor than the estimate of Mateo, Fischer & Krzemiński (1995). The relative luminosity of the red bump feature in the RGB is consistent with the low mean metallicity of Sextans. Our metallicity determination of Sextans puts this dSph well on the metallicity-luminosity relation of LG dSph galaxies. From the tip of the RGB we obtain a distance

modulus of 19.67 ± 0.12 mag, which is in good agreement with earlier measurements.

We could not find strong evidence in favor of an intermediate old stellar population in Sextans vs. a blue straggler scenario. Nevertheless, the lack of a red clump in the CMD is consistent with the existence of only a minor younger stellar population.

For the first time, we were able to detect a radial gradient in the HB morphology in the Sextans dSph. Metallicity and age might be the responsible culprits for the internal second parameter that governs the HB morphology in Sextans. The correlation of the HB gradient with the radial gradient in the RGB morphology suggests that the HB gradient in Sextans is driven by an internal metallicity gradient. This indicates a formation scenario for Sextans in which star formation started in a large area. With ongoing star formation, gas was expelled or exhausted in the outer regions, while in the inner part the gas experienced self-enrichment and was retained for successive star formation. This remaining gas formed slightly metal-enhanced stars that still have more centrally concentrated orbits.

Motivated by the detection of the population gradient in the Sextans dSph we start a comprehensive study of this phenomenon in LG dSph galaxies in the next Chapter.

Chapter 6

Population gradients in the Local Group Dwarf Spheroidals

The detection of a significant radial gradient in the horizontal branch (HB) of the Sextans dSph leads us to a more detailed investigation of the origin and generality of this phenomenon in other dwarf Spheroidals in the Local Group. Photometric data for LG dSphs that had to be sufficiently deep to reach the HB and had to cover a sufficiently wide field was searched among collaborators and the data archives for this study. This chapter was published as Harbeck et al. (2001).

Abstract

We present a systematic and homogeneous analysis of population gradients for the Local Group dwarf spheroidals (dSphs) Carina, Sculptor, Sextans, Tucana, Andromeda I-III, V, and VI. For all of the Milky Way companions studied here we find significant population gradients. The same is true for the remote dSph Tucana located at the outskirts of the LG. Among the M 31 dSph companions only Andromeda I and VI show obvious gradients. In all cases where a HB morphology gradient is visible, the red HB stars are more centrally concentrated. The occurrence of a HB morphological gradient shows a correlation with a morphology gradient in the red giant branch. It seems likely that metallicity is the driver of the gradients in Sextans, Sculptor, Tucana, and Andromeda VI, while age is an important factor in Carina. We find no evidence that the vicinity of a nearby massive spiral galaxy influences the formation of the population gradients.

6.1 Motivation

Dwarf spheroidal (dSph) galaxies contribute to the faint end of the galaxy luminosity function and may be basic building blocks in hierarchical galaxy formation scenarios. In all Local Group (LG) dSphs an old stellar population (age ≥ 10 Gyr) exists as indicated by the presence of a horizontal branch (HB). The HBs of the dSphs mostly show a bimodal morphology, i.e., both the blue and the red part of the HB are populated. Over the last few years it

has become clear that these apparently simple galaxies actually show a large range of metallicities as well as star to star variations in elemental abundance ratios, indicating that dSphs have experienced a complicated star formation history with various self enrichment processes (Mighell & Rich, 1996; Hurley-Keller, Mateo, & Nemeč, 1998; Gallart et al., 1999; Dolphin, 2001; Shetrone, Côté & Sargent, 2001).

For a few LG dSphs radial gradients in the HB morphology have been reported (e.g., Da Costa et al. 1996; Hurley-Keller, Mateo, & Grebel 1999). In each case the blue HB (BHB) stars have a more extended distribution than the red HB (RHB) stars.

Population gradients are well known for some dwarf irregular (dIrr) galaxies with ongoing star formation, e.g., Sextans A, WLM, Leo A, and IC 1613 as summarized by Grebel (1999). While high-mass dwarf galaxies, e.g. the LMC, tend to show widespread, multiple zones of concurrent star formation, low-mass dwarf galaxies ($10^7 M_{\odot}$) show centrally concentrated younger populations (Grebel, 2000). In particular the transition type dIrr/dSph galaxy Phoenix and the dSph Fornax show a central concentration of the younger stars (Martínez-Delgado, Gallart & Aparicio, 1999; Stetson, Hesser, & Smecker-Hane, 1998).

Radial gradients in the HB morphology can be interpreted as an imprint of the ancient formation process of the dSphs and may help to distinguish different formation scenarios. In this paper we perform a homogeneous study of HB morphology gradients for a large sample of dSphs in the Local Group. We analyze the spatial distribution of BHB and RHB stars, the red giant branch (RGB) stars, and, if present, of red clump (RC) stars of LG dSphs.

6.2 The horizontal branch as a tracer of population gradients

A HB forms in stellar populations older than ~ 10 Gyr and consists of He core burning stars. BHB stars lie blueward of the RR Lyrae strip, while the RHB stars have lower surface temperatures and lie redwards of the instability strip. The first parameter governing the HB morphology of a population is metallicity: Metal rich populations tend to form a red HB, while metal poor populations in general form blue HBs. However, globular clusters with the same metallicity may exhibit very different HB morphologies, demonstrating that additional parameters play a role. For instance, differences in age on a time scale of a few Gyr can have a significant influence on the HB morphology (Sarajedini, Chaboyer, & Demarque, 1997). For a fixed metallicity the HB morphology can change from a completely red HB to an entirely blue HB for population ages between 11 Gyr and 15 Gyr (Lee, Demarque, & Zinn, 1994; Lee et al., 2001). Populations with ages between 1 and 10 Gyr form an RC instead of a HB (Girardi et al., 1998). A red clump is indeed the continuation of the sequence of core He-burning stars, but is formed by stars with higher initial masses. The existence of an RC therefore is a tracer of intermediate age stellar populations in a galaxy. Consequently, the existence of spatial variations in the distribution of core He-burning stars (RHB, BHB, and RC) can reflect either age or metallicity differences, or a mixture of both. Other parameters may still play a rôle. For example, the old, metal rich open cluster NGC 6791 contains a population of stars on the extended blue HB in addition to its expected red HB (Kaluzny &

Udalski, 1992; Liebert, Saffer, & Green, 1994).

In an attempt to separate the effects of age and metallicity, we also will consider variations in the RGB morphology. For a given age, a lower metallicity results in a bluer RGB. A decrease in age has a similar effect (age-metallicity degeneracy). We demonstrate this effect in Fig. 6.1 where we show isochrones (Girardi et al., 2000) for $z = 0.004$ and $z = 0.0004$ for ages of 10, and 14 Gyr. Note that for ages larger than 6 Gyr the effect of age on the RGB morphology is nearly negligible.

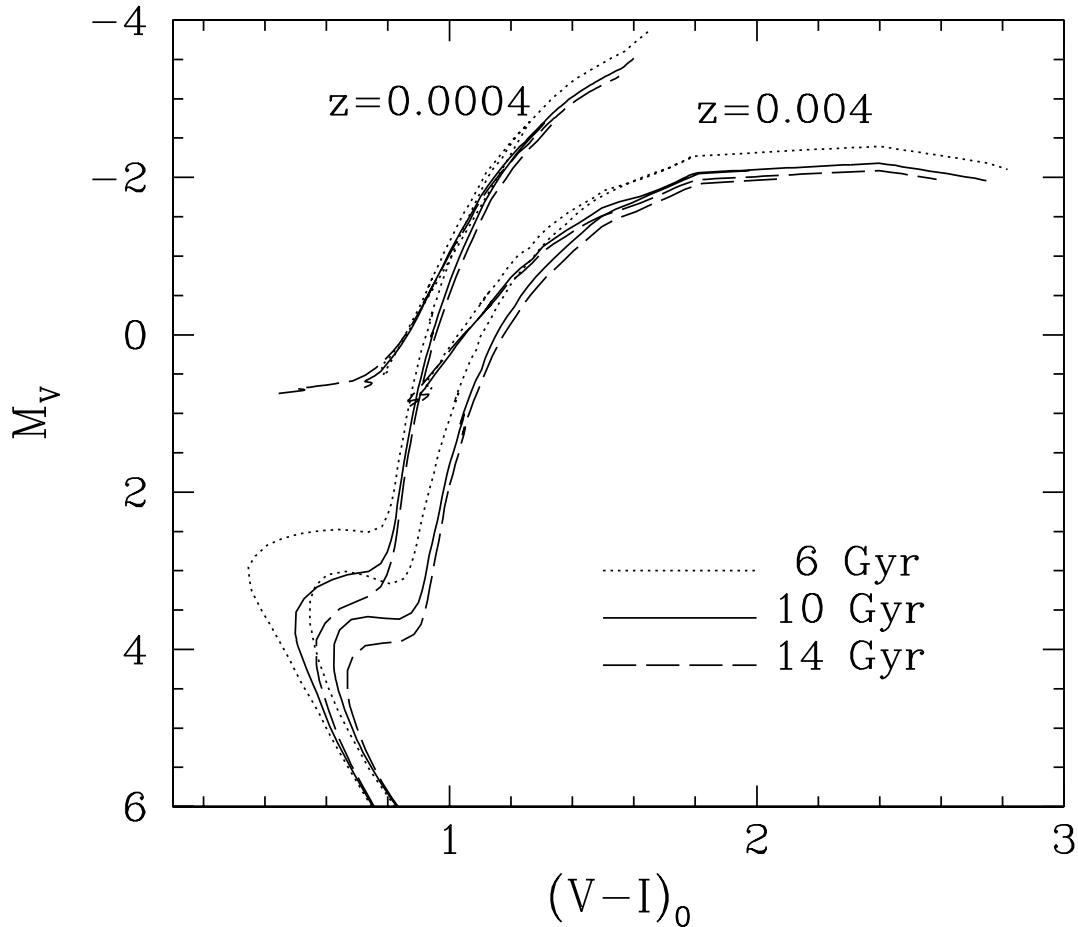


Figure 6.1 : Demonstration of the influence of age and metallicity on the RGB morphology: We show isochrones (Girardi et al., 2000) for $z = 0.004$ and $z = 0.0004$ for ages of 6, 10, and 14 Gyr.

6.3 Data sample and reduction

The LG contains 17 currently known dSphs. We consider here 3 of the 9 Milky Way companions, namely Carina, Sculptor, and Sextans, and 5 of the 6 Andromeda dSphs, Andromeda I-III, V, and VI. In addition we analyze the isolated dSph Tucana. Our sample is restricted to

those galaxies for which deep, wide-field data are available to us. To study the distribution of the blue and red HB stars, observations of a sufficiently large field and deep photometry are required. We present results from our own observations as well as data from the Hubble Space Telescope (HST) archive. The data sources of our sample are summarized in Tab. 6.1, including the instrument used, filter set, and radius covered, and references where available. We show in Fig. 6.2 the observed field of view for each dSph on a Digital Sky Survey image.

All HST observations (the five Andromeda dSphs and Tucana; see Tab. 6.1) were reduced using HSTphot (Dolphin, 2000a). This program performs point spread function photometry on Wide Field Planetary Camera 2 (WFPC 2) (Trauger, 1994) observations with PSFs based loosely on Tiny Tim models (Krist, 1993). It carries out corrections for charge transfer efficiency effects and performs the photometric calibration and transformation to the Johnson photometric system (Dolphin, 2000b). The photometry of the five Andromeda dSphs and Tucana were dereddened according to the extinction maps of Schlegel, Finkbeiner, & Davis (1997). The Andromeda dSphs were observed with the F450W and F550W filters. Da Costa et al. (2000) mention that the zeropoint for the conversion from the F450W filter to Johnson B should be corrected by 0.055 mag. This correction was applied to the $B - V$ color of the Andromeda photometry, leading to slightly redder colors.

The ground based observations were reduced using the IRAF¹ standard CCD reductions and the daophot package (Stetson, 1992) running under IRAF.

Details of the CTIO 4m BTC reductions of Sculptor can be found in Hurley-Keller, Mateo, & Grebel (1999). The data obtained with the Mosaic 2 camera for Sextans was discussed in Chapter 5. Details of the reduction of the CTIO 1.5m data of Carina will be described in Grebel et al. (2003).

The color magnitude diagrams (CMD) for the LG dSphs are shown in Fig. 6.3.

¹IRAF is distributed by the National Optical Astronomy Observatories, which are operated by the Association of Universities for Research in Astronomy, Inc., under cooperative agreement with the National Science Foundation.

Table 6.1 : O

Galaxy	Telescope, Instrument	Filters	r_o ['] ^a	r_c ^a	r_t ^a	$1 - \frac{a}{b}$	Reference
Carina	CTIO 1.5m	C,R	25'	8.8' ^b	29'	0.33	Grebel et al. (2003)
Sculptor	CTIO 4m, BTC	B,R	30'	5.8' ^b	76'	0.32	Hurley-Keller et al. (1998)
Sextans	CTIO 4m, Mosaic 2	C, T ₁	40'	16.6' ^b	160'	0.35	Harbeck et al. (2001)
Tucana	HST, WFPC 2	F555W, F814W	1.7'	0.7' ^c	...	0.48	(HST archive)
And I	HST, WFPC 2	F439W, F555W	2'	1.6' ^d	13.3'	0	Da Costa et al. (1996)
And II	HST, WFPC 2	F439W, F555W	2.8'	1.6' ^d	17'	0.3	Da Costa et al. (2000)
And III	HST, WFPC 2	F439W, F555W	2'	1.3' ^d	6.2'	0.6	(HST archive)
And V	HST, WFPC 2	F439W, F555W	2'	0.5' ^e	...	0	(HST archive)
And VI	HST, WFPC 2	F439W, F555W	2'	1.3' ^e	...	0.23	(HST archive)

Note. — ^a r_o : radius covered by observations, r_c : core radius, r_t : tidal radius. ^b Irwin & Hatzidimitriou (1995) ^c Saviane, Held, & Piotto (1996) ^d Caldwell et al. (1992) ^e Caldwell (1999)

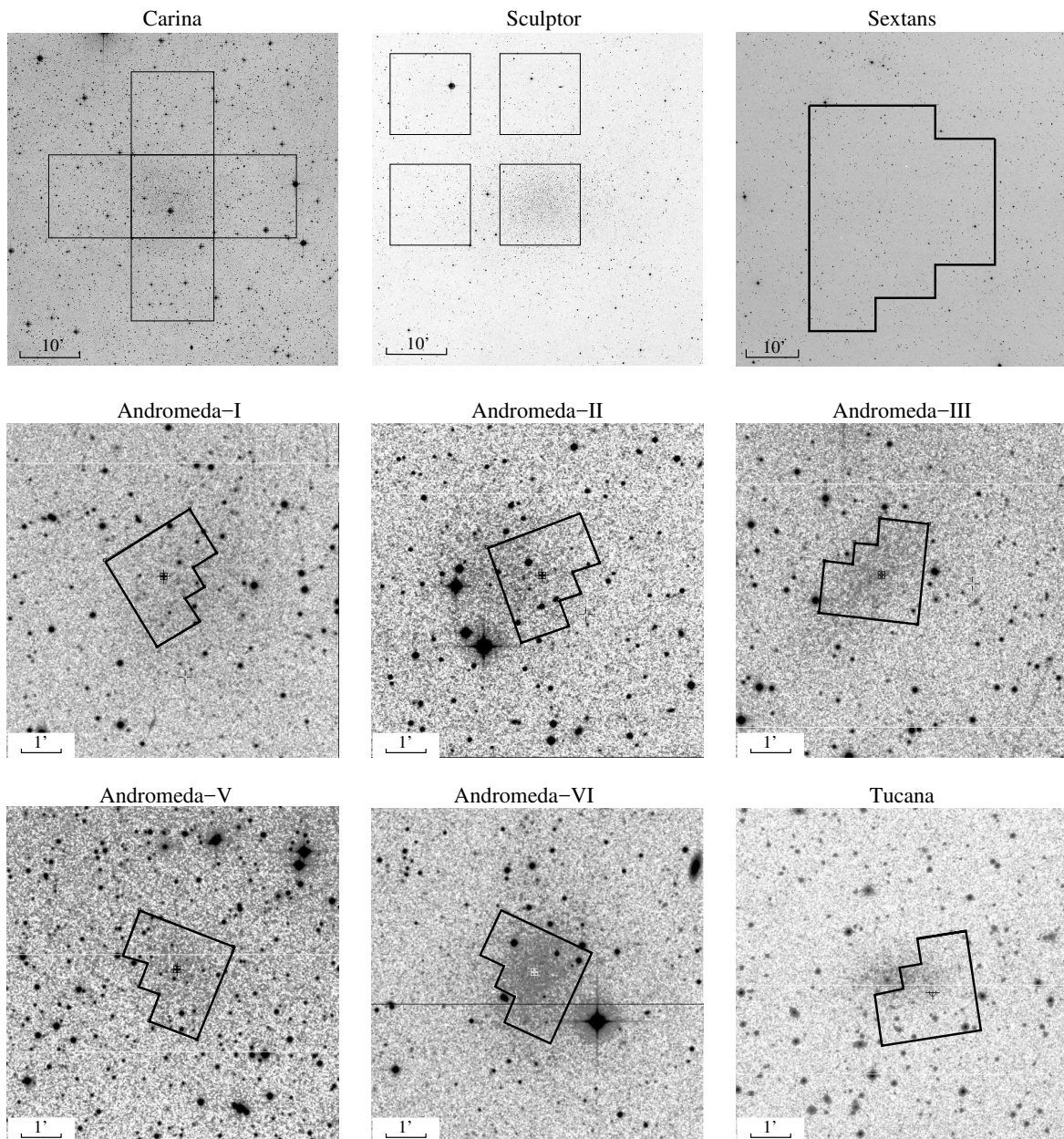


Figure 6.2 : *Digital Sky Survey images of the nine dSphs in our sample with the footprint of the covered field.*

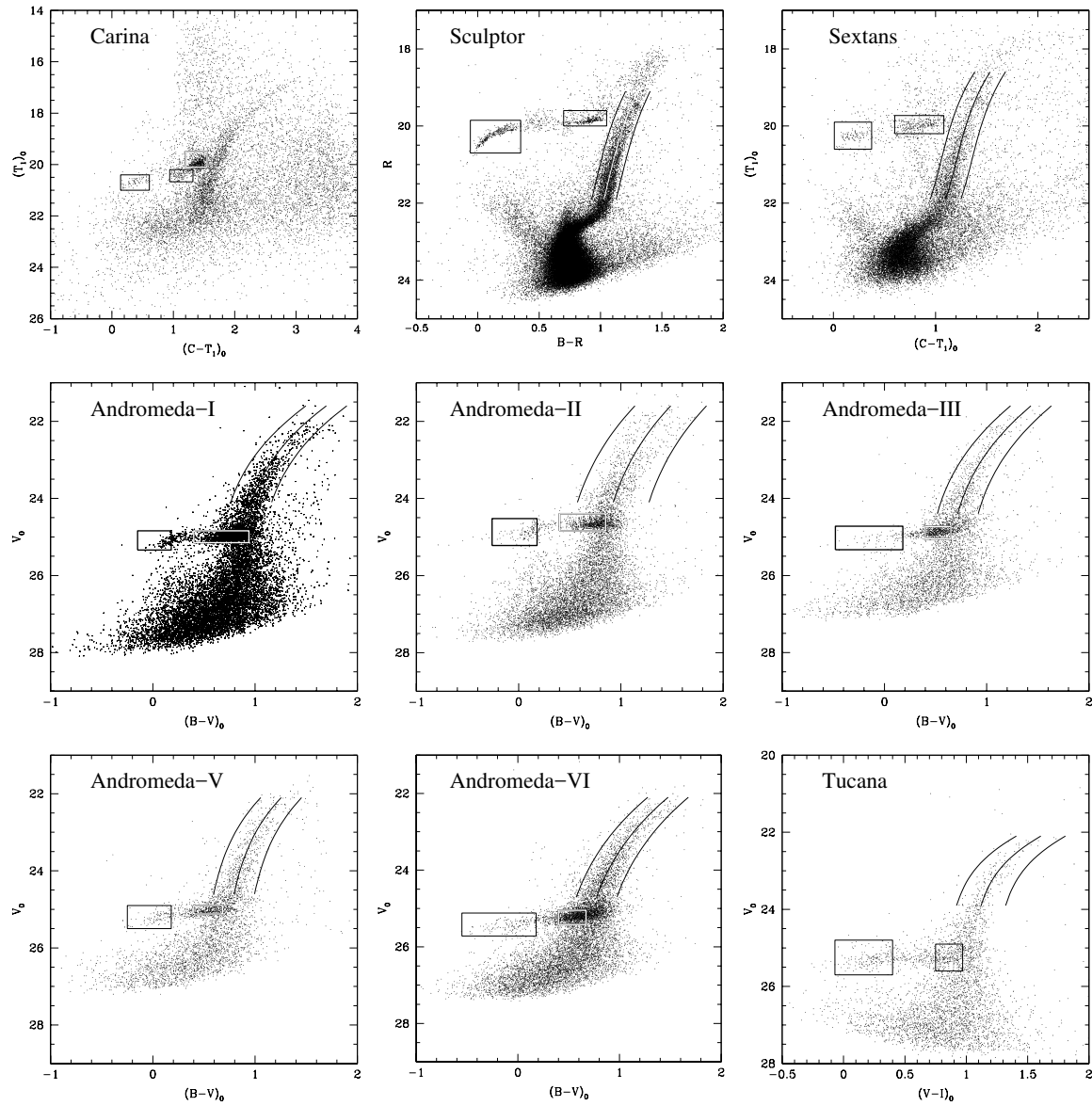


Figure 6.3 : Color magnitude diagrams of all dwarf spheroidals in our sample. The blue and red horizontal branch stars, and the red clump stars in Carina are selected according to the boxes.

6.4 Analysis

To investigate the presence of a possible radial HB morphology gradient for a given dSph we select the blue HB and red HB from the CMD according to the selection boxes in Fig. 6.3. The observations for the dSphs were made using different filter combinations, therefore the color- and magnitude selection vary for the galaxies. Even in the case of the five Andromeda dSphs, which were all observed in the same filters, the HB morphology varies significantly. Due to different contamination of the red HB by the RGB we define the best selection criteria for each individual galaxy to minimize contamination effects. A more quantitative analysis that corrects for this contamination of the HB is performed in section 6.7. The red edge of the BHB selection box and the blue edge of the RHB box are chosen to avoid stars from the instability strip. The boundaries of the instability strip in the different filter sets are: $B - V = 0.18$ to 0.4 (Sandage, 1990); $V - I = 0.4$ to 0.75 ; $C - T_1 = 0.38$ to 0.64 (Harbeck et al., 2001); $B - R = 0.35$ to 0.75 (based on visual inspection of Sculptor’s CMD). In the case of Carina, where a red clump population is visible, we select this region from the CMD to compare its spatial distribution with that of the RHB.

Most of the dSphs in our sample have a non negligible ellipticity $1 - \frac{b}{a}$ as listed in Tab. 6.1. Considering just the radial distance \tilde{r} of a star to the center of its galaxy would ignore this ellipticity and weaken any gradient effects. We therefore calculate for each star an ellipticity corrected distance r , equivalent to the major half axis. In the following we will always use this corrected distance when talking about radial distances to a galaxy center. The centers and position angles for the dSphs were chosen from published work, as referenced in Table 6.1. While different populations may exhibit different centroids (Stetson, Hesser, & Smecker-Hane, 1997), the offsets are small. We therefore search for possible gradients in old and intermediate-age populations by assuming azimuthal symmetry.

We use several different tools to analyze the radial distribution of different populations:

6.4.1 Cumulative radial distribution

We plot the cumulative radial distribution of the BHB, RHB, and, if present, the RC stars. We then apply a Kolmogorov-Smirnov (K-S) test to the radial cumulative distributions, which gives the probability of whether the distributions of the BHB and RHB stars are drawn from the same population.

6.4.2 T_2 statistics of number ratios

We use the number ratio

$$N_{HB} = \frac{n_{BHB}}{n_{BHB} + n_{RHB}} \quad (6.1)$$

which measures the blueness of the HB (Mironov, 1972). N_{HB} varies between 0 for a completely red HB and 1 for a totally blue HB. N_{HB} is calculated for radial bins with the width of a core radius each. We overplot N_{HB} for the individual bins in the cumulative distribution diagrams as histogram bars (Fig. 6.4). If more than two core radii are covered by the

observations this method shows whether there is a trend in the morphological gradient or just a local fluctuation. We also calculate N_{HB} for all stars with a radial distance larger than a single core radius. We refer to this radial selection as the “outer region”, while all stars within a core radius belong to the “inner region”. For Carina this analysis is also carried out to compare the distribution of the RHB and the RC stars.

T_2 statistics, which quantify the probability that two number ratios are derived from the same distribution (Da Costa et al., 1996), is then performed on the two N_{HB} values in the inner and outer region. The T_2 value has a normal distribution around zero with a width of one if the two compared number ratios are derived from the same distribution. T_2 values therefore directly measure at what σ -level two distributions are distinct. During the analysis it turned out that the T_2 -significance of an existing gradient is strongly influenced by the selection of the radii within which N_{HB} is calculated. We therefore decided to separate the inner and outer bin at the core radius for all dSphs to have a unique criterion, even though one could easily tune up the T_2 -significance by individual bin selections for each dSph.

We also define the gradient strength parameter

$$S[HB] = \frac{N_{HB}(r \leq r_c)}{N_{HB}(r \geq r_c)}. \quad (6.2)$$

$S[HB]$ compares the blueness of the HB in the inner and outer part of a dSph, separated by the core radius, and is therefore a measure for the strength of a morphology gradient on the scale length of a core radius. $S[HB] = 1$ for a homogeneous morphology without any gradients. $S[HB] < 1$ indicates a concentration of red HB stars, while $S[HB] > 1$ for a concentration of the BHB stars. We define $S[RC]$ in the same manner to compare the RC with the RHB.

6.4.3 RGB radial distribution and metallicities

We fit the mean ridge lines of the red giant branches (RGB) for all the galaxies by a third order polynomial. This divides the RGB in a red and a blue population (RRGB and BRGB). This ridge line is shifted in the color direction to envelope the red and blue part of the RGB as shown in Fig. 6.3. We tried to include as much of the RGB in this selection as possible and to avoid field star contamination. The same analysis as described for the HB stars is then applied to the RGB stars.

6.4.4 The HB morphology index

We determine the HB morphology index

$$\frac{B - R}{B + V + R}$$

(Zinn, 1986). B , R , and V are the numbers of blue, red, and variable stars in the HB, respectively. The determination of this index is simple in the case of Sculptor, but becomes more complicated for Sextans due to the field star contamination of the RHB. The HB of the

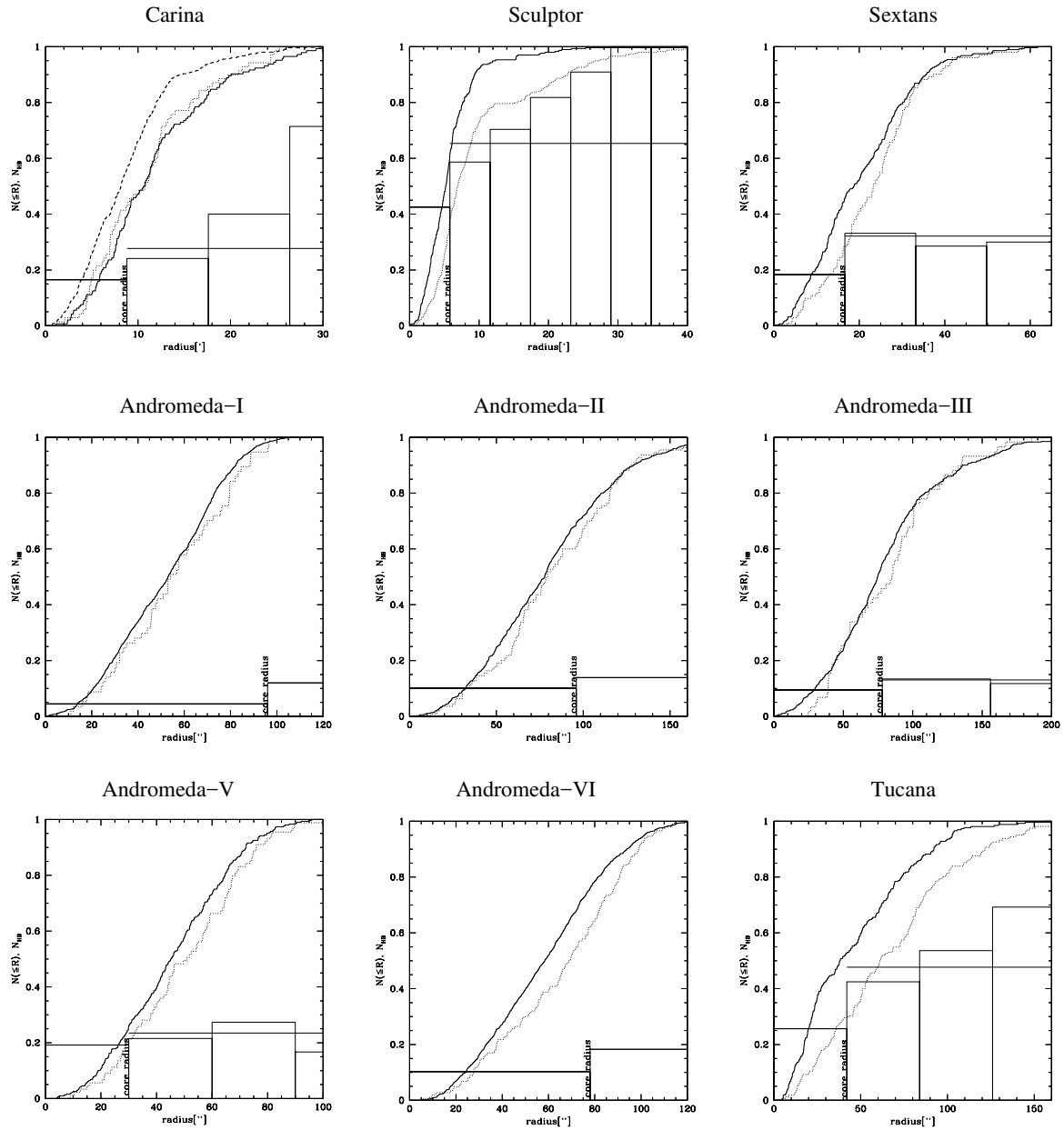


Figure 6.4 : Radial distributions of the blue (dotted line) and red (solid line) horizontal branch (HB) stars for all our sample dSphs. For Carina we plot in addition the distribution of the red clump stars with a dashed line. The selection of the population is made according to Fig. 6.3. For all of the Milky Way satellites a concentration of the red HB or the red clump stars (Carina) can be seen. The histogram bars represent the blueness index N_{HB} for the radii covered by the bars. The vertical line marks the core radius. The strong horizontal line outside the core radius indicates the mean HB ratio in the outer region, if more than two core radii are covered.

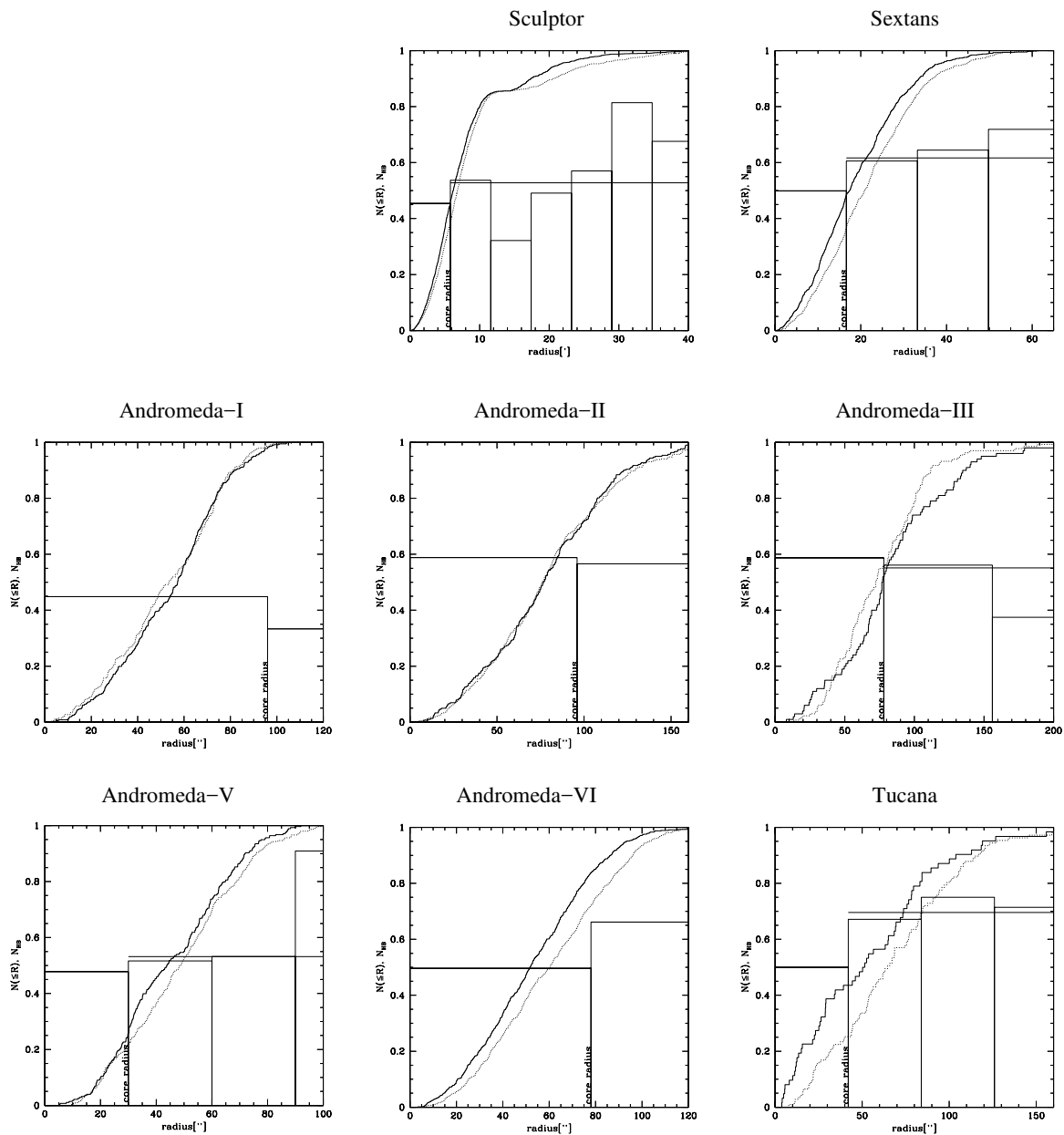


Figure 6.5 : Radial distributions of the blue (dotted line) and red (solid line) part of the red giant branch (RGB) stars for all our sample dSphs. Due to the strong field star contamination we can not analyze the radial distribution of the RGB stars in the Carina dSph. The selection of the red and blue RGB populations is made according to Fig. 6.3. The histogram blocks and numbers have the same meaning as in Fig. 6.4.

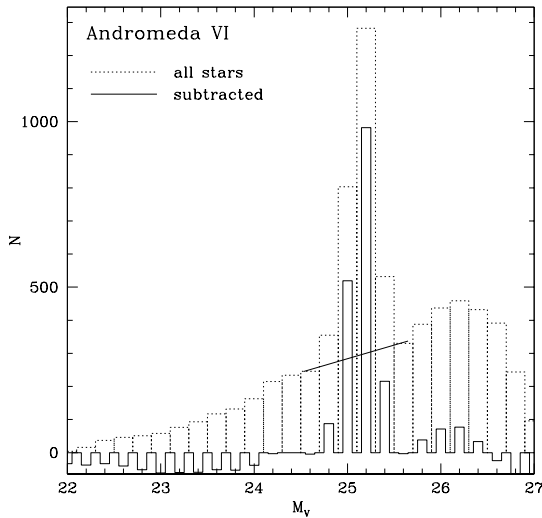


Figure 6.6 : As an example for counting HB stars in the HST photometry where the red HB and the RGB merge, the luminosity function (LF) for all stars with $B - V \geq 0.4$ is shown. At the luminosity of the HB the LF is modelled by a linear function and subtracted from the total. The remaining HB stars form a clearly distinct peak above the zero count level.

distant Andromeda companions and Tucana merges with the RGB, and the number of RHB stars cannot be measured directly. Since we need absolute numbers of red HB stars to compare the HB morphologies of the dSphs we need to correct for this contamination: The luminosity function (LF) is plotted for all stars redder than the red end of the instability strip (considered to be at $B - V = 0.4$; $V - I = 0.8$), as demonstrated in Fig. 6.6. The HB is a clearly distinct peak above the continuum of the RGB LF. We describe the LF of the RGB at the luminosity of the HB by a linear function and subtract this from the whole LF. Counting the remaining stars gives us a good estimate for the correct number of red HB stars. The same method is used to correct for the field star contamination in Sextans' HB, but with an additional cut at the red end of the RHB. The HB morphology index is determined for (i) the whole field covered, (ii) for radial bins with the width of the core radius, and (iii) for the inner and outer bins.

6.5 Radial gradients in the HB morphologies

The radial cumulative distributions of the He core burning stars in our dSphs are drawn in Fig. 6.4 with solid lines for the RHB stars and with dashed lines for the BHB stars. The histogram bars show the N_{HB} values as a measurement of the HB morphology for radial bins with the width of one core radius, while the thick bars show N_{HB} for all stars outside the core radius.

The corresponding statistical values (K-S-Test, T_2 , and S) are listed in Tab. 6.2. For Carina the results of the comparison between the RC and the RHB are listed as well.

6.5.1 The Milky Way companions

Due to the large angular extent of the nearby galaxies we have a strong contamination with foreground stars, especially in Carina and Sextans. Ratnatunga & Bahcall (1985) estimate the expected field star contamination for the globular cluster Pal 3, which is close to Sextans,

Table 6.2 : S

Galaxy	horizontal branch			red clump			red giant branch		
	K-S [%]	T_2	$S[HB]$	K-S [%]	T_2	$S[RC]$	K-S [%]	T_2	$S[RGB]$
Carina	43	0.13	1.0	$5 \cdot 10^{-4}$	3	0.57
Sculptor	$1.8 \cdot 10^{-9}$	6.2	0.65	$5 \cdot 10^{-3}$	4.5	0.86
Sextans	0.5	2.6	0.57	$1.5 \cdot 10^{-4}$	5.3	0.81
Tucana	$5 \cdot 10^{-4}$	4.4	0.54	5	2.9	0.72
And I	44	2.6	0.37	49	2.9	1.3
And II	22	1.2	0.72	99	0.9	1.1
And III	33	0.9	0.71	24	0.5	1.05
And V	24	0.7	0.83	6	1.3	0.9
And VI	0.1	2.7	0.56	$8 \cdot 10^{-4}$	6.6	0.74

to be ~ 9.4 stars in a ± 1 magnitude bin per arcmin² at the HB magnitude of Sextans. In contrast, for Sculptor we expect only 1.3 stars per arcmin². As can be seen in the CMDs, this contamination affects only the RHB and RC number counts, which will be overestimated. The foreground objects have a uniform distribution and therefore let the contaminated RHB and RC star sample appear less concentrated than they actually are. The gradient strengths determined here for the MW companions are therefore lower limits.

All three Milky Way companions considered here have different HB morphologies. Carina is the only one to show a prominent red clump. All three show strong radial population gradients in the morphology of the He-core burning star distribution.

The **Carina** dSph shows no significant gradient in its HB morphology: The K-S-probability that the RHB and BHB stars have the same radial distribution is 43 percent; the T_2 value of 0.13 is consistent with an equal distribution of RHB and BHB stars, as well. But the RC stars show a very significant central concentration compared to the HB. Such a concentration of the younger populations was already suggested by Mighell (1997).

Sculptor has the most significant HB morphology gradient in our sample, as indicated by the high T_2 -value of 6.2 and a K-S-test result of $1.8 \cdot 10^{-6}$. This result confirms the finding of Hurley-Keller, Mateo, & Grebel (1999), based on the same data, and that of Majewski et al. (1999), who use independent observations. Care has to be taken when interpreting the K-S test result due to the properties of the observations with the BTC camera; this camera is a mosaic of 4 chips with 5.4 arcmin gaps. These gaps are smeared out by the elliptical distribution of the stars. But one should keep in mind that the K-S test is strictly defined for contiguous distributions only.

The HB morphology gradient in **Sextans** is not as significant as compared to Carina or Sculptor due to lower number statistics of the sparse blue HB. But with $S = 0.57$ and $T_2 = 2.6$ its gradient is still very strong.

6.5.2 The Andromeda companions

The expected field star contamination towards Andromeda is ~ 5.6 stars per arcmin² in a ± 1 magnitude bin for the HB luminosities. But due to the smaller apparent angular size of the Andromeda dSphs, field star contamination does not play a major role for the M 31 dSph gradients.

The M 31 dSphs show a variety of population gradients. **Andromeda I** seems to show a strong radial HB morphology gradient: While the result of the K-S-test is consistent with no gradient, the result of the $T_2 = 2.6$ and $S = 0.37$ formally suggest a very strong gradient. This is consistent with the result of Da Costa et al. (1996), whose work is based on the same data we used. But the result for the outer bin is based on only 25 stars. This suggests that the HB gradient may become more pronounced beyond the field covered by HST and our result for Andromeda I is not reliable. A larger field coverage would be desirable to clearly establish the existence of a gradient, but no such data exist at present.

Andromeda II does not show a significant gradient (K-S-test: 22%, $T_2 = 1.2$). This result is again consistent with the work of Da Costa et al. (2000). In **Andromeda III** there is no obvious gradient (K-S-test: 33%, $T_2 = 0.9$) either.

The plot of the HB star distribution in **Andromeda V** in Fig. 6.4 suggests a central concentration of the red HB stars. But the distributions of BHB and RHB stars are still consistent with being similar (K-S-test: 24%, $T_2 = 0.7$).

Finally, in **Andromeda VI** there is a significant HB gradient (K-S-test: 0.1%, $T_2 : 2.7$).

6.5.3 The lonesome Tucana

Tucana has a very strong HB morphology gradient ($S = 0.54$) at a high significance level (K-S-test: $5 \cdot 10^{-4}$ %, $T_2 = 4.4$). While all of the other nine dSphs are presumably bound to a massive spiral galaxy, Tucana appears to be isolated within the LG. If Tucana has always maintained a large distance from massive galaxies it would be an example of undisturbed evolution in a dSph. If a HB gradient can form in such an isolated environment, this may indicate that it is created through internal processes in dSphs (Grebel, 2000).

6.6 Metallicity gradients in dSphs seen in the RGB

We analyzed the radial distribution of the red and blue part of the RGB as described in the Section 6.4.3. For Carina the contamination of the RGB by field stars is extremely high, and there is no comparison field for statistical field star subtraction available. It is therefore impossible to make a sensible analysis of possible gradients: Small variations in the selection criterion for the RRGB and BRGB can produce any desired gradient in the RGB morphology. We therefore ignore the RGB of Carina in the further analysis.

The resulting analysis of RGB gradients for the remaining sample of dSphs is plotted in Fig. 6.5 in the same way as in Fig. 6.4 for the HB and listed in Tab. 6.2.

There is a wide variety of RGB morphological gradients: Sculptor, Sextans, Tucana, and

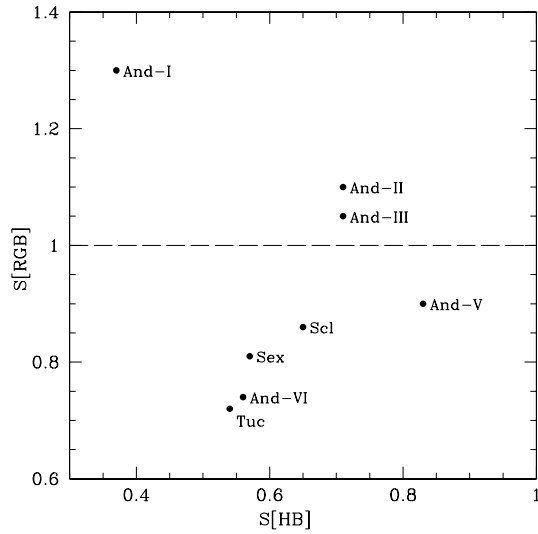


Figure 6.7 : Comparison of the gradient strengths S for the horizontal branch stars ($S[HB]$) and for the red giant branch stars ($S[RGB]$). Galaxies with $S[RGB] \leq 1$ show a central concentration of red RGB stars, while galaxies with $S[RGB] \geq 1$ have a central concentration of blue RGB stars. The gradient strengths for those galaxies with $S[RGB]$ slightly larger than 1 is still consistent with no gradient effects. There is a clear correlation between the gradients in these two populations: According to Tab. 6.3, Sex, Tuc, And VI and Scl have significant gradients both in the RGB and HB. And V has weak gradients, while And II and And III don't show significant gradients. And I suffers from low number statistics.

Andromeda VI show strong and significant concentrations of the RRGB stars. Andromeda II does not show any change in its RGB morphology with increasing central distance.

In Andromeda I+III the blue RGB stars seem to be more concentrated. For Andromeda I this effect has a low K-S-test significance and can be attributed to small number statistics. Indeed, if we reanalyze the HB and RGB gradient strength in the same way as before, but separating at $60''$ instead of the core radius of $96''$, the result is consistent with no gradients in both the HB and the RGB. The apparent concentration of the blue RGB stars in Andromeda III is also very low and the statistical significance of a possibly existing gradient is also very low.

Because the dSphs, except for Carina, which is not considered here, do not contain a significant intermediate age population, we interpret red RGB stars as the more metal rich stars. A central concentration of the red RGB stars would thus imply a metallicity gradient.

The gradient strengths for the HB ($S[HB]$) and for the RGB ($S[RGB]$) are calculated for each dSph with the same radial binning. Therefore $S[HB]$ and $S[RGB]$ can be directly compared, independent of the actual field coverage within a dSph. We compare these two values in Fig. 6.7. All dSphs that exhibit a significant morphological gradient of the HB (Sextans, Tucana, Sculptor, and Andromeda VI) always show a significant concentration of the red RGB stars, too. There are no significant gradients in Andromeda II, III, and V within the covered area. Note that the result for Andromeda I (HB and RGB) may be unreliable. The nice correlation between RGB and HB gradient strength visible in Fig. 6.7 strongly suggests that metallicity is an important driver of the gradients.

6.7 The dSphs in the metallicity-HB-index diagram

A useful tool to compare HB morphologies and metallicities is a plot of metallicity vs. the HB index $\frac{B-R}{B+V+R}$ (Zinn, 1993; Lee, Demarque, & Zinn, 1994; Sarajedini, Chaboyer, & Demarque, 1997). We calculate the HB index as described in the Section 6.4 for the eight

dSphs. The number counts for the blue, variable, and red HB stars are listed in Tab. 6.3 together with the resulting HB index. We calculate the HB index for (a) the whole covered field and (b) in bins with the width of one core radius. We found in the case of Carina that we can not correct for the contamination of the RHB by RC stars. It is also impossible to derive a mean metallicity for the old HB forming population from the RGB only (what currently metallicities are based on), since this metallicity would be dominated by intermediate age stars. Putting Carina into the HB index diagram would be not representative for its HB forming population. Carina is therefore excluded from the investigation in this section.

Table 6.3 : HB

Galaxy	#B	#V	#R	$\frac{B-R}{B+V+R}$	Galaxy	#B	#V	#R	$\frac{B-R}{B+V+R}$
Carina	And I	91	88	1144	-0.8
Sculptor ^a	353	243	299	0.06	I	88	85	1079	-0.8
I ^b	136	98	184	-0.11	II	3	3	31	-0.75
II	139	89	98	0.13	And II	140	55	923	-0.7
III	19	7	8	0.32	I	90	36	614	-0.7
IV	27	18	6	0.41	II	50	19	247	-0.62[0.5ex]
V	20	17	2	0.46	And III	78	81	552	-0.67
VI	5	10	0	0.33	I	39	44	328	-0.7
VII	4	1	0	0.8	II	34	31	196	-0.61
Sextans	102	24	237	-0.37	III	5	6	51	-0.74
I	29	6	120	-0.59	And V	89	111	562	-0.62
II	58	13	104	-0.26	I	19	25	169	-0.7
III	12	3	25	-0.32	II	40	41	244	-0.63
IV	3	2	4	-0.11	III	29	42	153	-0.55
Tucana	162	58	264	-0.2	IV	3	3	8	-0.44
I	48	23	133	-0.42	And VI	177	308	1749	-0.7
II	65	25	79	-0.08	I	114	208	1445	-0.85
III	37	7	36	0.01	II	63	100	315	-0.53
IV	9	2	9	0					

Note. — ^aThe first line of a dSph contains number counts for the whole covered field.

^bThe numbers I, II, ... refer to number counts in the first, second, etc. radial bins.

6.7.1 The whole covered field

In Fig. 6.8 the mean HB-indices of the dSphs are plotted versus the mean metallicities with open circles. The metallicities are taken from the compilation of Grebel (2000) except for Tucana and some of the Andromeda companions. In Andromeda III, the spectroscopic mean metallicity suffers from small number statistics (Guhathakurta et al., 2003); we adopt $[\text{Fe}/\text{H}] =$

-2.0 dex (Armandroff et al., 1993). For Andromeda VI we derive in Sect. 6.7.2 $[\text{Fe}/\text{H}] = -1.6$ dex from our own analysis, and $[\text{Fe}/\text{H}] \sim -1.6$ dex for Tucana, as well. We also show the locations of the MW globular clusters with data from Harris (1996) (filled circles) and for the four Fornax dSph globular clusters based on data of Buonanno et al. (1999) (open stars). Isochrones for three different relative ages are super-imposed (Lee, Demarque, & Zinn, 1994).

It turns out that the LG dSphs are not at the same location in this diagram as the single age population globular clusters of the MW. In particular the dSphs have redder HB morphologies than the mean of the MW GC system, but there are a few very red HB, metal-poor GCs in the MW that compare to the dSphs' HBs. If the HB morphology of the dSphs is indeed determined by age and metallicity only, the location in this diagram suggests that the dSphs may be systematically younger than the MW globular cluster system. On the other hand, there is evidence from deep main sequence photometry that the ages of nearby LG dSphs are comparable to the oldest MW GC clusters, e.g. shown for Sculptor by Monkiewicz et al. (1999); for Carina by Mighell (1997). The $[\text{Fe}/\text{H}]$ -HB-index diagram may not be the most reliable tool to compare relative ages of the dSphs, since many parameters such as mass loss, $[\alpha/\text{Fe}]$ and helium content affect age determinations. Additionally, the star formation histories of the dSph are by far more complex than that of the GCs.

In particular the content of α -elements in dSphs may be an important parameter for the HB morphology. A recent spectroscopic study by Shetrone, Côté & Sargent (2001) of RGB stars in the dSphs Draco, Ursa Minor, and Sextans suggests a decreased α -element abundance ($0.02 \leq [\alpha/\text{Fe}] \leq 0.12$) among these LG dSphs, compared to the Galactic globular clusters. At the present time, the total effect of α -element abundances in the stellar envelope on the HB morphology is not well understood. In general α -elements, especially oxygen, increase the opacity of stellar envelopes. For a fixed mass, stars with increased $[\alpha/\text{Fe}]$ will have lower surface temperatures and therefore will form redder HB stars (VandenBerg et al., 2000; VandenBerg & Bell, 2001). Accordingly, one would expect that dSphs would form bluer HBs than the MW globular clusters. But an enhanced opacity of the stellar envelope, e.g. due to an increased $[\alpha/\text{Fe}]$, should lead to an enhanced mass loss during the RGB evolutionary phase. As a consequence, stellar populations with increased $[\alpha/\text{Fe}]$ might form lower mass HB stars with higher surface temperatures. In this case the reduced α -element content of the dSphs could explain the systematically redder HBs of the dSphs.

Nearly all globular clusters contain RGB stars that show abundance patterns that indicate deep mixing, while the amount of deep mixing stars can vary from cluster to cluster, as reviewed, e.g., in Kraft (1994). Some models and correlation exist that suggest that deep mixing may indeed be a second parameter in globular clusters (Sweigart & Catelan, 1998; Cavallo & Nagar, 2000). If deep mixing were an internal second parameter in dwarf spheroidals, one would expect different abundance patterns among stars with different radial distances to the dSphs' centers.

The five Fornax globular clusters are known to have very red HB morphologies compared to their metallicity (Smith, Rich, & Neill, 1998; Buonanno et al., 1999) and are located at similar positions as the dSphs in Fig. 6.8. According to Buonanno et al. (1999), however, most of the Fornax GCs have ages comparable to the MW GC system.

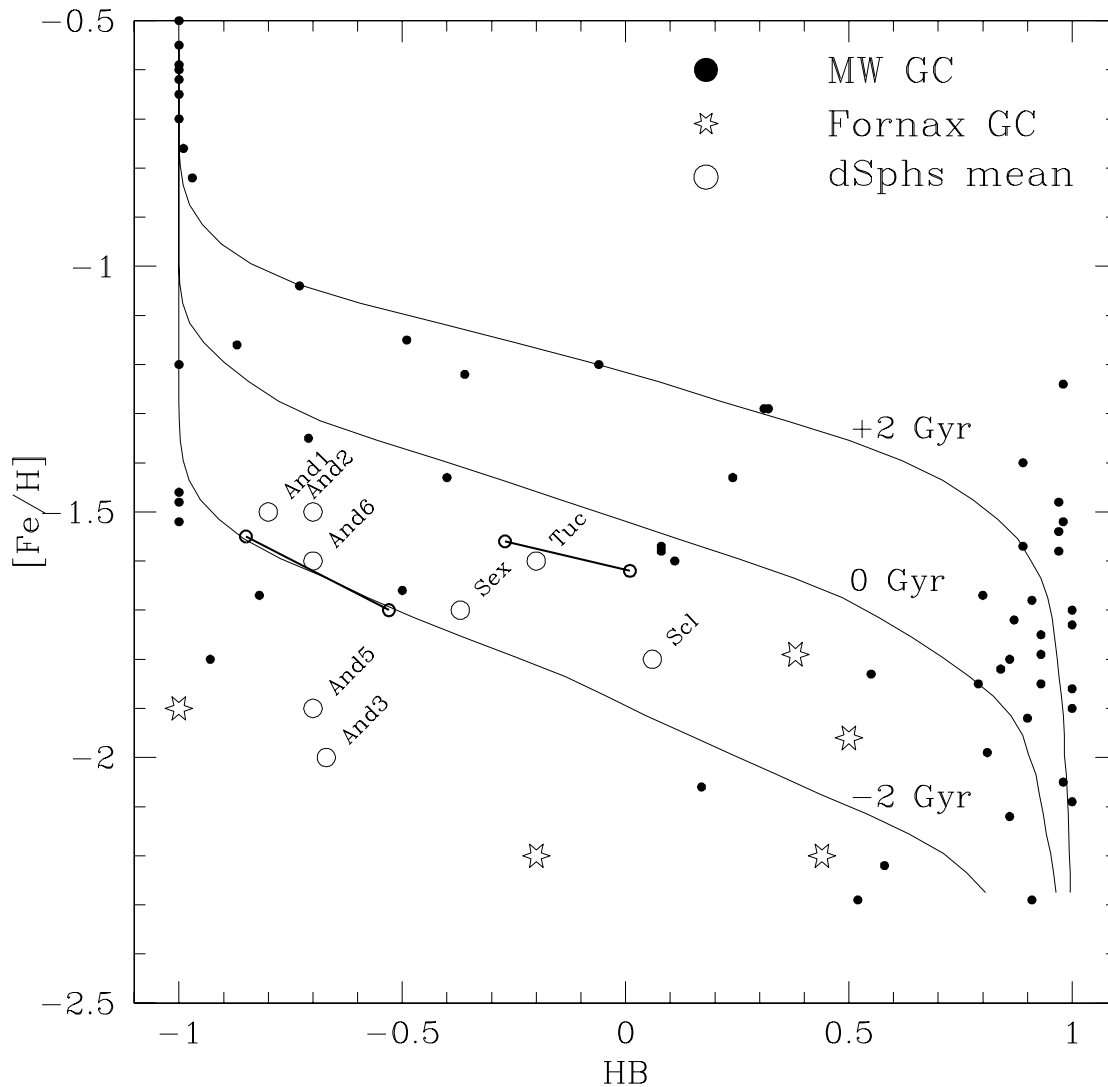


Figure 6.8 : *The Local Group dSphs in the HB index – metallicity plot (open circles). The dSphs’ HBs appear systematically redder for a given metallicity compared to the Milky Way globular clusters (filled circles). This suggests the dSphs may be slightly younger than the GCs. The location of the Fornax globular clusters (open stars) in this diagram indicates they are more comparable to the LG dSphs than the MW globulars. For the two dSphs Andromeda VI and Tucana the mean metallicity and HB indices for the inner and outer regions are drawn with small circles and connected with a solid line. For these two galaxies the HB morphology gradient can be explained by pure metallicity effect.*

6.7.2 Radial dependence of the HB index and the metallicity

Table 6.3 contains the HB morphology indices of the dSphs for different radial bins. The HB morphological gradients detected above are also reflected in the radial dependence of the HB morphology index.

All dSphs observed with the HST have well observed RGBs in the luminosity where star by star metallicity determinations using fiducials are possible. In Sculptor the stars of the upper RGB are saturated and we cannot perform a star by star analysis here. An analysis of the mean color of the lower RGB was found to be too unreliable to obtain meaningful results. In Sextans and in Carina field star contamination would affect photometric mean metallicities. Since in Carina there is a dominant intermediate age population, the RGB color can not become translated into a metallicity, since age becomes an important additional governing parameter.

Tucana and Andromeda VI are the only two dSphs that have significant HB morphology gradients in this sub-sample, where we can derive star by star metallicities. To compare the location of different radial bins in the $[\text{Fe}/\text{H}]$ -HB-morphology diagram, we analyze the metallicity distribution. We use fiducials in the V,I color space (Da Costa & Armandroff, 1990) and in the B,V filters (Sarajedini & Layden, 1997) to transform the location in the CMD of RGB stars into a metallicity. In particular we use fiducials of the globular clusters M15, NGC 6752, NGC 1851, and 47 Tuc with metallicities of $[\text{Fe}/\text{H}] = -2.17$ dex, -1.54 dex, and -1.29 dex, and -0.71 dex according to the sample of Da Costa & Armandroff (1990).

The upper panels of Fig. 6.9 show the metallicity distributions for the inner and outer parts as well as for the whole covered field of Andromeda VI and Tucana. In the lower panels of the same figure the error-folded distribution of metallicities is shown. We assumed a general uncertainty of ± 0.05 dex in $[\text{Fe}/\text{H}]$ plus an additional photometric error folded with the dependence $\frac{\Delta[\text{Fe}/\text{H}]}{\Delta(B-V)}$ of the metallicity on the star's color.

From the $[\text{Fe}/\text{H}]$ distributions of Andromeda VI and Tucana we calculate the median as an estimate for the mean metallicities. Although the median is quite robust against outliers, we exclude stars with metallicities higher than -1.0 dex, which we consider to be field stars. Another source of contamination for $[\text{Fe}/\text{H}] \geq -1$ dex could be CH stars. Both for Tucana and Andromeda VI we derive a mean $[\text{Fe}/\text{H}] = -1.6$ dex. Note the bimodal metallicity distribution in Tucana. The derived $[\text{Fe}/\text{H}]$ for Andromeda VI is compatible with the result of Armandroff, Jacoby, & Davies (1999), but 0.3 dex more metal-poor than the result of Grebel & Guhathakurta (1999). Our analysis estimates Tucana to be 0.2 dex more metal-rich than the study by Saviane, Held, & Piotto (1996).

The visual inspection of the metallicity distributions of Andromeda VI and Tucana (Fig. 6.9) reveals that the ratio of metal poor and metal rich stars changes significantly for different radial selections. For Andromeda VI we derive metallicities of -1.55 dex and -1.7 dex for the inner and outer region, respectively. From Table 6.3 HB indices of -0.85 and -0.55 are obtained for the same regions. The metallicities of the inner and outer bins of Tucana are calculated to be -1.56 dex and -1.62 dex. The HB indices of the bins are -0.27 and 0.01 , respectively. It is worth mentioning that the strong RGB morphology gradients that we de-

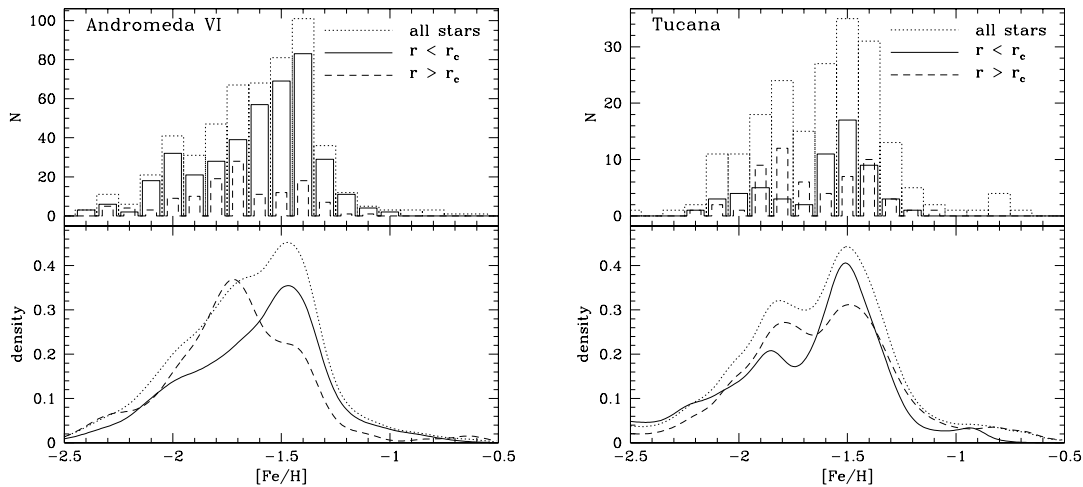


Figure 6.9 : Metallicity distribution of RGB stars in Andromeda VI and Tucana. We show the histogram of the $[Fe/H]$ distribution in the upper half: The dotted bars show the distribution of all stars, while the solid line counts stars within a core radius and the dashed line counts stars more distant than a single core radius. We derive for the inner and outer regions metallicities of -1.55 dex and -1.7 dex for Andromeda VI; -1.56 dex and -1.62 dex for Tucana. The lower part of the diagrams show the normalized density distribution of the $[Fe/H]$ measurements folded by their errors for the same radial selections as for the upper panels. Note that the amplitude of these distributions does not reflect the number of stars. The radial $[Fe/H]$ gradients still come out very nicely. Even the bimodal $[Fe/H]$ distribution in Tucana is still present.

rived in section 6.6 for Tucana and Andromeda VI can be accounted for by a relative small difference in the mean metallicity.

Reality check

We will briefly discuss three points regarding the reality of the apparent gradient in the metallicity in Andromeda VI and Tucana and the influence of field star contamination:

1. Keck/LRIS spectroscopy of bright giants in four Andromeda dSphs (Guhathakurta et al., 2003) directly gives the contamination fraction from a radial velocity membership criterion. The only non-members found (M31 field giants and foreground Galactic dwarf stars) are invariably found well away from the center of the dSphs. In fact, the cross-identified stars in common between the HST star list and the Keck spectroscopy list does not contain even a single non-member - i.e. zero non-members out of a total of 34 cross-ID-ed stars in the four dSphs. The HST star-by-star metallicity estimates (for which we are considering contamination issues) are dominated in number by RGB stars fainter than those in the Keck spectroscopic sample, but this only means that the fractional contamination from foreground Galactic dwarfs will be even lower.
2. Contamination, both by foreground Galactic dwarf stars and M31 field RGB stars (halo

or disk) tends to cause an apparent increase in the estimated $[\text{Fe}/\text{H}]$ of the population. Since contamination is bound to be greater in the outer ($r \geq r_c$) sample than in the inner sample, this goes the wrong way to explain the $[\text{Fe}/\text{H}]$ radial gradient that is observed.

The inner and outer bin in the HB-index- $[\text{Fe}/\text{H}]$ diagram

The location of the inner and outer bins of the two dSphs in the $[\text{Fe}/\text{H}]$ -HB-index diagram is plotted in Fig. 6.8. The positions of the inner and outer bins of the two galaxies in this diagram suggest that metallicity is the main parameter driving the HB gradient. According to the model of Lee, Demarque, & Zinn (1994) there is no *internal* second parameter required to explain the HB morphology gradients in these two galaxies. But taking into account the uncertainty of the HB morphology index (especially to mention the contamination of the HB by the RGB and its correction and the lack of direct RR Lyrae identification), an age spread of 2 Gyr in these two galaxies can not be excluded.

The bimodal metallicity distribution of Tucana

The plot of Tucana's metallicity distribution in Fig. 6.9 suggests a bimodal distribution: The fact that the multimodality exists in the inner and the outer bin, with similar peaks, supports the reality of this effect.

This multimodal metallicity distribution suggests that Tucana formed stars in two or more major events. In the previous section we demonstrated that there is no evidence for a significant age gradient in Tucana. Furthermore, the absence of carbon stars in Tucana (Battinelli & Demers, 2000) as well as the absence of a red clump indicates that there is no significant intermediate age population. The star formation in Tucana therefore happened in a quite narrow age window at least 10 Gyr ago. Different radial distributions of the populations that formed in the different epochs are still visible at the present time by the morphological gradients in the RGB and the HB.

6.8 Global parameters governing the morphology gradients in the HB

To investigate the possible impact of environmental effects, we plot the gradient strength $S[\text{HB}]$ of the dSphs against their absolute magnitude M_V and against their deprojected distance to the nearest massive spiral galaxy (Fig. 6.10 a and b). The absolute magnitude and distances were taken from the compilation of Grebel (2000). As pointed out by Bellazzini, Fusi Pecci, & Ferraro (1996), one should keep in mind that the currently observed distance of the galaxy may not be representative of its orbit and the distance during the star forming episodes; the probability to find a satellite galaxy in its apogalactic orbit position is higher than at the pericenter. The whole sample of galaxies is quite inhomogeneous in gradient strengths and does not show a significant dependence of $S[\text{HB}]$ on the radial distance or the absolute luminosity.

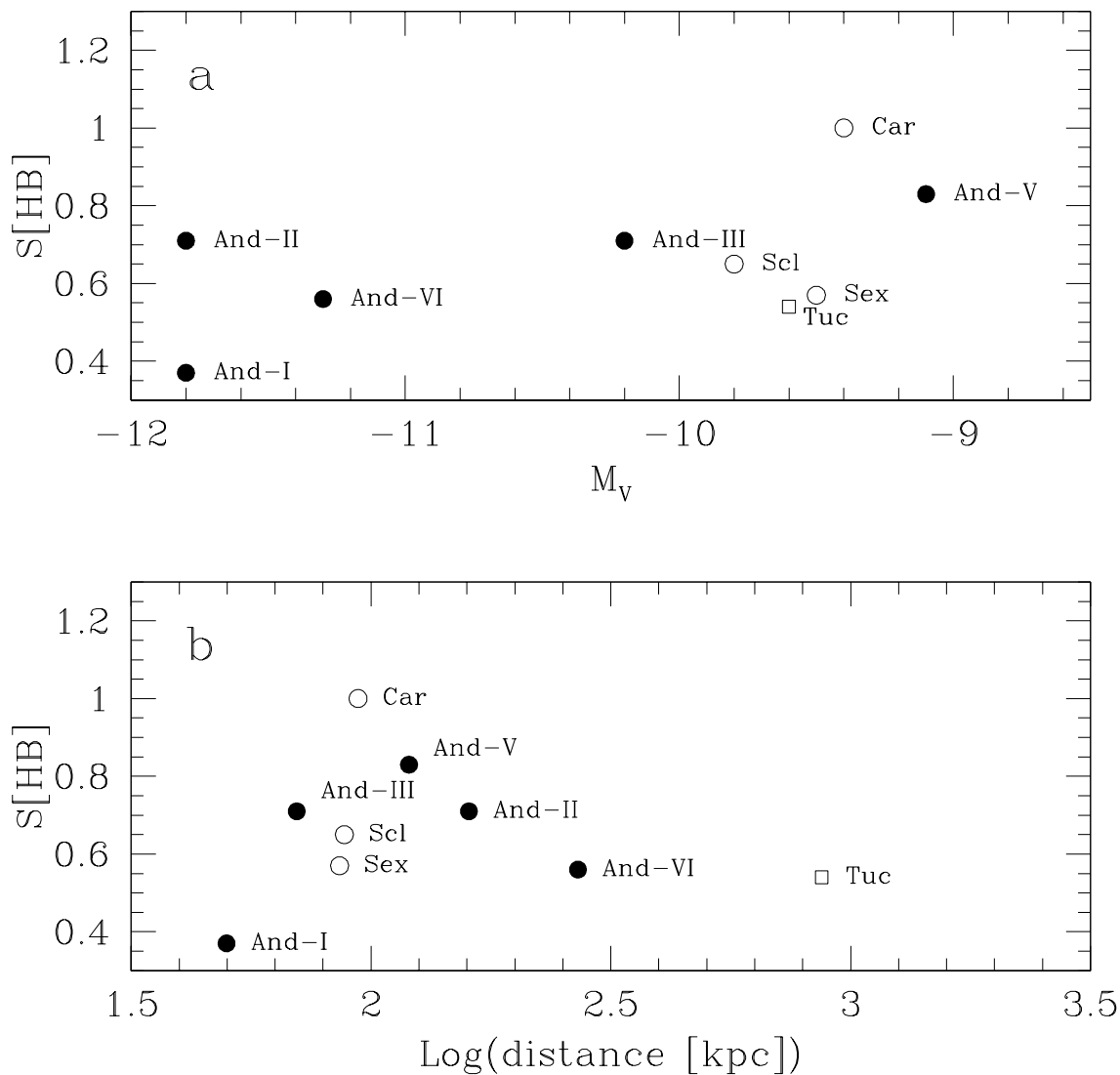


Figure 6.10 : a) Dependence of the population gradient as indicated by the HB gradient index $S[HB]$ (see text for definition) on the absolute luminosity of the dSph. $S[HB] = 1$ corresponds to an equal distribution of the blue and red HB stars, while $S[HB] = 0$ would indicate the maximal concentration of the red HB stars. b) $S[HB]$ compared to the logarithm of the distance to the nearest massive spiral galaxy. Milky Way companions are plotted with open circles, Andromeda satellites with filled dots. The distant galaxy Tucana is plotted with the open rectangle. There is no obvious correspondence between these parameters.

The field coverage of our data compared to the radial extent of the dSphs in our sample varies a lot. But for each of our sample galaxies the data cover an area of at least $1.25 \cdot r_c$. We therefore redetermined $S[HB]$ for all galaxies taking only the central 1.25 core radii into account. This gradient strength will be called $S_c[HB]$. These new gradient strengths $S_c[HB]$ and their significance T_2 are listed in Tab. 6.4. Within this common central radius of $1.25 \cdot r_c$ the gradient strengths for the Milky Way companions and Tucana tend to become weaker (reflected by slightly increased $S_c[HB]$) than before and closely resemble the strength of the M 31 dSphs measured within the same core radius. The case of Andromeda V demonstrates that an insufficient field coverage may lead to completely different results. We expect that the HB morphology variations in the M 31 companions may become more pronounced and significant if a larger area of these galaxies were covered.

A new comparison of the $S_c[HB]$ parameters with the luminosity and distance to the nearest spiral does not reveal any significant correlations either. We therefore exclude the absolute luminosity and the present day radial distance from the nearest massive spiral as parameters governing the HB gradients within the restrictions of our sample.

6.9 Conclusions

We have compared the HBs of nine Local Group dSphs. The existence of a morphological gradient of the HB turns out to be a common, but not a defining, feature of dSphs. If there is a population gradient, the RHB or RC stars are always more concentrated than the BHB stars; there is no counter example in our sample. The main parameters governing the HB morphology are age and metallicity. There are other possible candidates such as stellar rotation, but there is no obvious mechanism that would systematically alter this parameter in the low-density environment of a dSph as a function of radius.

Increasing the helium abundance would lead to lower mass HB stars and would therefore foster the formation of bluer HBs (Lee, Demarque, & Zinn, 1994). For the solar vicinity a correlation between metallicity and helium was found with $\Delta Y / \Delta Z \sim 3$ (Pagel & Portinari, 1998). Increased $[Fe/H]$ should therefore be accompanied by an enhancement of $[Y/H]$ and might overall reduce the effect of metallicity on the HB.

Metallicity as one defining parameter for the HB morphology could produce morphology gradients through a much more efficient self-enrichment of the star forming gas in the central region of a dSph. The driver of the gradient could be the gravitational potential of the dSph which would either retain the star forming gas longer in its central regions, or retain both the gas and newly formed metals (Mayer et al., 2001). The correlation between the central concentration of red RGB stars (supposed to be metal-rich) and the concentration of red HB

Table 6.4 : HB
 $1.25 \cdot r_c$

Galaxy	T_2	$S_c[HB]$
Carina	1.4	1.8
Sculptor	2.1	0.81
Sextans	2.4	0.54
Tucana	2.0	0.66
And I	2.6	0.37
And II	1.6	0.65
And III	0.7	0.73
And V	0.3	1.2
And VI	2.7	0.56

stars (also assumed to be metal-rich) in Fig. 6.7, supports the idea of a global metallicity gradient. Examples where metallicity is an important driver for the HB morphology gradients in our sample are Sextans, Sculptor, Tucana, and Andromeda VI. The location of the inner and outer bins of Andromeda VI and Tucana is consistent with a pure metallicity effect.

In contrast, age as a governing parameter of the HB morphology would support the idea that gas in the dSphs could be retained in the center of the dSphs for a significantly longer time than in the outskirts (Grebel, 2000). In our sample there is no evidence that age is the dominant governing parameter for the HB gradients. At least in the Carina dSph age is a viable parameter that correlates with the gradient of the He-core burning stars, as indicated by the strongly concentrated intermediate age RC. It is very interesting that the HB in Carina does not show a gradient effect. But Carina is the only dSph in our sample that has a dominant intermediate-age population and its star formation history is not directly comparable to the remaining predominantly old dSphs.

The central concentration of the youngest stars has also been seen in Fornax and in the transition type galaxy Phoenix (Stetson, Hesser, & Smecker-Hane, 1998; Martínez-Delgado, Gallart & Aparicio, 1999). One may consider the transition type galaxy Phoenix as an example of a progenitor of a dSph with a strong population gradient.

Overall, in this study we were able to find dSphs with indications of (a) metallicity gradients (Tucana, Andromeda VI, Sextans, and Sculptor) (b) no or weak gradients (Andromeda I, II, III, and V) and (c) age gradients (Carina). Our observations seem to confirm the picture that no two galaxies are alike, not even when they are of the same morphological type.

We found no significant evidence that the proximity to a massive galaxy influenced the formation of an HB gradient, in contrast to van den Bergh's (1994) and Grebel's (1997) correlation between a dwarf galaxy's stellar content and its distance to the Milky Way or M31. The HB and RGB morphology gradient in Tucana is an interesting result due to the fact that this galaxy is not associated with any massive spiral galaxy. It also exhibits a multimodal metallicity distribution, indicative of multiple episodes of star formation. If this dSph was not close to a massive galaxy while it formed stars, environmental effects like tidal gas stripping or an external UV field from a nearby galaxy rather than an extragalactic UV field, could not have introduced the population gradient as far as the progenitors of the HB stars are concerned. Hence it looks as if the formation of population gradients in dSphs is a process that is caused by interior processes within a dSph or that is triggered by external events that occur independently of a nearby massive galaxy.

What could trigger or inhibit the formation of an HB gradient in dSphs? If the formation of a population gradient is the normal mode of dSph evolution it may, e.g., have been stopped due to collisions with intergalactic gas clouds in some galaxies. Such a collision may strip the remaining gas out of the evolving galaxy and end any further star formation. On the other hand an intergalactic cloud may have been captured by a dSph and caused a second star forming epoch, a scenario that is suggestive for Tucana. Yet the shallow potential of a dSph makes it difficult to keep intergalactic gas clouds bound (Hirashita, 1999). Mac Low & Ferrara (1999) found that the amount of gas lost by dwarf galaxies during their star forming epoch depends on the luminosity of the star burst and on the parent galaxy mass. The strength of the star forming time may therefore have been influenced by the starburst itself.

There is also no evidence that the spatial scales on which the population gradients appear are correlated with the core radius of a dSph. The minimum scale on which a population gradient becomes evident can vary a lot. Gradients seem to become most evident at a field coverage of at least one or two core radii. On smaller scales gradients may disappear (e.g., Andromeda I). But the HB morphology gradient in Sculptor can be seen down to a radius of $4''$ ($2/3 r_c$) with a K-S-Test probability of 5 %. To obtain a measure of the scale length for existing morphology gradients requires a field coverage of order of the tidal radius, which is lacking for many galaxies at present. With a sufficient field coverage one could define core radii for the RHB and BHB populations and attempt to correlate them with a natural length scale of a dSph.

6.10 Appendix: The transition type galaxy Phoenix

In the Carina dSph the intermediate old stellar population was significantly more centrally concentrated than the old stellar populations. Is this increasing concentration with decreasing age a general trend among dwarf galaxies? Besides the gas-deficient dSphs with predominantly old stellar populations and the dwarf irregular (dIrr) galaxies with large gas reservoirs and ongoing active star formation there exist a few „transition type” galaxies that share some properties of dIrr and dSph galaxies: They have a predominantly old stellar population, contain neutral hydrogen gas, and experienced recent star formation. This type of galaxies might evolve into dSph galaxies in the future (Grebel, Gallagher, & Harbeck, 2003). We comment here on the spatial distribution of the young stellar populations in the Phoenix dIrr/dSph galaxy.

Data and Reduction

For the transition type galaxy Phoenix deep and wide observations are available in the ESO/VLT archive. Phoenix was observed in July 2000 with the VLT/FORS in the Johnson B and V filters under program number 64.N-0632(A). In each filter three dithered exposures are available with exposure times of 400 s and 300 s in B and V, respectively. FORS’ field of view of $\sim 6'$ covers a large fraction of Phoenix, which has a tidal radius of $\geq 8.6'$ (Mateo, 1998). After bias-correction and flat-fielding the three observations per filter were aligned and coadded, leading to final images with effective exposure times of 900 s and 1200 s in B and V. On these combined images we performed PSF photometry. In this section we are only interested in spatial variations of different subpopulations of Phoenix. The identification of the subpopulations does not require absolute photometric calibration and we proceed with the measured instrumental magnitudes without photometric calibration. The CMD for the transition type galaxy Phoenix is presented in Fig. 6.11.

6.10.1 Different distributions of subpopulations

The CMD of the transition type galaxy Phoenix (Fig. 6.11) shows a young main sequence as well as an RGB and a prominent HB, which partly overlaps with the young main sequence. These features were identified in Phoenix in several earlier studies (Martínez-Delgado, Gallart & Aparicio, 1999; Holtzman, Smith, & Grillmair, 2000; Saviane, Held & Bertelli, 2000). We select different populations from the CMD as indicated by the selection boxes: The red and blue HB stars, the youngest luminous main sequence (referred to as “MS1” later on) and the less luminous, intermediate old population with luminosities fainter than that of the crossing HB (“MS2”). From the isochrone fits by Holtzman, Smith, & Grillmair (2000) to an HST based CMD of Phoenix we estimate typical ages for the MS1 and MS2 samples to 0.1 to 1.5 Gyr and ~ 1.5 to 3 Gyr, respectively. However, stars of lower masses from the youngest stellar population (MS1) will contaminate the MS2 sample.

Martínez-Delgado, Gallart & Aparicio (1999) derived an ellipticity of $\epsilon = 0.3$ and a position angle $\theta = 5^\circ$ for the old extended stellar population of Phoenix, while the young

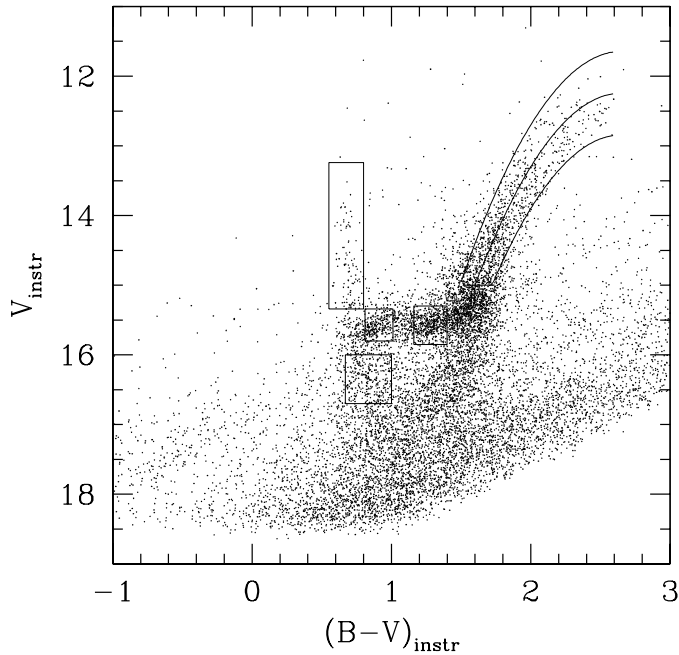


Figure 6.11 : Instrumental color magnitude diagram of the Phoenix dwarf galaxy from VLT/FORS imaging: A prominent old RGB, the HB, and the young main sequence stars are clearly visible. We select several populations from the CMD: The blue and red HB, the young, luminous main sequence (MS1), and the somewhat older main sequence below the HB (MS2). In addition the red and blue parts of the upper RGB are selected.

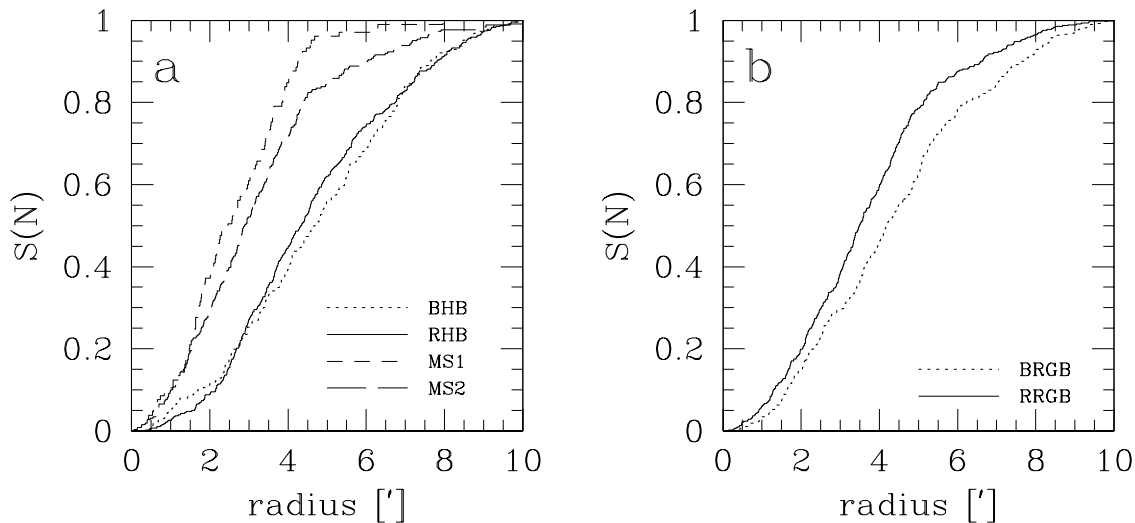


Figure 6.12 : Cumulated radial distributions for populations in the Phoenix galaxy selected in Fig. 6.11: (a) The HB shows only a very weak population gradient (solid line: RHB, dotted line: BHB). The young main sequence populations MS1 and MS2 show a significant central concentration, while the older main sequence stars (long dashed line) are not as much concentrated as the youngest main sequence stars (short dashed line). (b) We also plot the cumulated radial distributions of the red (solid line) and the blue (dotted line) RGB stars. The difference of their radial distributions is evident.

population shows a bar-like concentration with $\epsilon = 0.4$ and $\theta = 95^\circ$. For simplicity we treat all stars as if they followed a similar distribution with $\epsilon = 0.3$ and $\theta = 5$ and determine the distance to the center of this galaxy for all stars.

Fig. 6.12 presents the cumulated radial distributions for the selected subpopulations. The HB shows a weak gradient only. The K-S test and T_2 test result in 26% and 1.5, respectively, and the gradient strength S is measured to 0.83 for the HB. This is a marginally significant gradient in the HB, but again, the RHB stars are more centrally concentrated than the BHB stars. In contrast to the HB stars, the younger stars are considerably more concentrated to the center of this galaxy: The concentration of the stars selected by the MS1 selection compared to the RHB stars is significant with $4 \cdot 10^{-12}\%$ in the K-S test and a T_2 value of 5.4. The slightly older stars from the MS2 selection are not as strongly concentrated as the MS1 sample. Even for these stars the significance of a difference in the distributions of the two young samples is very high: The K-S test probability is 5%, and T_2 yields 3.5. It turns out that the concentration of stars increases with decreasing age. This result is consistent with the work of Martínez-Delgado, Gallart & Aparicio (1999) who also found a concentration of the younger stars. The old stellar population in Phoenix has to be at least as old as 10 Gyr in order to form an HB. We speculate that with ongoing time the star-forming gas of Phoenix might have sunk to the center of Phoenix where the potential well is deepest.

Gradient in the RGB morphology

The RGB of Phoenix covers an outstanding large range in color. To test if there is a gradient in the RGB morphology as well, we select the blue and red RGB according to Fig. 6.11. We cannot distinguish between the age and metallicity effects on the RGB morphology due to the metallicity-age degeneracy. It remains unclear whether this selection traces mainly differences in age effects, or metallicity, or a mixture of both. Phoenix contains a large amount of intermediate old and young stars, the RGB morphology does not directly trace a metallicity distribution. In Fig. 6.12b we plot the cumulated radial distributions for the blue and red parts of the RGB. The red RGB appears significantly more centrally concentrated than the blue one. The K-S-probability for an identical radial distribution is $\sim 7 \cdot 10^{-14}\%$, while the T_2 statistics results in a value of 5.9. Since the RGB morphology becomes bluer with decreasing age, and we know about the strong age gradient in Phoenix, the gradient in the RGB might indicate that the effect of self-enrichment and increasing metallicity is stronger than the age effect. As such we conclude that strong radial gradients in both age and metallicity are evident in the RGB-forming stellar populations of Phoenix.

Chapter 7

Population Gradients seen by SDSS: Sextans and Draco

The Draco dSph and more recently the Sextans dSphs were observed by the Sloan Digital Sky Survey. Studies of population gradients in the dSphs presented in the last two chapters were limited by the covered field. The large coverage of the SDSS allows to study the gradients in Sextans and Draco out to a distance of their tidal radii. Parts of this chapter are published in Klessen, Grebel & Harbeck (2003) or will be part of Grebel, Odenkirchen & Harbeck (2003), in prep.

Abstract

Based on observations by the Sloan Digital Sky Survey (SDSS), we study the large scale distribution of red and blue horizontal branch (HB) stars in the Sextans and Draco dwarf spheroidals. We are able to identify blue HB stars out to a radial distance of order of the tidal radius. We confirm radial gradients in the HB morphology that were found in the central regions in both dSphs in earlier studies. These gradients continue to even larger radii than covered so far and can be traced to a distance of the tidal radii.

7.1 Introduction

The large scale structural analysis of the Local Group (LG) dwarf spheroidals (dSphs) was limited to star counts on photographic plates for a long time (e.g., Irwin & Hatzidimitriou 1995; IH95). With the availability of wide field imagers in the last years, multi-color, deep, and wide field photometry of the extended nearby dSphs became feasible. In the last years it turned out that different sub-populations in the LG dSphs can show very different radial extensions. The horizontal branch (HB) of the predominantly old dSphs is a very useful tool to trace different sub-populations, since the morphology of the HB is affected by several parameters such as metallicity or age (Lee, Demarque, & Zinn, 1994). It turned out in recent studies of LG dSphs that the population of red HB stars often shows a central concentration with respect to the population of blue HB stars (see Harbeck et al. 2001 and references therein; Chapter 6).

Studies on the HB morphology gradients concentrate on radial gradients. The analysis of the detailed structure of the blue and red HB stars in general suffer from two fundamental problems: (i) the still insufficient field coverage of only a few core radii and (ii) the low number statistics of the HB sub-populations. The second problem is an intrinsic problem of the low density dSphs and the sparse BHB population, while we can overcome the first problem with wide field surveys such as the Sloan Digital Sky Survey (SDSS). The Draco dSph and, more recently, the Sextans dSph and its surroundings were observed by the SDSS. We report here for the first time on the distribution and radial gradients of HB stars in these two dSph galaxies at a radial coverage even larger than the tidal radius. Both galaxies are ideal targets to study large-scale population gradients as both were identified to show HB morphology gradients in the central regions (Sextans: Harbeck et al. 2001; Draco: Bellazzini et al. 2002).

7.2 Data, CMD, and star selection

The field of Sextans and Draco were observed in several great circle drift scans made with the SDSS CCD mosaic camera (for details of the survey see York et al. 2000, Gunn et al. 1998, Fukugita et al. 1996). The SDSS five color imaging data are reduced by a standard photometric pipeline. From the resulting data products we extracted objects that are recognized as bona fide stars due to their point spread function. The data for Sextans were selected from the “staging” database, which is a preliminary database to provide fast access to the incoming SDSS data. These data will become recalibrated before they will be made available to the public in the Data Release 1 in 2003. Nevertheless, the changes in the photometric calibration are expected to be small and will not affect the classification into blue and red horizontal branch stars. The Draco data was taken from the SDSS Early Data Release Release (Schneider et al., 2002).

The color-magnitude diagram (CMD) of Sextans is shown in Fig. 7.1. Only stars within the central 30 arcmin are plotted. The red giant branch as well as the horizontal branch with its blue extension are visible. To trace the position of the instability strip in the SDSS photometric system, we plot the cross-identified variable stars from the study of Mateo, Fischer & Krzemiński (1995) into the CMD.

Following the strategy used in chapter 6, we select the red and blue HB (RHB and BHB, respectively) stars from the CMD according to the selection boxes in Fig. 7.1. We avoid to include stars from the identified instability strip. The BHB clearly separates from the background, while the RHB selection suffers from a substantial background contamination. To estimate this background contamination of the RHB we count stars that would match the RHB selection criterion in the one square degree comparison field limited by $151^\circ \leq \alpha \leq 152^\circ$ and $2 \leq \delta \leq 3$. We found that we have to expect 0.015 ± 0.002 field stars per square arc minute in the RHB selection box. In the RHB selection box of Fig. 7.1 we therefore expect ~ 85 field stars.

The same strategy is applied to the Draco dSph (see Fig. 7.2). The boxes in Draco’s CMD indicate the selections for BHB and RHB stars. The contamination by background stars is

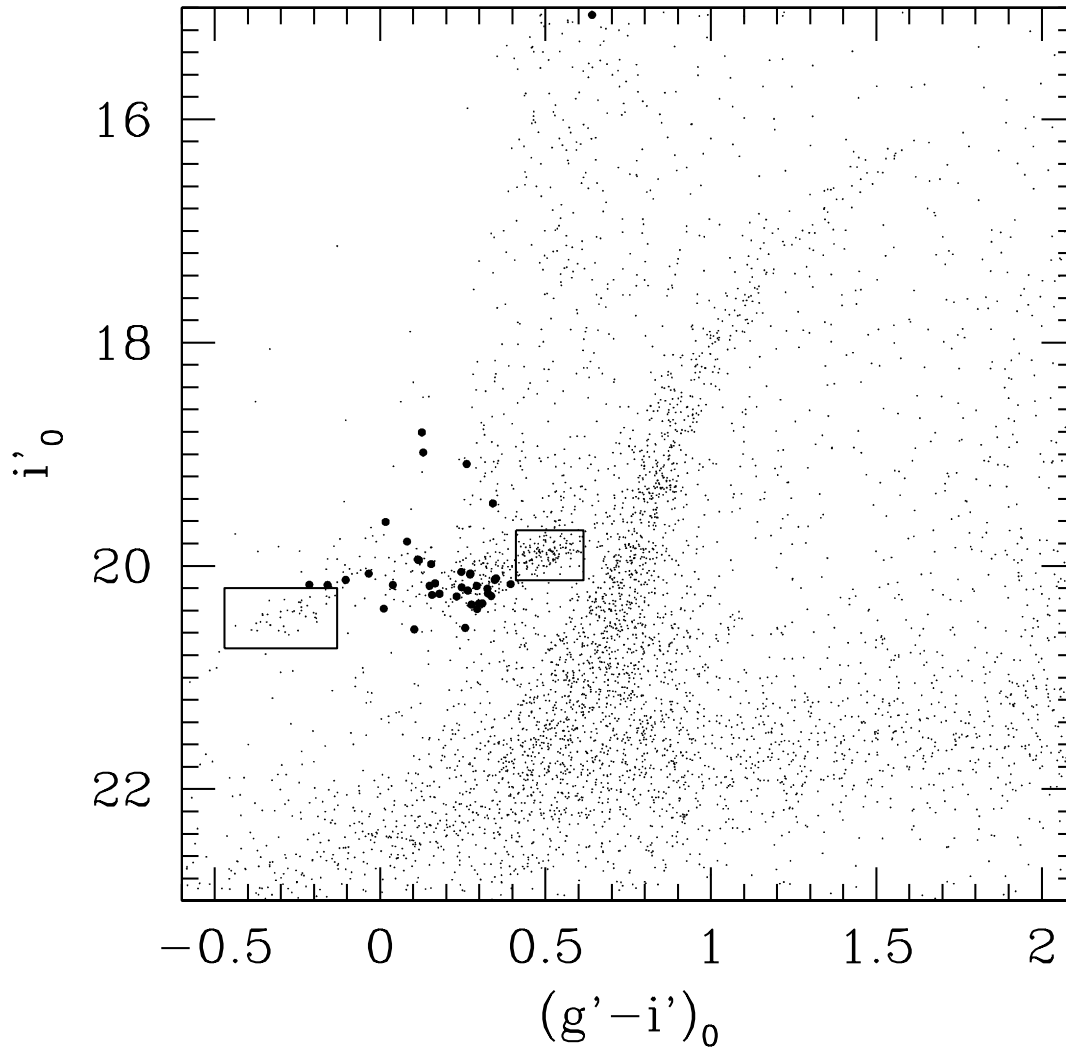


Figure 7.1 : CMD of the Sextans dSph based on SDSS observations in the g' and i' band. All stars within a radius of $30'$ are plotted. Variable stars crossidentified to Mateo, Fischer & Krzemiński (1995) are plotted with filled circles. The boxes define selections for red and blue horizontal branch stars.

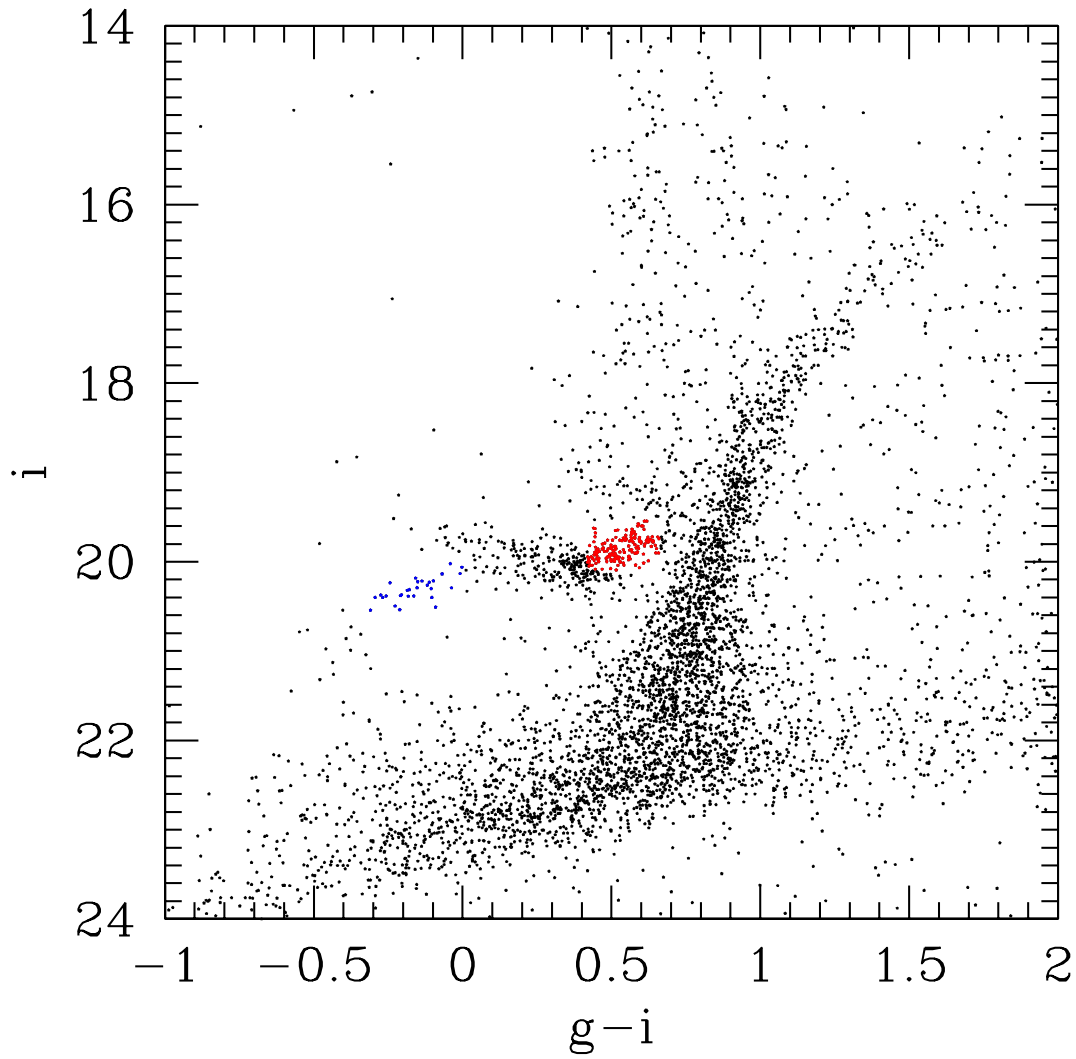


Figure 7.2 : CMD of the **Draco dSph** based on SDSS observations in the g' and i' band. All stars within the central $20'$ are plotted. The red and blue dots define selections for red and blue horizontal branch stars.

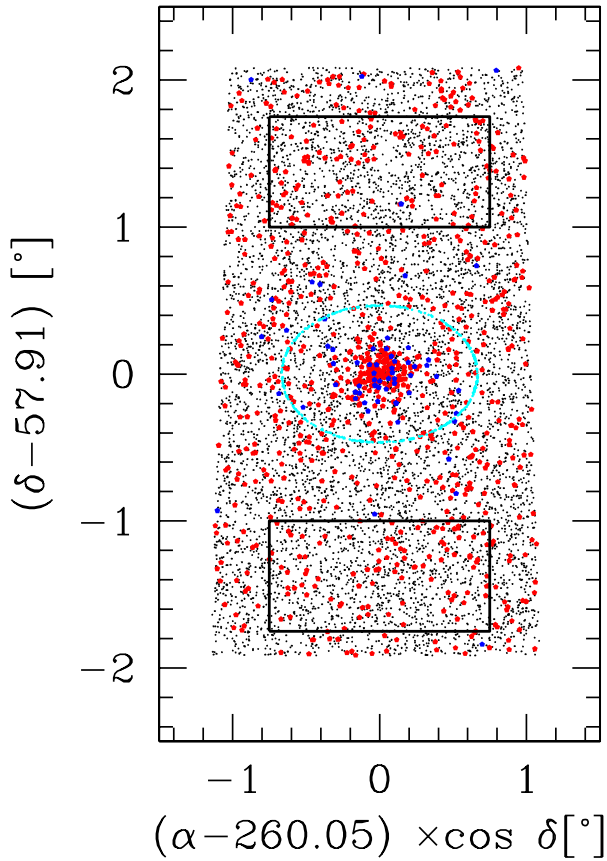


Figure 7.3 : *Spatial distribution of stars in the Draco region. The small black dots are positions of stars with $17 \leq i' \leq 18$ to trace the overall stellar density in the fields. The central concentration in the middle of the field is the Draco dSph. The blue ellipse indicates the tidal radius of $\sim 40'$. Stars matching the BHB and RHB selection criteria are plotted with blue and red dots, respectively. The background contamination is determined in the boxed regions.*

measured in two comparison fields (see Fig. 7.3). We find a field star density of 0.023 ± 0.001 background stars per square arcminute for the RHB selection, and 0.0003 ± 0.0003 background stars per square arcminute for the BHB selection.

7.3 Radial Gradients in the HB morphology

For both the Draco and Sextans dSph stars matching the BHB and RHB selection criterion (see Fig. 7.1 and Fig. 7.2) were extracted from the star catalog. For all stars projected distances to the centers of the galaxies were calculated, taking the ellipticity of the galaxies into account. All radial distances therefore refer to the major half axis.

7.3.1 Draco

In Fig. 7.3 we show the spatial distribution of stars in the Draco environment. BHB and RHB stars are plotted with blue and red filled circles, respectively. The central concentration towards the center of Draco is evident, although for the RHB stars the large contamination by foreground objects is evident. For the BHB stars, there is an excellent contrast to the foreground. Note that the density of background objects is roughly a factor of 80 smaller than for the RHB selection.

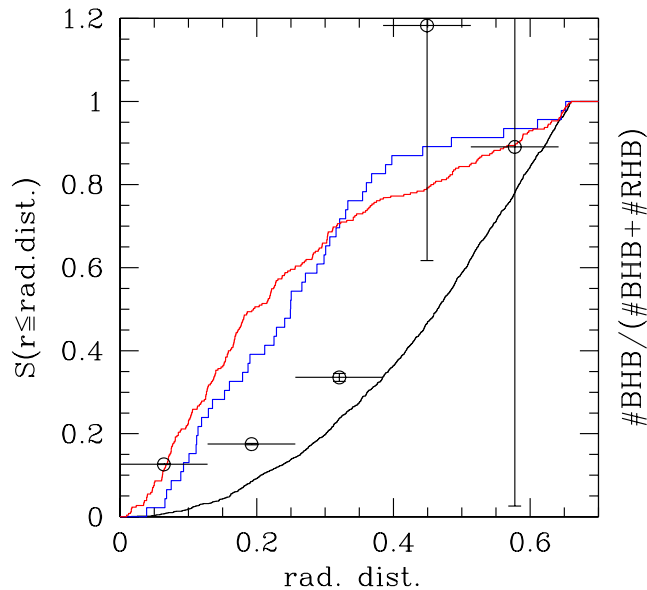


Figure 7.4 : Cumulative radial distribution of RHB and BHB stars in Draco (red and blue lines). Although a central concentration of RHB stars is suggested in the center, the strong foreground contamination is dominating the distribution of RHB stars in the outer regions. The distribution of foreground stars is plotted for comparison with the black line. The histogram bars show the number ratio $N_{HB} = \frac{\#BHB}{\#BHB + \#RHB}$ for radial bins of one core radius width. Note that this ratio is corrected for foreground stars. The increasing blueness of the HB morphology for the outer regions is evident.

We plot cumulative radial distributions of RHB and BHB stars in Fig. 7.4 with blue and red lines, respectively. For comparison, the distribution of field stars selected by $1.5 \leq (g' - i') \leq 2.5$ and $18 \leq i' \leq 21$ is drawn with a black line. The red HB stars appear more centrally concentrated than the blue HB stars, but in the inner 0.3° only. In the outer parts of Draco, the high contamination by foreground stars is dominating the shape of the RHB stars' distribution. A detailed investigation of this uncorrected cumulative distribution is therefore meaningless. In the same figure we plot the HB ratio N_{HB} for radial bins with the width of one core radius (7.7 arcmin) as histogram bars. The N_{HB} ratio is corrected for foreground objects. There is an apparent increase in the N_{HB} index towards the outer regions, indicating a central concentration of the red HB populations. The errorbars in the bins are based on the uncertainty of the foreground determination only. At a radial distance of $r \sim 0.4^\circ$ the RHB stellar population of Draco is apparently lost in the noise of the foreground, while the BHB stars still stand out.

We test the significance of the HB gradient in Draco using the T_2 statistics (see Chapter 4) for the two radial bins $0 \leq r \leq 0.2^\circ$ and $0.2^\circ \leq r \leq 0.4^\circ$. The resulting T_2 value of $T_2 = 1.8$ corresponds to a $1.8 - \sigma$ significance that the N_{HB} ratios in the two bins are different. Our result confirms the HB gradients in Draco found by Bellazzini et al. (2002) in the inner 0.25° and at even larger radial distances.

7.3.2 Sextans

Sextans is a very extended object on the sky. We present isodensity contours of BHB and RHB stars in Fig. 7.5. Due to the small amount of stars (~ 6000 RHB and ~ 420 BHB stars distributed over a large field of 40 square degrees), simple star counts in cells suffer from local statistical fluctuations. Instead we use an adaptive kernel smoothing technique to derive stellar densities: Each star in a stellar distribution plot is replaced by a Gaussian with a FWHM equal to the distance of the nearest 20th star. This technique allows for well resolved

density maps in the central dense regions but degrades the spatial resolution in low density regions, while reducing the effects of density fluctuations. The dashed ellipse in Fig. 7.5 indicates the tidal radius (160') of Sextans according to IH95. The red and blue lines refer to the density of the RHB and BHB stars at levels of 10,30,50,70,90,99% of the central peak density.

The red HB stars show a strong central concentration compared to the BHB stars. This is consistent with the result by Harbeck et al. (2001) who found a significant radial gradient in Sextans' HB morphology, but on a scale of the central four core radii only. Note that the RHB stars contours are lost in the background contamination on a much smaller radial distance than the BHB stars due to the different background contamination.

The BHB and RHB stellar populations seem to have different centers, that seem to be caused by a small number of BHB stars: in a Monte-Carlo experiment we distributed ~ 400 stars in a Gaussian profile with a width comparable to that of the tidal radius of Sextans and measured the positions of the centers of the stars. Offsets of order of the difference of the BHB-RHB centers can easily be produced just due to the statistical fluctuations.

The contour plots are based on star counts with adaptive kernel smoothing. Since especially for the low density this data processing may cause artificially larger extended isopleths, we analyze the unsmoothed, but binned, and foreground corrected, radial distribution of the red and blue HB stars. Since the different centers of the BHB and RHB stars are most likely not real, we assumed for both populations the center determined by IH95. Due to the small number statistics of the HB stars, a complete recalculation of all structural parameters such as ellipticity, position angle, and tidal radius, would be dominated by noise, and we also use the IH95 ellipticity and position angle for both populations.

In elliptical bins with the width of one core radius ($\sim 20'$) we counted the number of stars in the RHB and BHB selection box and corrected the numbers for the area covered. We corrected the derived number counts for the estimated density of foreground stars. Fig. 7.6 shows the HB morphology ratio dependent on the radial distance. An increasing HB index for increasing radial distances is evident, even well beyond the distance of 60' covered by Harbeck et al. (2001). Nevertheless, at larger radial distances the HB ratio becomes dominated by noise, mainly due to the uncertainty of the background subtraction in the RHB selection.

7.4 Conclusions

We analyzed the large scale distribution of blue and red HB stars in Draco and Sextans dSphs. In both cases a radial gradient in the HB morphology could be detected out to radial distances as large as a tidal radius. In both galaxies, but in particular in the case of Draco, there appear to exist BHB stars well beyond a tidal radius. The existence of population gradients in dSphs demonstrates that these galaxies are dynamical multi-component systems. In a recent work, Kleyna et al. (2002) use spatially resolved measurements of the velocity dispersion of RGB stars in Draco dSph to constrain its dark matter content and the shape of the dark matter halo. One basic assumption of their model (Wilkinson et al., 2002) is that dSphs are a single

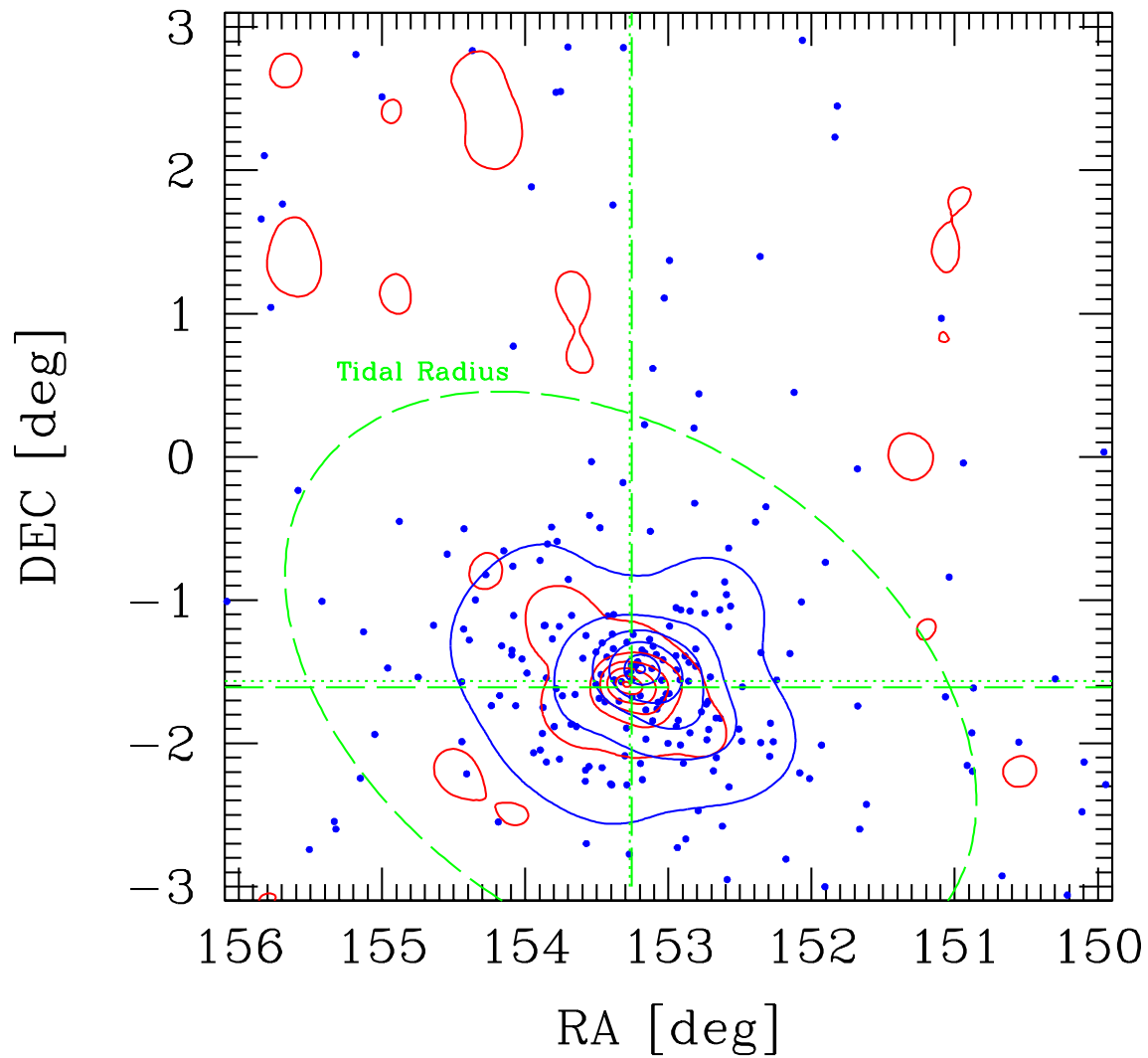


Figure 7.5 : Contour-plot of the blue (thin line) and red (thick line) HB stars of Sextans. The contours are chosen to the 80, 60,40,20 % level of the peak stellar density. The filled dots represent the locations of all selected blue HB stars. The dashed ellipse shows the tidal radius according to Irwin & Hatzidimitriou (1995). The green lines indicate the mean center of the BHB and RHB stellar populations.

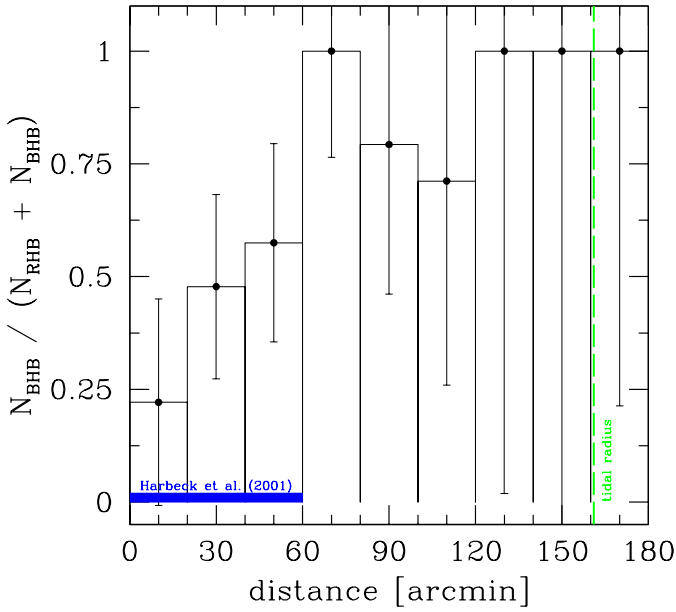


Figure 7.6 : *The radial gradient in the HB morphology in Sextans: The histogram bars indicate for the radial bins the numerical ratio $N_{\text{HB}} = \frac{N_{\text{BHB}}}{N_{\text{BHB}} + N_{\text{RHB}}}$.*

dynamical system. Kleyna et al. (2002) found an increasing velocity dispersion of RGB stars in Draco with increasing radius (limited to the inner two core radii). The authors derive from a model for the velocity distributions the dark matter distribution of Draco's halo to be slightly more extended than a flat rotation-curve potential. A possible problem of this modelling is that for larger radii stars of the more-extended sub-population (BHB) would be favoured in the target selection, while in the central regions the more centrally concentrated population (RHB) would be selected in kinematic studies. As both sub-populations differ in their spatial extent, they also must have different kinematics. Future studies of dark matter halos from stellar kinematics will have to take the existence of population gradients in dSphs into account; dynamical profiles of a sub-population have to be compared to their spatial distribution. Additional parameters like stellar metallicities will be required to determine the membership to a certain sub-population in a dSph. It is therefore essential to investigate the underlying gradient in stellar parameters that is producing the HB gradient.

Harbeck et al. (2001) could demonstrate for the two dSphs Tucana and Andromeda VI that the appearance of the HB radial gradients can be explained by an underlying metallicity gradient. Of course other second parameters like age or α -element abundances could play a role. The striking question is if the underlying gradient varies continuously with increasing distance to the center, or if we can see two discrete populations with distinct metallicities and different radial distributions. As pointed out by Majewski et al. (1999) for the example of Sculptor dSph, the existence of two distinct red bumps in that dSphs supports the idea of two distinct sub-populations. Harbeck et al. (2001) found in the Tucana dSphs evidence for a bimodal metallicity distribution that would support the model of distinct populations rather than a smooth transition between the populations at least for these two galaxies. In the CMD of Sextans (Fig. 7.1) two such red bumps can be identified on a good-will basis. Bellazzini, Ferraro, & Pancino (2001) could clearly identify two distinct red bumps in Sextans.

It is important to derive good spectroscopic metallicities for large samples of Sextans' and Draco's RGB stars to get a accurate, and more important, an unbiased idea of the metallicity distribution and its correlation with the population gradients.

Chapter 8

Conclusions and future prospects

8.1 Is the CN problem in GCs solved?

The bits and pieces of the nearly thirty years old problem of chemical inhomogeneities in GCs are now beginning to form a coherent picture. Thanks to new large telescopes and instruments such as FORS2 at the VLT, and in the future FLAMES at the VLT, our understanding of stellar evolution in GCs and of the impact of the dense environment is rapidly improving. Recent studies of element variations on the main sequence in GCs, including my work presented in Chapter 3, demonstrated that the element abundances in the envelopes of these low-mass GC stars must have been altered by nuclear processes that happened outside of these stars. Nucleosynthesized material has to have been accreted by stars during the lifetime of the GCs. It remains to be more closely investigated whether primordial enrichment or pollution by stellar ejecta during the evolution of a globular cluster are the responsible mechanisms. The bimodality in CN absorption strengths remains a challenge since it cannot completely be explained by saturation effects of molecule formation.

In Chapter 2 we argued against the hypothesis that CN variations trace increased mixing on the RGB; rotationally induced mixing accompanied by increased mass-loss could not be identified as a dominant second parameter of the HB morphology. My work on 47 Tuc in Chapter 3 demonstrates that CN molecule variations might not be a suitable tracer of mixing processes: This cluster shows from the tip of the RGB down to the faint main sequence bimodal CN variations; there is no indication for a point along the evolutionary path where the onset of internal mixing apparently altered the CN absorption strength. If internal mixing dredged up CNO processed material to the surface of 47 Tuc stars, its effect on the relative C and N abundances might be too small to alter the imprint of primordial variations or of accreted material. While the relative C and N abundances change very slowly in the CNO cycle, the carbon isotope ratio $^{12}\text{C}/^{13}\text{C}$ is much more sensitive to partial processing. In a recent study, Shetrone (2002) demonstrated that the carbon isotope ratio indeed changes along the RGB at the luminosity of the red bump in the globular clusters M 4 and NGC 6528. The carbon isotope ratios change from their initial (high) value at the subgiant branch to a low, near CNO-equilibrium value at the red bump (see Fig. 8.1). This change of the carbon isotope ratio is a direct proof of the onset of extra mixing on the RGB at the red bump.

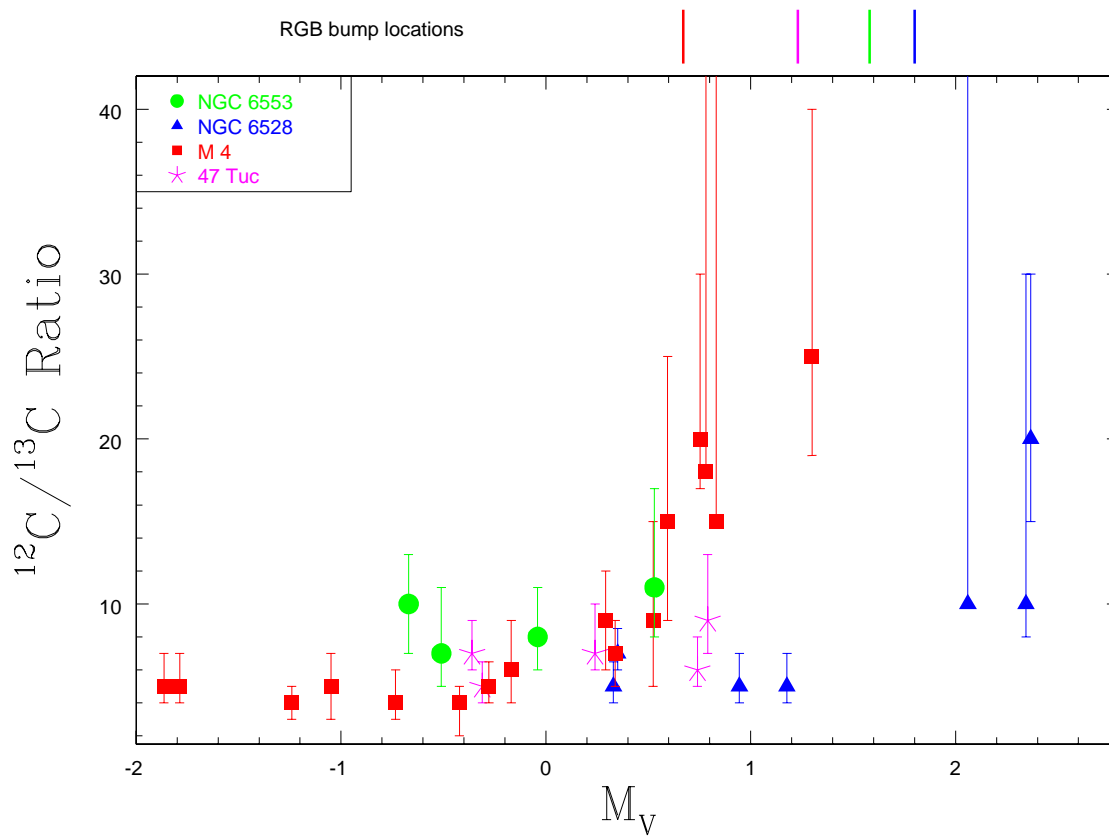


Figure 8.1 : The change of the $^{12}\text{C}/^{13}\text{C}$ carbon isotope ratio at the red bump proves the existence of extra-mixing at the red bump (plot kindly made available by M. Shetrone; Shetrone 2003, in prep).

Identification of the source of pollution in GCs

In Chapter 3 we concluded that abundance variations in 47 Tuc cannot be explained by internal stellar evolution, but that external processes must play an important role. Whether pollution by CNO processed material is important can directly be tested: the CNO process does not only alter the relative abundances of the CNO elements, but also very effectively alters the isotope ratios. In particular, the ratio of the carbon isotopes ^{12}C and ^{13}C is very sensitive to CNO-processing: It quickly changes from its initial value (which is $^{12}\text{C}/^{13}\text{C} = 89$ in the special case of the sun) to the equilibrium value of $^{12}\text{C}/^{13}\text{C} = 3$. If enrichment by CNO-processed material happened, one expects that all CN-rich stars show low $^{12}\text{C}/^{13}\text{C}$ ratios, while the CN-poor stars should still have their initial values. Internal mixing processes will alter the surface carbon isotope ratio of stars brighter than the red bump luminosity; the imprint of polluting material has to be traced among stars fainter than the red bump. The carbon isotope ratio can easily be determined by K-band infrared spectroscopy of the CO molecule at $2.34 \mu\text{m}$. Large surveys for carbon isotope ratios in nearby globular clusters are not challenging for large telescopes such as the VLT or Keck combined with intermediate resolution ($R \sim 3000$) infrared spectrographs, e.g., ISAAC at the VLT (We have received observing time for a carbon isotope survey in 47 Tuc in ESO Period 71).

Among the GCs studied by Shetrone (2002), at least M 4 is known to have bimodal CN variations (Norris et al., 1981) on the RGB; there is no evidence for a change in the relative CN absorption strengths at the red bump luminosity, supporting the idea that the relative C and N ratio at the stellar surface is only marginally altered by internal mixing processes. Unfortunately, there are no CN measurements available for the RGB of the second GC showing evidence of a changing carbon isotope ratio at the red bump, NGC 6528, in the literature.

Smith (2002b) found that in RGB stars of M 3 the carbon abundance decreases with increasing luminosity, i.e., with progressing evolution, both for CN-strong and CN-poor stars. He concludes that even CN-poor stars experienced mixing, in contrast to the expectation of the scenario of a rotationally induced mixing origin of CN variations.

The C and N content in GC stars seems to change due to both external and internal processes, although the internal process (nucleosynthesis and dredge-up of material) is not powerful enough to change the CN abundance pattern imprinted by early external processes in the stellar material and can only be identified by single element/isotope studies. Further studies of certain isotope ratios may help to investigate internal mixing processes in more detail and will allow us to disentangle the relative contribution of external and internal processes. It is remarkable that the integrated properties of GCs do not seem to be altered by the internal chemical inhomogeneity, as was demonstrated for the CH band absorption for the three metal-poor GCs M 3, M 13, and NGC 7006 in Chapter 4.

A possible proof of the mass transfer scenario: dwarf carbon stars

If a sufficient amount of ejected material is accreted by a main sequence dwarf star, the surface composition can change significantly. In particular in close binary systems Roche-lobe overflow might happen if the more massive companion star starts to evolve away from the main sequence and becomes a red giant. If the donating star becomes a carbon star after its third dredge-up (i.e., material after the He \rightarrow C burning phase is transported to the stellar envelope), the accreting star could also be converted into a carbon star. Or, the other way, if a low-mass main-sequence star shows an excess of carbon in its atmosphere (in particular, if $[C/O] \geq 1$), it has likely accreted carbon enriched material from a carbon star binary companion. A dwarf carbon star is therefore a direct proof that a star lives — or at least once lived — in a close binary system. Recent results from the Sloan Digital Sky Survey suggest that $\sim 0.2\%$ of all halo main-sequence stars are expected to be dwarf carbon stars. Within the vast number of main-sequence stars in globular clusters one should be able to find many of these dC stars — but only if the dense environment of a globular cluster allows mass-transfer in close binary systems. Up to now, nothing is known about dC stars in GCs, although they are an ideal tracer of binarity in GCs.

I recently started a photometric survey for dC stars in globular clusters using filters sensitive to the C₂ molecule bands (see Fig 8.2). The combination of two narrow band filters NB513 and NB531 at the ESO/MPG 2.2m wide field imager allows an identification of carbon enriched stars. However, the gravity sensitive Mgb and MgH lines at 5100 Å are included in the NB513 passband; there is an overlap between dC star candidates and background giant stars. A preliminary result of observations of NGC 6752 is shown in Fig. 8.3. At least

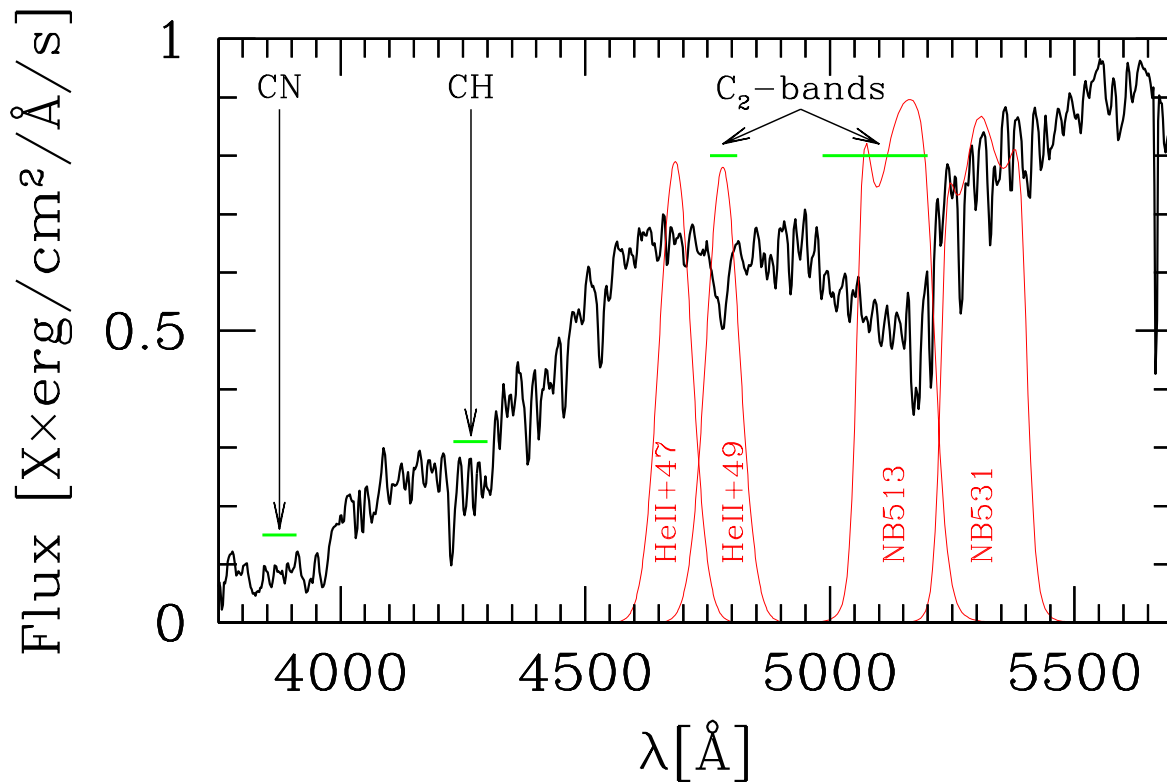


Figure 8.2 : Spectrum of a dwarf carbon star in the foreground of the globular cluster NGC 7006. C_2 sensitive filter sets are overlotted.

one promising dC star candidate could be identified. Follow-up spectroscopy is required to investigate its true nature.

By coincidence, the set of redshifted helium emission line filters of the FORS camera at the VLT overlap with a C_2 band absorption feature at 4850\AA . Although this feature is not as prominent as the 5100\AA C_2 -feature, it will not suffer from ambiguous Mgb line interference and will therefore leave a unique signature. A proposal for a dC star survey at the VLT was submitted and approved for ESO Period 71.

8.2 Do we understand dSphs?

In chapter 5 to 7 I investigated the old stellar populations — as traced by the HB and RGB — of the LG dSphs. The main conclusions of this study are:

- dSphs and transition type galaxies in general show strong population gradients. Despite the diversity of the morphologies of the CMDs of the galaxies, which indicates very different star formation histories, the less-metal rich, and therefore (assuming an age-metallicity relation) older stellar populations, are spatially more extended than the metal-rich, slightly younger stars. Within the assumption of age and metallicity as

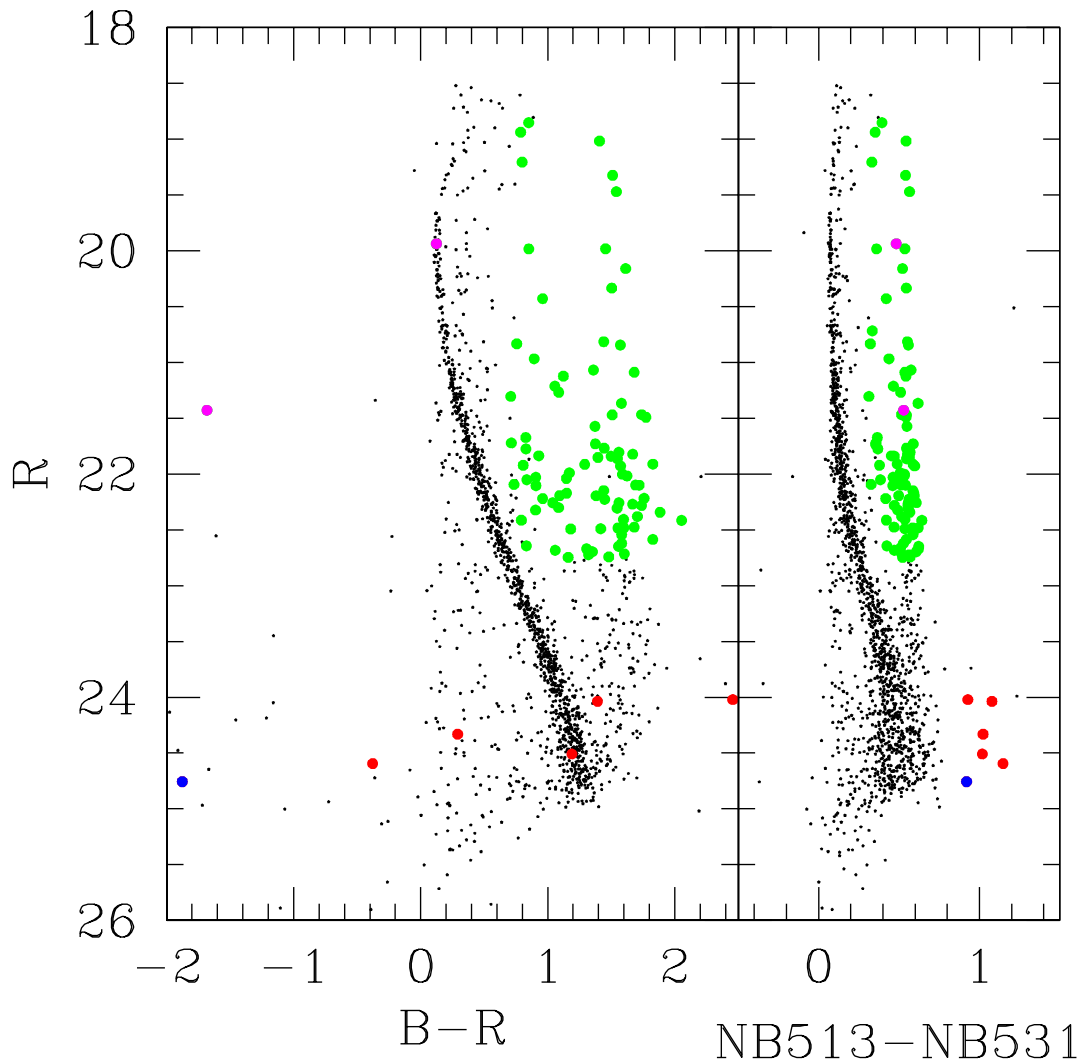


Figure 8.3 : Very preliminary result of a search for dwarf carbon (*dC*) stars in NGC 6752; magnitudes are uncalibrated. Stars with flux depletion in the C_2 -sensitive filter NB513 (see Fig. 8.2) are selected in two luminosity regions (all colored data points on the right side of the plot). The brighter stars in the sample that fall on or are bluer than the main sequence of the CMD based on the broad band filters (see left panel) are plotted with magenta dots. Due to the sensitivity of the NB513 filter to the surface gravity-sensitive Mgb feature, predominantly background giant stars are selected by this filter (green dots). For the faint sample, stars identified on the CCD images (i.e., they are not cosmic ray hits or CCD defects), are plotted with blue dots, while stars with unclear identification are plotted with red dots.

the only parameters governing the HB morphology, the HB gradients do not reflect an internal age gradient, thus implying a fast early evolution of the dSphs studied here.

- The horizontal branches of the dSphs are — compared to the Milky Way globular cluster system — too red in their morphology. The dSphs, in particular the Andromeda companions, appear to have a global second parameter effect.
- Environment does not seem to play a role in the evolution of dSphs, at least as far as the formation of population gradients is concerned.

I will in particular comment on the first two points and their implications for the formation of the dSph galaxies.

8.2.1 How could the population gradients form?

Monolithic infall

In chapter 6 I concluded that in the sparse, low-mass environment of dSphs gas might be retained in the central regions only. In the outer parts of a dSph gas could be more easily removed due to ram-pressure stripping or tidal interaction with nearby massive spirals (e.g., reviewed by Grebel, Gallagher, & Harbeck 2003). The most simplistic model of gradient formation in dSphs is ongoing star formation in a monolithically collapsing proto-galaxy. The first generation of stars will be metal-poor and widely distributed. The first supernovae will explode, and the gas in the dwarf galaxy will gain in metallicity. As the gas concentrated to the center of the young galaxy, star formation would also be concentrated, and a subsequent, more metal-rich generation of stars would be formed. The radial distribution of stellar orbits in the dSphs would represent the orbits of the star-forming molecular clouds. In the collisionless environment of dSphs the different distributions of different generations of stars would be conserved until the present day. This situation is shown in a cartoon in Fig. 8.4, upper left.

Dynamical heating

A substantially different scenario might apply to dwarf galaxies. A correlation between age and the vertical velocity dispersion (σ_z) is observed in the Milky Way disk (Wielen, 1977): Old stars have a larger σ_z , or a larger vertical scale-height. This relation can partially be explained by a *dynamical heating* process, where stars orbiting in the disk are scattered by an inhomogeneous gravity field in the galactic plane; the older stars would have experienced more scattering processes. In particular, scattering on massive molecular clouds is considered as an efficient way to increase the velocity dispersion of a stellar population (Spitzer & Schwarzschild, 1951, 1953), although their contribution to heating seems to be too weak to explain the observations. Lacey (1984) demonstrated that the velocity dispersion of stars due to giant molecular cloud (GMC) scattering will increase with time as $\sigma_z \propto \tau^{\frac{1}{2}}$. It is important to mention here that stars will not gain energy from GMC collisions forever: due to dynamical friction stellar populations will

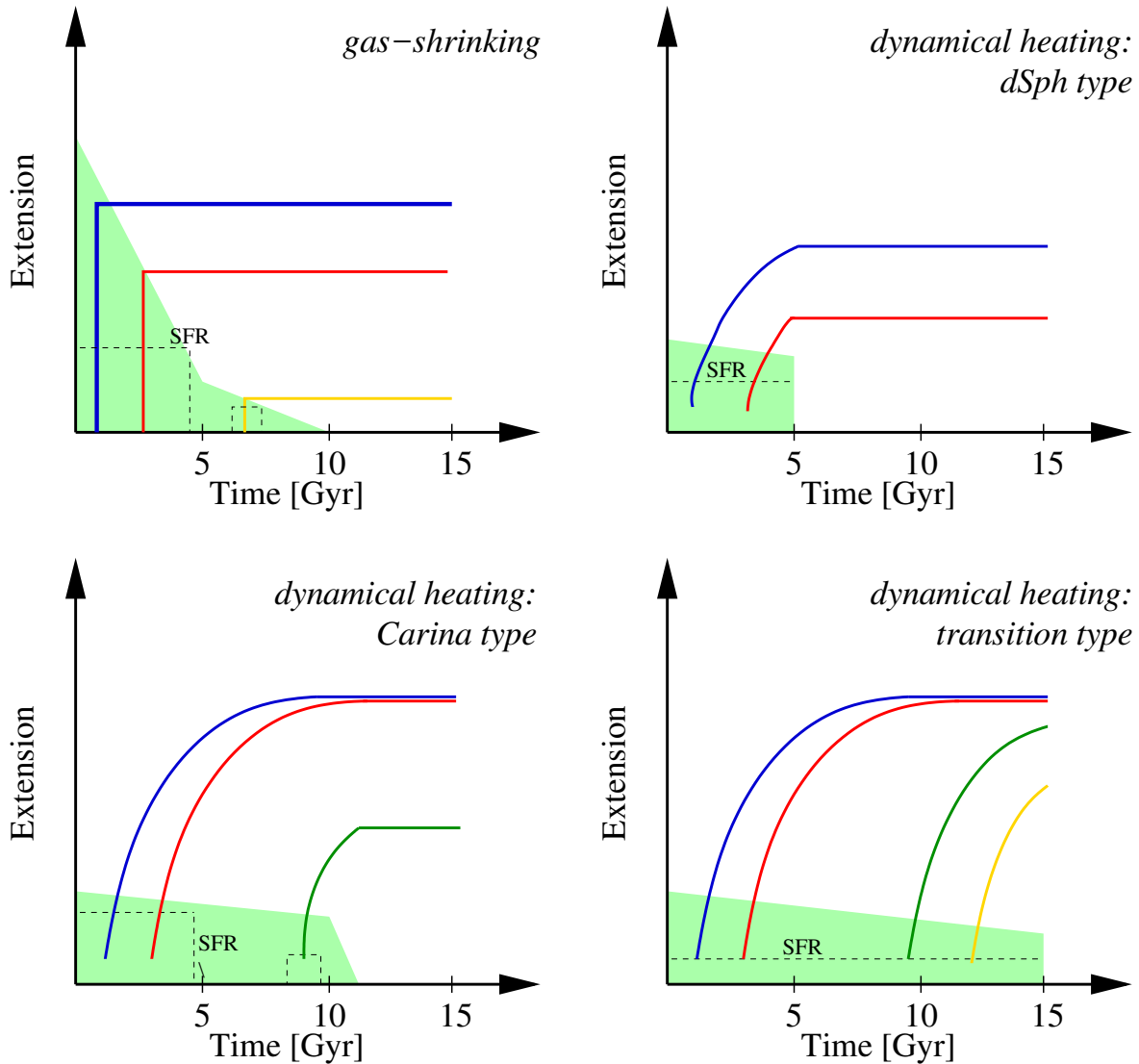


Figure 8.4 : *Cartoon of different formation scenarios of dwarf spheroidal and transition type galaxies. The green shaded regions indicate the availability and spatial extension of gas in the galaxies. The red and blue lines indicate the spatial extension of the BHB and RHB stellar population. Green and yellow lines represent intermediate old and young stellar populations. The dashed line represents a qualitative star formation rate over time. In the gas-shrinking scenario, the distribution of stars resembles the spatial distribution of the star-forming regions at the time of their birth. As the gas settles at the center of the galaxy, younger stellar populations are increasingly more centrally concentrated. In the dynamical heating scenario stars are always formed at a central region of a galaxy. Collisions of stars with molecular clouds will heat up the stars with time, leading to an increased spatial extension. The longer stars can collide with molecular clouds the more extensive their distribution until at some point saturation sets in. See text for details of the formation scenarios. Disclaimer: This cartoon graph is designed to show the principles of the possible scenarios, and should not be seen as a real model of the galaxies!*

soon end up at a limiting velocity dispersion. Simulation by Yasutomi & Fujimoto 1989 (e.g., their Fig. 2) show that this saturation happens after a time-scale of only a few 10^9 years at $\sigma \sim 40 - 50 \text{ kms}^{-1}$. Current calculations concentrate on the two-dimensional problem of spiral galaxies. Time-scales and strengths of dynamical heating by GMCs were not calculated for the different environment of dSphs. In particular, the number and size distribution of GMC in dSph might be significantly different from the situation in the Milky Way.

We will apply the *dynamical heating* model of the Milky Way disk to the formation of gradients in a dSph, assuming a gas reservoir of constant size at the center of a dSph; its size shall only marginally change with ongoing time. The first stars form and will have a certain velocity dispersion and spatial extension according to the extension and velocity dispersion of the GMCs that formed stars. With ongoing time, two effects will happen simultaneously:

- The GMCs at the galaxy's center will be enriched with metals and continue to form stars; we assume that the spatial extension of the gas will stay constant.
- Existing stars will gain energy by collisions with GMCs, their velocity dispersion will increase and their spatial extent will increase. Stars of later generations will also experience this spreading process, but they start later than the earlier stars.

At a certain time in the dSph's evolution, its gas will be lost for some reason¹, and star-formation as well as further heating will stop. In the collisionless environment of the dSph, the different spatial extension of all subpopulations will be conserved (see Fig. 8.4). We have seen in Chapter 6 that the correlation of the metallicity and HB morphology gradients suggests that age is a minor player in the HB gradients, but age differences smaller than a few Gyr will be hidden by the observed metallicity gradient. The expansion timescale of order of one to two billion years derived for the Milky Way disk would be in good agreement with the HB gradients seen in most of the dSphs.

Can we explain the central concentration of the intermediate-age stellar population (as indicated by the red clump) in the Carina dSph, but the absence of a HB morphology gradient in the dynamical heating scenario? In Fig. 8.4 (lower right) we outline a possible evolution history of Carina: Starting similarly to dSphs, Carina retains a substantial amount of its gas after the first ancient star formation episode. Both the BHB and RHB populations expand, but at some point both reach the saturation of the heating process, and the radial extensions become indistinguishable. The intermediate-age stellar population is built up at a later time and these stars also start expanding. But before the saturation level of expansion can be reached, the gas is stripped from Carina and all expansion mechanisms stop: The ancient stellar populations have the same radial extensions, while the younger stars are still centrally concentrated.

The transition type dwarf galaxy Phoenix was shown in the appendix of Chapter 6 to have only a very small gradient in the HB forming stellar population, but the younger populations showed an increasing central concentration with decreasing age. In Fig. 8.4 (lower right) we

¹The understanding of the gas-loss mechanisms in dSphs is still challenging, see Grebel, Gallagher, & Harbeck 2003 for a detailed discussion.

continue the evolution of a Carina-like galaxy, but let it retain its gas. Now, the intermediate-age stellar population (green line) can expand, younger stellar populations form, and they also start expanding. If we observe Phoenix at the present time, we will again see more or less equally distributed blue and red HB stars, but stellar populations with ages smaller than the heating saturation time will show steadily increasing central concentrations.

The scenario of dynamical heating has its special attraction to explain the formation of gradients, although it is almost impossible to be distinguished from the gas-shrinking scenario. The heating process does not necessarily have to be provided by GMC scattering. Other processes that are limited in time might lead to the expansion of the stellar populations and the gas in a dSphs with subsequent cooling and resettling of the central gas reservoir, such as tidal interaction with a massive galaxy. For instance, gas from the central regions could be expelled due to an initial star burst and enforce a rearrangement of stellar orbits in the time-dependent potential. A complete blow-away of the gas is expected to occur in galaxies of masses below $5 \cdot 10^6 M_{\odot}$ only (e.g., reviewed in Grebel, Gallagher, & Harbeck 2003), and the expelled (and enriched) gas would fall back to the center of the dSph. In the meantime the existing stars would expand in the shallower potential well of the galaxy. Later on the gas would fall back to the dSph's center and form the subsequent, centrally concentrated generation of stars (e.g., Lin & Murray 1998).

8.2.2 The global second parameter effect of LG dSphs

Buonanno et al. (1997) found stellar density to be a second parameter of the HB morphology: The residuals in a HB-type–[Fe/H]–relation nicely correlate with the central density of a GC. The denser a globular cluster is, the more stars evolve onto the BHB rather than to the RHB. In Chapter 6 I found the HBs of dSphs to be redder than those of the mean of the Milky Way GC system. I concluded that this difference might be caused by age effects, a different amount of α -elements, or other effects. In the picture of the Buonanno et al. (1997) result the sparse environment of LG dSphs suggests that their HB morphology should be redder than the MW GC system mean. I can speculate here that in the more sparse environment of a dSph the evolution of RGB stars to helium core burning HB stars can be observed unaffected by external disturbing effects as they appear in the dense environment of GCs. In this context it will be interesting to compare the relative fraction of stars that become dwarf carbon stars in the different environments of the GCs with different densities, the dSphs, and the Milky Way halo.

ω Cen - the core of a dwarf galaxy?

ω Cen is the only GC of the Milky Way known to have significant star-to-star variations in the iron peak element abundance. In contrast to ordinary GCs, it also shows signs of an internal spread in age (up to 6 Gyr, e.g., Hilker & Richtler 2000) and in metallicity ([Fe/H] ranging from -1.6 dex to -0.6 dex). ω Cen has therefore been discussed as the stripped nucleus of a captured dwarf galaxy. The metallicity of the dominant stellar population in ω Cen is [Fe/H]= -1.7 dex. In contrast to the dSphs studied here, its HB morphology is as

blue as would be expected with a HB index of 0.9 (Harris, 1996).

The stellar density of ω Cen suggests it to be the nucleus of a dwarf elliptical (dE) galaxy rather than a dSph galaxy. Only little information is available about HBs of dEs in the literature. The closest dEs in the LG are the Andromeda companions NGC 185 and NGC 205. Although the distance of these galaxies would allow photometry of their HBs, the high stellar density in dEs is the major complication. Geisler et al. (1999) found evidence of metal-rich ($[\text{Fe}/\text{H}] \sim -0.7$ dex or higher), old field star populations in the two Andromeda dEs (based on HST/WFPC2 imaging). Han et al. (1997) found a predominantly red HB morphology in the LG dE galaxy NGC 147. The observed HB morphologies match the expectations at this metallicity, i.e., predominantly the red part of the HB is populated. There is no photometry available of the stellar population in the dense nuclei, which would correspond to an ω Cen GC.

Thus, if ω Cen was the nucleus of a accreted dSph or dE galaxy, its HB morphology does not fit smoothly into the trend of anomalously HB morphologies among the LG dwarf galaxies observed at the present time. As each galaxy is an individual, however, the difference in the HB morphology of Ω Cen to the LG dSphs and dEs does not necessarily contradict the accretion scenario.

8.2.3 Further projects

The correlation between radial gradients in the RGB and in the HB of dSph galaxies suggests that the main driver of the gradients is metallicity. The current photometric metallicity determinations suffer from a degeneracy in age and metallicity. But quantitative $[\text{Fe}/\text{H}]$ distributions will permit constructing a comprehensive scenario of dSph formation. Such quantitative measurements of metallicity gradients in dSphs would require large spectroscopic surveys. With large telescopes and fiber-fed spectrographs these become very efficient today. An observing campaign to obtain Ca II triplet metallicities for 160 RGB stars in the Sextans dSph with the Hydra multi-fiber spectrograph at the 3.5m WIYN telescope unfortunately became a victim of strong winds — the telescope was shaking and too little light was actually collected by the fibers. An approved Large Programme at the VLT with FLAMES will provide us with Ca II triplet metallicities for large samples of stars in LG dSphs.

*How shall we have patience for the consummation of the mystery?
Who will comfort us in the going through?
Sir Michael Tippet, A Child of our Time*

References

- Armandroff, T. E., Da Costa, & G. S., Caldwell, N., Seitzer, P. 1993, AJ, 106, 986
- Armandroff, T. E., Jacoby, G. H., & Davies, J. E. 1999, AJ, 118, 1220
- Ashman, K. A., Bird, C. M., & Zepf, S. E. 1994, AJ, 108, 2348
- Baade, D., Meisenheimer, K., Iwert, O. et al. 1998, Messenger, 93, 13
- Battinelli, P., & Demers, S. 2000, AJ, 120, 1801
- Behr, B. B., Djorgovski, S. G., Cohen, J. G., McCarthy, J. K., Côté, P., Piotto, G., & Zoccali, M. 2000, ApJ, 528, 849
- Behr, B. B., Cohen, J. G., & McCarthy, J. K. 2000, ApJ, 531, L37
- Bell, R. A. & Gustafsson, B. 1978, A&AS, 34, 229
- Bell, R. A., Hesser, J. E., & Cannon, R. D. 1983, ApJ, 269, 580
- Bell, R. A., Hesser, J. E., & Cannon, R. D. 1984, ApJ, 283, 615
- Bellazzini, M., Fusi Pecci, F., & Ferraro, R. R. 1996, MNRAS, 278, 947
- Bellazzini, M., Ferraro, F. R., & Pancino, E. 2001, MNRAS, 327, L15
- Bellazzini, M., Ferraro, F. R., Origlia, L., Pancino, E., Monaco, L., & Oliva, E. 2002, AJ, 124, 3222
- Bernardi, M., Sheth, R. K., Annis, J., et al. (2003), AJ, in press; astro-ph/0301629
- Briley, M. M., Hesser, J. E., & Bell, R. A. 1991, ApJ, 373,
- Briley, M. M., Smith, G. H., Bell, R. A., Oke, J. B., & Hesser, J. E. 1992, ApJ, 387, 612
- Briley, M. M. & Smith, G. H. 1993, ASP Conf. Ser. 48: The Globular Cluster-Galaxy Connection, 184
- Briley, M. M., Hesser, J. E., Bell, R. A., Bolte, M., & Smith, G. H. 1994, AJ, 108, 2183
- Briley, M. M., Smith, V. V., Suntzeff, N. B., Lambert, D. L., Bell, R. A., & Hesser, J. E. 1996, Nature, 383, 604
- Briley, M. M. 1997, AJ, 114, 1051

- Briley, M. M., & Cohen, J. G. 2001, *AJ*, 122, 242
- Bruzual A., G. & Charlot, S. 1993, *ApJ*, 405, 538
- Buonanno et al. 1991, *AJ* 102, 1005
- Buonanno, R., Corsi, C., Bellazzini, M., Ferraro, F. R., & Pecci, F. F. 1997, *AJ*, 113, 706
- Buonanno, R., Corsi, C. E., Castellani, M., Marconi, G., Fusi Pecci, F., & Zinn, R. 1999, *AJ*, 118, 1671
- Burstein, D., Faber, S. M., Gaskell, C. M., & Krumm, N. 1984, *ApJ*, 287, 586
- Caldwell, N., Armandroff, T. E., Seitzer, P., & Da Costa, G. S. 1992, *AJ*, 103, 840
- Caldwell, N. 1999, *AJ*, 118, 1230
- Cannon, R. D., Croke, B. F. W., Bell, R. A., Hesser, J. E., & Stathakis, R. A. 1998, *MNRAS*, 298, 601
- Carbon, D. F., Romanishin, W., Langer, G. E., Butler, D., Kemper, E., Trefzger, C. F., Kraft, R. P., & Suntzeff, N. B. 1982, *ApJS*, 49, 207
- Catelan, M., Bellazzini, M., Landsman, W. B., Ferraro, F. R., Fusi Pecci, F., & Galletti, S. 2001, *AJ*, 122, 3171
- Cavallo, R. M., Sweigart, A. V., & Bell, R. A. 1996, *ApJ*, 464, L79
- Cavallo, R. M., Sweigart, A. V., & Bell, R. A. 1998, *ApJ*, 492, 575
- Cavallo, R. M. & Nagar, N. M. 2000, *AJ*, 120, 1364
- Chun, M. S. & Freeman, K. C. 1978, *AJ*, 83, 376
- Cohen, J. G. & Frogel, J. A. 1982, *ApJ*, 255, L39
- Cohen, J. G., Blakeslee, J. P., & Ryzhov, A. 1998, *ApJ*, 496, 808
- Cohen, J. G. 1999a, *AJ*, 117, 2428
- Cohen, J. G. 1999b, *AJ*, 117, 2434
- Cohen, J. G., Briley, M. M., & Stetson, P. B. 2002, *AJ*, 123, 2525
- Côté, P., Hanes, D. A., McLaughlin, D. E., Bridges, T. J., Hesser, J. E., & Harris, G. L. H. 1997, *ApJ*, 476, L15
- Cunha, K., Smith, V. V., Suntzeff, N. B., Norris, J. E., Da Costa, G. S., & Plez, B. 2002, *AJ*, 124, 379
- Da Costa, G. S. & Armandroff, T. E. 1990, *AJ*, 100, 162
- Da Costa, G. S., Hatzidimitriou, D., Irwin, M. J., McMahon, R. G., 1991, *MNRAS*, 249, 473
- Da Costa, G. S., Armandroff, T. E., Caldwell, N., & Seitzer, P. 1996, *AJ*, 112, 2576

- Da Costa, G. S., Armandroff, T. E., Caldwell, N., & Seitzer, P. 2000, *AJ*, 119, 705
- Denisenkov, P. A. & Denisenkova, S. N. 1990, *Soviet Astronomy Letters*, 16, 275
- Denissenkov, P. A., Weiss, A., & Wagenhuber, J. 1997, *A&A*, 320, 115
- van Dokkum, P. G. 2001, *PASP*, 113, 1420
- Dolphin, A. E. 2000, *PASP*, 112, 1383
- Dolphin, A. E. 2000, *PASP*, 112, 1397
- Dolphin, A. E. 2001, *MNRAS*, submitted
- Faber, S. M., Trager, S. C., Gonzalez, J. J., & Worthey, G. 1995, *IAU Symp. 164: Stellar Populations*, 164, 249
- Ferraro, F. R., Clementini, G., Fusi-Pecchi, F., Vitiello, E., & Buonanno, R. 1993, *MNRAS*, 264, 273
- Freeman, K. C. 1993, in *Galactic Bulges*, *IAU Symp 153*, ed. H. Dejonghe & H. J. Habing (Dordrecht: Kluwer), p. 263
- Freire, P. C., Kramer, M., Lyne, A. G., Camilo, F., Manchester, R. N., & D'Amico, N. 2001, *ApJ*, 557, L105
- Fusi Pecci, F., Ferraro, F. R., Crocker, D. A., Rood, R. T., & Buonanno, R. 1990, *A&A*, 238, 95
- Gallart, C., Freedman, W. L., Aparicio, A., Bertelli, G., & Chiosi, C. 1999, *AJ*, 118, 2245
- Geisler, D., 1984, *PASP*, 96, 723
- Geisler D., Clariá J. J. & Minniti, D., 1991, *AJ*, 102, 1836
- Geisler, D. 1996, *AJ*, 111, 480
- Geisler, D., & Sarajedini, A. 1999, *AJ*, 117, 308
- Geisler, D., Armandroff, T., da Costa, G., Lee, M. G., & Sarajedini, A. 1999, *IAU Symposium*, 192, 231
- Girardi, L., Groenewegen, M. A. T., Weiss, A., & Salaris, M. 1998, *MNRAS*, 301, 149
- Girardi, L., Bressan, A., Bertelli, G., & Chiosi, C. 2000, *A&AS*, 141, 371
- Gnedin, O. Y., Zhao, H. S., Pringle, J. E., Fall, S. M., Livio, M., & Meylan, G. 2002, *ApJ*, 568, L23
- Gratton, R. G. et al. 2001, *A&A*, 369, 87
- Grebel, E. K. 1997, *Reviews of Modern Astronomy*, 10, 29
- Grebel, E. K. 1999, in *IAU Symp. 192, The Stellar Content of the Local Group*, eds. P. Whitelock & R. Cannon (Provo: ASP), 17

- Grebel, E. K. 2000, in 33rd ESLAB Symposium, Star Formation from the Small to the Large Scale, SP-445, eds. F. Favata, A.A. Kaas, & A. Wilson (Noordwijk: ESA), 87
- Grebel, E. K., Braun, R., & Burton, W. B. 2000, American Astronomical Society Meeting, 196
- Grebel, E. K. & Guhathakurta, P. 1999, ApJ, 511, L101
- Grebel, E. K. & Harbeck, D. 2002, Astronomische Gesellschaft Meeting Abstracts, 19, 117
- Grebel, E. K., Gallagher, J. S., & Harbeck, D. 2003, AJ, in press; astro-ph/0301025
- Grebel, E. K., Harbeck, D., Holtzman, J., Geisler, D., & Sarajedini, A. 2003, in prep.
- Guhathakurta, P., Grebel, E.K., Pittroff, L.C., et al. 2003, AJ, in prep.
- Gustafsson, B., Bell, R. A., Eriksson, K., & Nordlund Å. 1975, A&A, 42, 407
- Han, M., Hoessel, J. G., Gallagher, J. S., Holtzman, J., & Stetson, P. B. 1997, AJ, 113, 1001
- Harbeck, D. et al. 2001, AJ, 122, 3092
- Harbeck, D., Smith, G.H., & Grebel, E.K. 2003, AJ, 125, 197
- Hargreaves, J. C., Gilmore, G., Irwin, M. J., Carter, D., 1994, MNRAS269, 957
- Harris W.E. 1996, AJ, 112, 1487
- Held, E. V., Saviane, I. & Momany, Y. 1999, A&A, 345, 747
- Hesser, J. E. 1978, ApJ, 223, L117
- Hesser, J. E. & Bell, R. A. 1980, ApJ, 238, L149
- Hesser, J. E., Harris, G. L. H., Bell, R. A., & Cannon, R. D. 1984, in Observational Tests of the Stellar Evolution Theory, IAU Symp. 105, eds. A. Maeder & A. Renzini. (Dordrecht: Reidel), p. 139
- Hesser, J. E., Harris, W. E., Vandenberg, D. A., Allwright, J. W. B., Shott, P., & Stetson, P. B. 1987, PASP, 99, 739
- Hilker, M. & Richtler, T. 2000, A&A, 362, 895
- Hirashita, H. 1999, ApJ, 520, 607
- Holtzman, J. A., Smith, G. H., & Grillmair, C. 2000, AJ, 120, 3060
- Hughes, J., & Wallerstein, G. 2000, AJ, 119, 1225
- Hurley-Keller, D., Mateo, M., & Nemeč, J. 1998, AJ, 115, 1840
- Hurley-Keller, D., Mateo, M., & Grebel, E. K. 1999, ApJ, 523, L25
- Irwin, M. J., Bunclark, P. S., Bridgeland, M. T. & McMahon, R. G., 1990, MNRAS, 224, 16P
- Irwin, M., & Hatzidimitriou, D. 1995, MNRAS, 277, 1354

- Kaluzny, J. & Udalski, A. 1992, *Acta Astronomica*, 42, 29
- Klessen, R., Grebel, E. K., & Harbeck, D. 2003, *ApJ*, in press; astro-ph/0302287
- Kleyna, J., Wilkinson, M. I., Evans, N. W., Gilmore, G., & Frayn, C. 2002, *MNRAS*, 330, 792
- Kraft, R. P. 1994, *PASP*, 106, 553
- Kraft, R. P., Sneden, C., Smith, G. H., Shetrone, M. D., & Fullbright, J. 1998, *AJ*, 115, 1500
- Krist, J. 1993, *ASP Conf. Ser. 52: Astronomical Data Analysis Software and Systems II*, 2, 536
- Lacey, C. G. 1984, *MNRAS*, 208, 687
- Langer, G. E. 1985, *PASP*, 97, 382
- Langer, G. E., Suntzeff, N. B., & Kraft, R. P. 1992, *PASP*, 104, 523
- Langer, G. E., Hoffman, R., & Sneden, C. 1993, *PASP*, 105, 301
- Lee, Y.-W., Demarque, P., & Zinn, R. 1994, *ApJ*, 423, 248
- Lee, H., Yoon, S., & Lee, Y. 2000, *AJ*, 120, 998
- Lee, Y.-W., Yoon, S.-J., Rey, S.-C., & Chaboyer, B. 2001, in *ASP Conf. Ser., Astrophysical Ages and Time Scales*, eds. T. von Hippel, N. Mabet & C. Simpson, in press
- Lejeune, T. & Schaerer, D., 2001, *A&A*, in press.
- Liebert, J., Saffer, R. A., & Green, E. M. 1994, *AJ*, 107, 1408
- Lin, D. N. C. & Murray, S. D. 1998, in *Dwarf Galaxies and Cosmology, XXXIIIrd Rencontres de Moriond*, eds. T. X.Thuan, C. Balkowski, V. Cayatte, & J. T. T. Van (Paris: Editions Frontières), 433
- Mac Low, M.-M., & Ferrara, A., 1999, *ApJ*, 513, 142
- Majewski, S. R., Siegel, M. H., Patterson, R. J., & Rood, R. T. 1999, *ApJ*, 520,33
- Majewski, S. R., Ostheimer, J. C., Patterson, R. J., Kunkel, W. E., Johnston, K. V., & Geisler, D. 2000, *AJ*, 119, 760
- Martínez-Delgado, D., Gallart, C., & Aparicio, A. 1999, *AJ*, 118, 862
- Maraston, C. & Thomas, D. 2000, *ApJ*, 541, 126
- Mateo, M., Nemeč, J., Irwin, M.; McMahon, R., 1991, *AJ*, 101, 892
- Mateo, M., Fischer, F. & Krzeminski, W., 1995, *AJ* 110, 2166
- Mateo, M. 1998, *ARA&A*, 36, 435
- Mayer, L., Governato, F., Colpi, M., Moore, B., Quinn, T., Wadsley, J., Stadel, J., & Lake, G. 2001, *ApJ*, 547, 123

- McClure, R. D. & Hesser, J. E. 1981, *ApJ*, 246, 136
- McClure, R. D. & Osborn, W. 1974, *ApJ*, 189, 405
- Mighell, K. J. & Rich, R. M. 1996, *AJ*, 111, 777
- Mighell, K. J. 1997, *AJ*, 114, 1458
- Mironov, A. V. 1972, *Soviet Astronomy*, 16, 105
- Monet et al., 1996, USNO-SA1.0, (U.S. Naval Observatory, Washington DC)
- Monkiewicz, J. et al. 1999, *PASP*, 111, 1392
- Norris, J. & Freeman, K. C. 1979, *ApJ*, 230, L179
- Norris, J. 1981, *ApJ*, 248, 177
- Norris, J., Cottrell, P. L., Freeman, K. C., & Da Costa, G. S. 1981, *ApJ*, 244, 205
- Norris, J. & Freeman, K. C. 1983, *ApJ*, 266, 130
- Norris, J., Freeman, K. C., & Da Costa, G. S. 1984, *ApJ*, 277, 615
- Norris, J. 1987, *ApJ*, 313, 65
- Odenkirchen, M. et al. 2001, *AJ*, 122, 2538
- Osborn, W. 1971, *The Observatory*, 91, 223
- Pagel, B. E. J. & Portinari, L. 1998, *MNRAS*, 298, 747
- Palma, C., Majewski, S. R., Siegel, M. H., & Patterson, R. J. 2000, *AAS*, 197, 7808
- Paltoglou, G. 1990, *BAAS*, 22, 1289
- Paltoglou, G. & Bell, R. A., 1994, *MNRAS*, 268, 793
- Pancino, E., Ferraro, F. R., Bellazzini, M., Piotto, G., & Zoccali, M. 2000, *ApJ*, 534, L83
- Pancino, E., Pasquini, L., Hill, V., Ferraro, F. R., & Bellazzini, M. 2002, *ApJ*, 568, L101
- Puzia, T. H., Kissler-Patig, M., Brodie, J. P., & Huchra, J. P. 1999, *AJ*, 118, 2734
- Ratnatunga, K. U. & Bahcall, J. N. 1985, *ApJS*, 59, 63
- Rey, S., Yoon, S., Lee, Y., Chaboyer, B., & Sarajedini, A. 2001, *AJ*, 122, 3219
- Rose, J. A. 1984, *AJ*, 89, 1238
- Sandage A. & Wallerstein G. 1960, *ApJ* 131,598
- Sandage A. & Wildey R. 1967, *ApJ* 150, 469
- Sandage, A. 1990, *ApJ*, 350, 603

- Sarajedini, A., & Forrester, W. L. 1995, *AJ*, 109, 1112
- Sarajedini, A., Chaboyer, B., & Demarque, P. 1997, *PASP*, 109, 1311
- Sarajedini, A., & Layden, A. 1997, *AJ*, 113, 264
- Saviane, I., Held, E. V., Piotto, G. 1996, *A&A*, 315, 40
- Saviane, I., Held, E. V., & Piotto, G. 1996, *A&A*, 315, 40
- Saviane I., Held E. V., & Bertelli G. 2000, *A&A*, 355, 56
- Schlegel, D., Finkbeiner, D., & Davis, M. 1997, *ApJ*, 500, 525
- Schneider, D. P. et al. 2002, *AJ*, 123, 567
- Schroder, L. L., Brodie, J. P., Kissler-Patig, M., Huchra, J. P., & Phillips, A. C. 2002, *AJ*, 123, 2473
- Shetrone, M. D., Côté, P., & Sargent, W. L. W. 2001, *ApJ*, 548, 592
- Smith, G. H. & Norris, J. 1982, *ApJ*, 254, 149
- Smith, G. H. & Bell, R. A. 1986, *AJ*, 91, 1121
- Smith, G. H. 1987, *PASP*, 99, 67
- Smith, G. H., Bell, R. A., & Hesser, J. E. 1989, *ApJ*, 341, 190
- Smith, G. H. & Mateo, M. 1990, *ApJ*, 353, 533
- Smith, E. O., Rich, R. M., & Neill, J. D. 1998, *AJ*, 115, 2369
- Smith, G. H. 1999, *PASP*, 111, 980
- Smith G.H. et al. 1996, *AJ* 112,1511
- Smith G.H. & Fullbright J. 1997, *PASP* 109, 1246
- Smith, G. H. 2002a, *PASP*, 114, 1215
- Smith, G. H. 2002b, *PASP*, in press
- Spitzer, L. J. & Schwarzschild, M. 1951, *ApJ*, 114, 385
- Spitzer, L. J. & Schwarzschild, M. 1953, *ApJ*, 118, 106
- Stetson, P.B. 1992, in *ASP Conf. Ser. 25, Astronomical Data Analysis Software and Systems I*, eds. D.M. Worrall, C. Biemesderfer, & J. Barnes (San Francisco: ASP), 297
- Stetson, P. B., Hesser, J. E., Smecker-Hane, T. A. 1997, *PASP*, 110, 533
- Stetson, P. B., Hesser, J. E., & Smecker-Hane, T. A. 1998, *PASP*, 110, 533
- Suntzeff, N. B. 1981, *ApJS*, 47, 1

- Suntzeff, N. B., & Smith, V. V. 1991, *ApJ*, 381, 160
- Suntzeff, N. 1993a, *ASP Conf. Ser. 48: The Globular Cluster-Galaxy Connection*, 167
- Suntzeff, Nicholas B., Mateo, Mario, Terndrup, Donald M., Olszewski, E. W., Geisler, D., Weller, W., 1993b, *ApJ*, 418, 208
- Sweigart, A. V. 1997, *ApJ*, 474, L23
- Sweigart, A. V. & Catelan, M. 1998, *ApJ*, 501, L63
- Thoul, A., Jorissen, A., Goriely, S., Jehin, E., Magain, P., Noels, A., & Parmentier, G. 2002, *A&A*, 383, 491
- Trager, S. C., Faber, S. M., Worthey, G., & González, J. J. 2000a, *AJ*, 119, 1645
- Trager, S. C., Faber, S. M., Worthey, G., & González, J. J. 2000b, *AJ*, 120, 165
- Trauger, J.T., et al. 1994, *ApJ*, 435, L3
- Ventura, P., D'Antona, F., Mazzitelli, I., & Gratton, R. 2001, *ApJ*, 550, L65
- Vandenberg, D. A., Bolte, M., & Stetson, P. B., 1990 *AJ*, 100, 445
- van den Bergh, S. 1994, *ApJ*, 428, 617
- van den Bergh, S. 1999, *A&ARv*, 9, 273
- VandenBerg, D. A., Swenson, F. J., Rogers, F. J., Iglesias, C. A., & Alexander, D. R. 2000, *ApJ*, 532, 430
- VandenBerg, D. A. & Bell, R. A. 2001, *New Astronomy Review*, 45, 577
- Wachter, S., Wallerstein, G., Brown, J. A., & Oke, J. B. 1998, *PASP*, 110, 821
- Weiss, A., Denissenkov, P. A., & Charbonnel, C. 2000, *A&A*, 356, 181
- Welch, D. L. & Stetson, P. B. 1993, *AJ*, 105, 1813
- Wielen, R. 1977, *A&A*, 60, 263
- Wilkinson, M. I., Kleyna, J., Evans, N. W., & Gilmore, G. 2002, *MNRAS*, 330, 778
- Wirth, A. 1985, *ApJ*, 288, 132
- Worthey, G., Faber, S. M., Gonzalez, J. J., & Burstein, D. 1994, *ApJS*, 94, 687
- Yasutomi, M. & Fujimoto, M. 1989, *PASJ*, 41, 823
- Zinn, R. & West, M. J., 1984, *ApJS*, 55, 45
- Zinn, R. J. 1986, in *Stellar Populations* (Cambridge, Cambridge University Press), 73
- Zinn R. J. 1993, in *ASP Conf. Ser. 48, The Globular Cluster-Galaxy Connection*, ed. G. H. Smith and J.P. Brodie (San Francisco: ASP), 98

Acknowledgements

First of all, I wish to thank Eva Grebel for her great support during the last three years in Heidelberg. I much enjoyed her collaborative spirit and her way of giving advice (rather than supervising me), providing me the freedom to work independently on my projects. I'm also grateful for the support by Professor Graeme Smith, who gave me extra advice on my thesis. I would like to thank Professor Jay Gallagher for his behind-the-scene support and advisory assistance ever since our first meeting at the *Modes of Star Formation conference* in Heidelberg. Furthermore I would like to thank Andreas Burkert for discussions and for doing academic supervision of my thesis. Many thanks to Professor Immo Appenzeller for co-correcting this thesis.

I gratefully acknowledge funding during the last three years by the Max-Planck-Institut für Astronomie. I would especially like to thank Lilo Schleich, who with great patience organized many trips for me and went through the trouble of doing my travel expenses. I would like to thank Doug Geisler and Tom Richtler (Universidad de Concepción, Concepción, Chile), Jon Holtzman (New Mexico State University, Las Cruces, USA), Jay Gallagher (University of Wisconsin, Madison, USA), and Graeme Smith (University of California, Santa Cruz) for inviting me to or hosting me at their home institutes. Further, I would like to thank George Wallerstein for providing me with the necessary financial support allowing me to visit the conference on Nucleosynthesis, 2002, Seattle, USA.

For scientific and secular discussions during lunch-time and at other opportunities I thank Michael Odenkirchen, Henry Lee, Dan Zucker, David Anderson, Eric Bell, and all the many others. I would also like to mention the enlightening coexistence with my past and current roommates, Sebastian Jester, Jakob Walcher, Rene Faßbender, Andreas Koch, and Zoltan Kovacs.

Last but not least I would like to thank my family and my girl-friend for their wonderful support during these past three years.

Further acknowledgements:

This work is partly based on observations made with the NASA/ESA Hubble Space Telescope, obtained from the data archive at the Space Telescope Science Institute. STScI is operated by the Association of Universities for Research in Astronomy, Inc. under NASA contract NAS 5-26555. I also used observations made with ESO Telescopes at the Paranal Observatory under programme ID 67.D-0153 and the MPG/ESO 2.2m telescope at La Silla Observatory.

This work made use of the IRAF software package. IRAF is distributed by the National Optical Astronomy Observatories, which are operated by the Association of Universities for Research in Astronomy, Inc., under cooperative agreement with the National Science Foundation. The Digitized

Sky Surveys were produced at the Space Telescope Science Institute under U.S. Government grant NAG W-2166. The images of these surveys are based on photographic data obtained using the Oschin Schmidt Telescope on Palomar Mountain and the UK Schmidt Telescope. The plates were processed into the present compressed digital form with the permission of these institutions. The Second Palomar Observatory Sky Survey (POSS-II) was made by the California Institute of Technology with funds from the National Science Foundation, the National Geographic Society, the Sloan Foundation, the Samuel Oschin Foundation, and the Eastman Kodak Corporation. The Oschin Schmidt Telescope is operated by the California Institute of Technology and Palomar Observatory. The UK Schmidt Telescope was operated by the Royal Observatory Edinburgh, with funding from the UK Science and Engineering Research Council (later the UK Particle Physics and Astronomy Research Council), until 1988 June, and thereafter by the Anglo-Australian Observatory.

This research has made use of NASA's Astrophysics Data System Bibliographic Services.

Funding for the creation and distribution of the SDSS Archive has been provided by the Alfred P. Sloan Foundation, the Participating Institutions, the National Aeronautics and Space Administration, the National Science Foundation, the U.S. Department of Energy, the Japanese Monbukagakusho, and the Max Planck Society. The SDSS Web site is <http://www.sdss.org/>. The SDSS is managed by the Astrophysical Research Consortium (ARC) for the Participating Institutions. The Participating Institutions are The University of Chicago, Fermilab, the Institute for Advanced Study, the Japan Participation Group, The Johns Hopkins University, Los Alamos National Laboratory, the Max-Planck-Institute for Astronomy (MPIA), the Max-Planck-Institute for Astrophysics (MPA), New Mexico State University, University of Pittsburgh, Princeton University, the United States Naval Observatory, and the University of Washington.